# UNIVERSITE LOUIS PASTEUR

ECOLE NATIONALE SUPERIEURE DE PHYSIQUE DE STRASBOURG

LABORATOIRE DES SYSTEMES PHOTONIQUES

# THESE

Présentée pour obtenir
le titre de Docteur de l'Université Louis Pasteur
en Physique Photonique

par

**Olivier HAEBERLÉ**

## ELECTROMAGNETIC RADIATION GENERATED BY RELATIVISTIC ELECTRONS INTERACTING WITH A DIFFRACTION GRATING

Date de soutenance: 9 DÉCEMBRE 1994

Commission d'examen:

| | |
|---|---|
| J. HARTHONG | Rapporteur interne-Président |
| P. AMBS | Rapporteur externe |
| L. WARTSKI | Rapporteur externe |
| N. MAENE | |
| P. MEYRUEIS | |
| P. RULLHUSEN | Membre invité |
| J.-M. SALOMÉ | Membre invité |

# TABLE OF CONTENTS

# ABSTRACT

The Smith-Purcell effect has been widely studied since its theoretical prediction in 1942 and its first experimental confirmation in 1953. The previous available models assume electrons moving parallel to a grating surface and perpendicular to the grating rulings. In the first chapter, the description of the Smith-Purcell effect for electrons moving parallel to a grating, at an arbitrary angle with respect to the grating rulings is exposed in the frame of an electromagnetic theory.

The model is restricted to perfectly conducting surfaces, for which some of the modern available techniques to solve the grating problem are adapted to the peculiar configuration of the incident field. These techniques are developed in the second chapter.

In chapter three, the Smith-Purcell radiation produced by relativistic electrons with energy in the 1 to 100 MeV range interacting with millimeter period gratings is calculated, using the previously developed theories. The properties of the radiation are described and possible applications are proposed.

In the fourth chapter, the GELINA facility which was used to carry out Smith-Purcell experiments is described.

In chapter five, the Smith-Purcell experiments are described. The spectral and angular distributions, the polarization and the dependence on the electron energy of the radiation obtained by interaction of high energy electrons of 20 to 110 MeV with optical gratings in various configurations are presented.

# RÉSUMÉ

L’ effet Smith-Purcell a été largement étudié depuis la prédiction de son existence en 1942 et sa première confirmation expérimentale en 1953. Les modèles théoriques précédemment existants supposent un électron se propageant parallèlement à la surface du réseau de diffraction et perpendiculairement aux traits du réseau. Dans le chapitre premier est exposée dans le cadre d’ une théorie électromagnétique la description de l’ effet Smith-Purcell pour un électron se propageant parallèlement à la surface d’ un réseau de diffraction avec un angle arbitraire par rapport aux traits du réseau.

Le modèle proposé est restreint au cas des surfaces parfaitement conductrices, pour lesquelles quelques techniques modernes de résolution du problème de réseau ont été adaptées à la configuration particulière du champ incident. Ces techniques sont décrites dans le second chapitre.

Dans le chapitre trois, le rayonnement de Smith-Purcell produit par des électrons relativistes d’ énergie 1 à 100 MeV en interaction avec des réseaux millimétriques est calculé en utilisant les théories précédemment développées. Les propriétés du rayonnement sont décrites et quelques applications potentielles sont proposées.

L’ accélérateur GELINA utilisé pour la réalisation des expériences Smith-Purcell est décrit dans le chapitre quatre.

Dans le chapitre cinq, les expériences Smith-Purcell sont décrites. Les distributions spectrales et angulaires, la polarization et la dépendance par rapport à l’ énergie des électrons du rayonnement obtenu par interaction d’ électrons de 20 à 110 MeV avec des réseaux optiques sont présentées.

# INTRODUCTION

In 1942, Franck [1] predicted that a fast electron passing close to a diffractive structure would emit polarized light. But one had to wait till 1953 for the first experimental confirmation obtained by Smith and Purcell [2] who observed visible radiation from an about 300 keV electron beam passing close to an optical grating. Independently, Salisbury [3] had similar ideas in 1949 and demonstrated generation of submillimeter and millimeter waves.

Several theories have been formulated to explain that the emitted light is strongly polarized, the wavelength satisfying a simple dispersion relation involving the structure period, the speed of the emitting electrons, and the angle of observation. Smith and Purcell proposed that the electromagnetic radiation is caused by the periodic motion of the charges induced on the grating surface by the electrons from the beam. This explanation was improved by Salisbury [4] and Ishiguro and Tako [5], who considered the vibrating dipole formed by a moving electron and its accompanying image, oscillating with respect to the periodic grating surface. Using these models, one was able to explain the polarization of the emitted light, and to derive the dispersion relation. So it has been rapidly planned to use the Smith-Purcell effect as a sources in the millimeter to visible range for which tunable sources were hardly or not available. In this optic, Bradchaw [6] in the millimeter range, Ishiguro and Tako [5] in the near infrared and Salisbury [7] in the infrared, visible and ultraviolet carried out experiments to build such generators. The results were however not very satisfying and it appeared that the quantitative predictions were not correct. In fact it has been proved that these models are not convenient for a rigorous theoretical analysis.

In 1960, Toraldo di Francia [8] established the analogy between the Cherenkov [9] and the Smith-Purcell radiation. In this approach, the electric field of the moving electron is described by a set of evanescent plane waves, and the refraction (Cherenkov effect) or the diffraction (Smith-Purcell effect) of these waves produces the outgoing radiation. This approach permits in fact to link several phenomena involving electrons: the best known is of course the Cherenkov effect, which has been extensively studied and which gave rise to applications like Cherenkov detectors for high-velocity charged particles. Transition radiation [10] is observed when a charged particle crosses the interface between two media with different optical constants. In this case, the electromagnetic field of the electron is reflected at the surface. This effect has also been studied in great detail and is now widely used for charged beam monitoring and diagnostic [11]. X-ray production facilities using transition radiation are also planned [12]. Diffraction radiation is another example: a charged particle passes close to

an obstacle like a wedge, or through a hole in a foil: the environment suddenly changes for the moving particle [13]. If the perturbation is periodic, one observes Smith-Purcell radiation: the electromagnetic field of the electron is diffracted by the structure (an optical grating for example) and the periodicity of the phenomenon imposes a wavelength selection exactly as happens with light diffracted in a spectrometer. The diffraction and interference effects are also related to the Parametric X-ray production [14], observed when an electron hits a crystal and both the incident angle of the electron relative to a cristallographic axis as well as the observation angle fulfil the Bragg condition for a specific photon energy and for the crystal parameters.

In the case of the Smith-Purcell effect, a particular difficulty remained: the boundary problem related to electromagnetic wave diffraction by a periodic device was not solved at this time, except for some particular structures: Hessel [15] considered a planar grating with periodic surface reactance, the boundary problem being reduced to solving an infinite system of linear equation in which the spatial Fourier coefficients of the emitted radiation are the unknowns. He pointed out the presence of resonances similar to the Wood anomalies in grating theory [16]. The case of the plane strip grating was also solved rigorously, using the same technique [17]. The Wiener-Hopf technique [18] allows to solve the boundary value problem for a grating consisting of an infinite array of conducting semi-infinite screens of vanishing thickness. A quantum theory of the Smith-Purcell effect was also proposed [19]: the polarization of emitted light and the dispersion law are predicted, but the quantitative predictions are difficult. Bachheimer [20] applied the Rayleigh method in the theory of the reflection grating to the case of the Smith-Purcell radiation. The problem is then reduced to solving an infinite system of linear equations with the spatial Fourier coefficients as unknowns. It appeared however [21] that this method is not of general validity and even that one can not say a priori whether the method is valid or not. Barnes and Dedrick [22] used a Green function with the grating surface as boundary, represented the grating profile by its Fourier series and expanded the Green's function as a power series in the groove depth. The method is then a valid approximation when the wavelength is large compared to the local radius of curvature of the grating surface. Perturbation methods were also used [23].

Smith-Purcell radiation from structures other than gratings was also considered, like emission from electrons passing through an helix [24]. In that case, the diffractive structure is not open and the treatment is similar to the one applied in electronic tube theory. The interest of using a bunched beam in order to observe coherence effects in the beam and by this way to enhance the emission was pointed out [25]. Smith-Purcell radiation from finite-length structures was also considered, experimentally [26] and theoretically [27], but few results are available.

The first complete and rigorous treatment of the Smith-Purcell radiation has been given by Van den Berg [28]. From the point of view of Toraldo di Francia [8], the evanescent waves constituting the three-dimensional spatial Fourier spectrum of the moving charge illuminate the diffraction grating [29]. The propagating reflected spectral orders constitute the Smith-Purcell radiation. It is shown that the vectorial electromagnetic problem can be reduced to two two-dimensional scalar problems. Employing a Green's function formulation of the problem, Van den Berg derives integral equations of the second kind for the unknown functions on the grating surface. The solutions are recombined to yield the complete vector solution. The method is valid for an arbitrary periodic profile. For a particular type of grating, with

rectangular profile, Van den Berg [30] also derived a modal expansion method, using Deryugin's treatment [31], to calculate the Smith-Purcell radiation produced by a line charge moving over the grating. Geometrical considerations show that in the plane perpendicular to the grating rulings, the result is the same as for a point charge, so this approach can be used to calculate the Smith-Purcell radiation from a point charge in this particular configuration [32]. The Van den Berg model is however limited to perfectly conducting surfaces. Very few attempts have been made to predict Smith-Purcell radiation for dielectric [33][34] or metallic gratings. Bachheimer [35] used the Rayleigh hypothesis for shallow grating and was able to predict peculiar behaviour of the radiated light, related with surface plasmons. The experiments he carried out [36] confirmed his predictions. A theory for low relativistic electrons and emission near the plasma frequency of the grating matter was also derived [37].

All the previous theories assume that the charge is moving perpendicular to the grating rulings. Bachheimer [20] showed that using a beam moving at a certain angle with respect to the grooves (but still parallel to the grating surface) offers an easy way to tune the emitted radiation because the period as seen by the moving electron changes. No rigorous theory has yet been written to treat this case. The purpose of this work is to develop such a theory.

In the first chapter, the starting point of view of Toraldo di Francia [8] is used in conjunction with the method of Van den Berg [29] for perfectly conducting surfaces to calculate the radiated intensity. Qualitative results are presented for metallic gratings. In the second chapter, some of the now available theories to solve the grating problem are presented.

The third chapter is dedicated to the presentation of theoretical predictions of Smith-Purcell radiation emitted by relativistic electrons in the range of 1 MeV to 100 MeV interacting with several common types of gratings. A practical Smith-Purcell source is discussed.

A radiation physics program started 5 years ago at the Institute for Reference Materials and Measurements (IRMM) at Geel by the upgrade of a photo-activation facility which was installed in the early seventies, using bremsstrahlung radiation produced in a thick tungsten target. Small samples could be send to this facility for irradiation using a pneumatic system. After a proper time of irradiation and dose rate the samples were sent back to the laboratory for analysis. A study using 40 MeV electrons has been carried out to characterize X-ray transition radiation produced by electrons interacting with different kinds of radiators [12]. This study lead to the decision of installing a large laboratory dedicated to radiation physics outside the target hall where a transition radiation source will be installed. Theoretical estimates show that using the rejuvenated GELINA accelerator such a source could be orders of magnitude stronger than conventional bremsstrahlung sources and that the brightness and the tunability of transition radiation can lead to an effective tool for surface and interface physics. The use of Smith-Purcell radiation was suggested by L.Wartski and will be foreseen in the new laboratory. At the GELINA facility, which is described in chapter four, experiments using electrons interacting with a grating have been carried out. The results of these experiments are presented in chapter five.

# CHAPTER 1 Theoretical description of the Smith-Purcell effect

The Smith-Purcell radiation emitted by electrons moving parallel to a periodic surface has been widely studied, either from the theoretical or the experimental point of views. Several theories have been developed, among which the electromagnetic theory proposed by Van den Berg [29] proved to fit best with experimental data, as shown by Gover *et al.* [38] who compared different models. This theory assumes however electrons moving perpendicularly to the grating rulings. In the next paragraphs, an extension of the model taking into account an arbitrary tilting angle is being developed.

## 1.1 Formulation of the problem

### 1.1.1 The field of the moving electron

Figure 1.1 gives the geometry of the configuration of a Smith-Purcell experiment. The electric point charge is moving in vacuum, parallel to a reflection grating with an electrically perfect conducting surface. The grating is periodic in the x direction of a cartesian coordinate system, the y direction being parallel to the grating rulings and the grating top plane lies in the (x-y) plane. The charge moves along a trajectory $z=z_0=\text{const}$ and $\Psi_1$ is the angle between the x axis and the projection of the trajectory onto the (x-y) plane. The electron moves with constant velocity $\boldsymbol{v}_0 = v_0 \cos\Psi_1 \boldsymbol{i}_x + v_0 \sin\Psi_1 \boldsymbol{i}_y$.

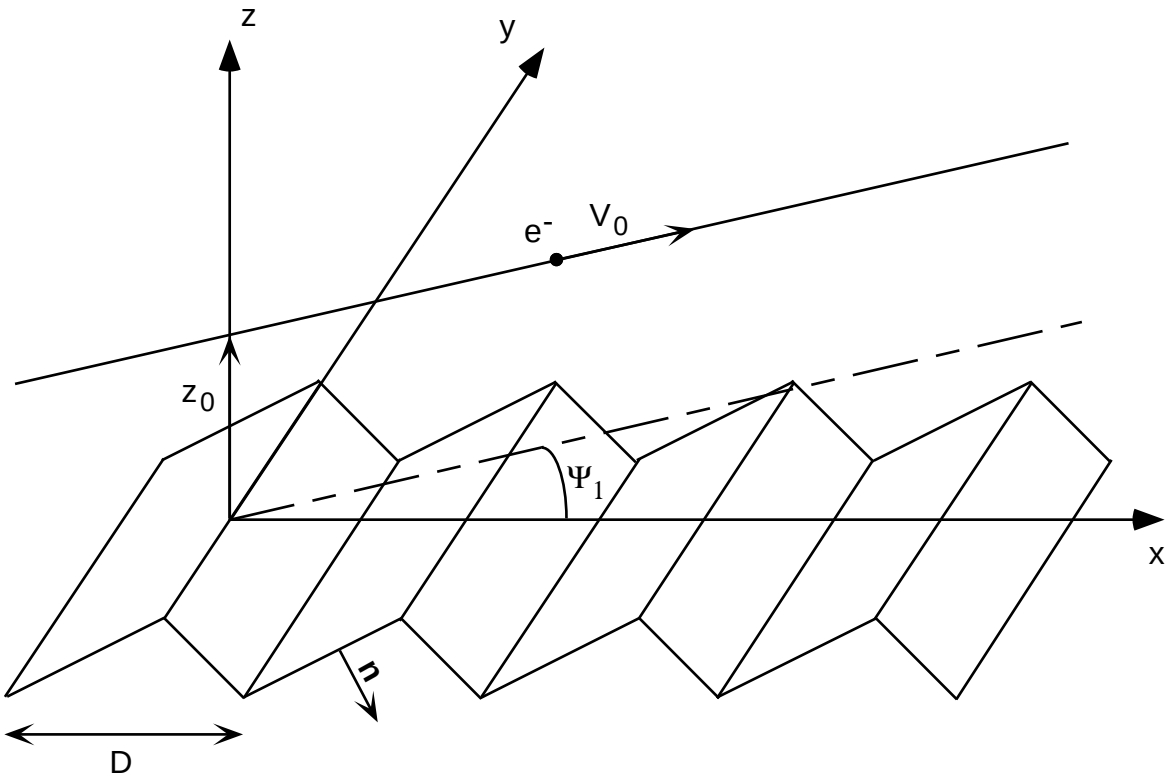


**FIGURE 1.1 : Configuration of a Smith-Purcell experiment.**

Similarly to Van den Berg [29], the fields of the moving charge $\mathbf{E}^i=\mathbf{E}^i(x,y,z,t)$, $\mathbf{H}^i=\mathbf{H}^i(x,y,z,t)$ are represented by Fourier integrals:

$$\begin{aligned}\mathbf{E}^i(x,y,z,t) &= (2\pi)^{-2}\int_{-\infty}^{\infty} d\omega \int_{-\infty}^{\infty} \boldsymbol{E}^i(x,z;\beta,\omega)\, exp\,(i\beta y - i\omega t)\, d\beta \\ \mathbf{H}^i(x,y,z,t) &= (2\pi)^{-2}\int_{-\infty}^{\infty} d\omega \int_{-\infty}^{\infty} \boldsymbol{H}^i(x,z;\beta,\omega)\, exp\,(i\beta y - i\omega t)\, d\beta\end{aligned} \qquad (1.1)$$

Since the fields are real and only positive values of ω are considered, Eqs. ( 1.1 ) are rewritten as:

$$\begin{aligned}\mathbf{E}^i(x,y,z,t) &= (2\pi^2)^{-1} Re\left(\int_{0}^{\infty} d\omega \int_{-\infty}^{\infty} \boldsymbol{E}^i(x,z;\beta,\omega)\, exp\,(i\beta y - i\omega t)\, d\beta\right) \\ \mathbf{H}^i(x,y,z,t) &= (2\pi^2)^{-1} Re\left(\int_{0}^{\infty} d\omega \int_{-\infty}^{\infty} \boldsymbol{H}^i(x,z;\beta,\omega)\, exp\,(i\beta y - i\omega t)\, d\beta\right)\end{aligned} \qquad (1.2)$$

The Fourier components satisfy the Maxwell equations:

$$(\nabla + i\beta \boldsymbol{i}_y) \times \boldsymbol{H}^i + i\omega\varepsilon_0 \boldsymbol{E}^i = \boldsymbol{J}$$
$$(\nabla + i\beta \boldsymbol{i}_y) \times \boldsymbol{E}^i - i\omega\mu_0 \boldsymbol{H}^i = 0 \qquad (1.3)$$

with $\nabla = \partial_x \boldsymbol{i}_x + \partial_z \boldsymbol{i}_z$ and $\boldsymbol{J} = \boldsymbol{J}(x, z; \beta, \omega)$ being the Fourier transform of the current density distribution:

$$\boldsymbol{J}(x, z; \beta, \omega) = \int_{-\infty}^{\infty} dt \int_{-\infty}^{\infty} \mathbf{J}(x, y, z, t)\, exp(-i\beta y + i\omega t)\, dy \qquad (1.4)$$

The charge moves in the plane $z=z_0$ with velocity $\boldsymbol{v}_0 = v_0 \cos\Psi_1 \boldsymbol{i}_x + v_0 \sin\Psi_1 \boldsymbol{i}_y$. Therefore, the electric-current density is written as:

$$\mathbf{J}(x, y, z, t) = qv_0 \cos\Psi_1 \delta(x - v_0 \cos\Psi_1 t, y - v_0 \sin\Psi_1 t, z - z_0)\, \boldsymbol{i}_x$$
$$+ qv_0 \sin\Psi_1 \delta(x - v_0 \cos\Psi_1 t, y - v_0 \sin\Psi_1 t, z - z_0)\, \boldsymbol{i}_y \qquad (1.5)$$

in which $q=-e$ is the electron charge. From Eqs. ( 1.4 ) and ( 1.5 ), $\boldsymbol{J}(x, z; \beta, \omega)$ is obtained as :

$$\boldsymbol{J}(x, z, \beta, \omega) = q\delta(z - z_0) exp\left( (i\omega - i\beta v_0 \sin\Psi_1) \frac{x}{v_0 \cos\Psi_1} \right) \boldsymbol{i}_x$$
$$+ q\delta(z - z_0) \tan\Psi_1 exp\left( (i\omega - i\beta v_0 \sin\Psi_1) \frac{x}{v_0 \cos\Psi_1} \right) \boldsymbol{i}_y \qquad (1.6)$$

The Maxwell equations are expressed for each components as:

$$i\beta H_z - \partial_z H_y + i\omega\varepsilon_0 E_x = J_x \qquad (1.7)$$

$$\partial_z H_x - \partial_x H_z + i\omega\varepsilon_0 E_y = J_y \qquad (1.8)$$

$$\partial_x H_y - i\beta H_x + i\omega\varepsilon_0 E_z = 0 \qquad (1.9)$$

and

$$i\beta E_z - \partial_z E_y - i\omega\mu_0 H_x = 0 \qquad (1.10)$$

$$\partial_z E_x - \partial_x E_z - i\omega\mu_0 H_y = 0 \qquad (1.11)$$

$$\partial_x E_y - i\beta E_x - i\omega\mu_0 H_z = 0 \qquad (1.12)$$

Through Eqs. ( 1.7 ) - ( 1.12 ) the x and z components of the Fourier field vectors $\boldsymbol{E}^i$ and $\boldsymbol{H}^i$ can be expressed as functions of their $E_y^i$ and $H_y^i$ components (from now on, when there is no possible confusion, a field A(x,z,β,ω) will sometimes be simply written A).

Furthermore, $E_y^i$ and $H_y^i$ satisfy the two-dimensional Helmholtz equations. To obtain these equations, the formula $rot\,(rot) \;=\; grad\,(div) \;-\Delta$ is applied to the Maxwell equations.

For $\boldsymbol{H}^i$, with $\boldsymbol{div}\boldsymbol{H}^i \;=\; 0$ the following equation is obtained:

$$(-\partial_x^2 - \partial_z^2 + \beta^2)\,\boldsymbol{H}^i + i\omega\varepsilon_0 i\omega\mu_0 \boldsymbol{H}^i \;=\; (\nabla + i\beta \boldsymbol{i}_y) \times \boldsymbol{J} \qquad (1.13)$$

which gives for the y component:

$$(\partial_x^2 + \partial_z^2)\,H_y^i + \,(k_0^2 - \beta^2)\,H_y^i \;=\; -\partial_z J_x \qquad (1.14)$$

with $k_0 \;=\; \omega_0 / c_0$. For the y component of $\boldsymbol{E}^i$, with $\boldsymbol{div}\boldsymbol{E}^i \;=\; \partial_x E_x^i + i\beta E_y^i + \partial_z E_z^i$ and combining with the Maxwell equations, the following expression is obtained:

$$i\omega\varepsilon\,(\partial_x E_x^i + i\beta E_y^i + \partial_z E_z^i) \;=\; \partial_x J_x + i\beta J_y$$

Applying $rot\,(rot) \;=\; grad\,(div) \;-\Delta$ to the Maxwell equations gives for $\boldsymbol{E}^i$:

$$\boldsymbol{grad}\,(\boldsymbol{div}\boldsymbol{E}^i) \;-\Delta\boldsymbol{E}^i - i\omega\mu_0\,(\boldsymbol{J} - i\omega\varepsilon_0 \boldsymbol{E}^i) \;=\; 0 \qquad (1.15)$$

So that for the y component, after substitution of $\boldsymbol{div}\boldsymbol{E}^i$ by the expression derived above, the equation is:

$$(\partial_x^2 + \partial_z^2)\,E_y^i + \,(k_0^2 - \beta^2)\,E_y^i \;=\; -\,i\omega\mu_0 J_y + \frac{\beta}{\omega\varepsilon_0}\,(\partial_x J_x + i\beta J_y) \qquad (1.16)$$

We obtain the solutions of these equations as:

$$H_y^i \;=\; -\frac{1}{2} q \cdot sign\,(z - z_0) \;\cdot exp\,(i\alpha_0 x + i\gamma_0 |z - z_0|) \qquad (1.17)$$

$$E_y^i \;=\; E1_y^i + E2_y^i \qquad (1.18)$$

with

$$\begin{aligned} E1_y^i \;&=\; \frac{1}{2} q \left(\frac{\mu_0}{\varepsilon_0}\right)^{1/2} \frac{\beta}{k_0} \frac{\alpha_0}{\gamma_0} \cdot exp\,(i\alpha_0 x + i\gamma_0 |z - z_0|) \\ E2_y^i \;&=\; \frac{1}{2\gamma_0} q \left(-\mu_0\omega + \frac{\beta^2}{\omega\varepsilon_0}\right) \tan\Psi_1 \, exp\,(i\alpha_0 x + i\gamma_0 |z - z_0|) \end{aligned} \qquad (1.19)$$

in which:

$$\begin{aligned} \alpha_0 &= \frac{\omega - \beta v_0 \sin\Psi_1}{v_0 \cos\Psi_1} \\ \gamma_0 &= i\,(\alpha_0^2 + \beta^2 - k_0^2)^{1/2} \text{ with } (\alpha_0^2 + \beta^2 - k_0^2)^{1/2} \geq 0 \end{aligned} \qquad (1.20)$$

As a consequence of the limited speed of the electron, $c_0 > v_0$ and $\alpha_0^2 + \beta^2 > {k_0}^2$. Therefore, $\gamma_0$ is imaginary and Eqs. ( 1.17 ) and ( 1.19 ) represent evanescent plane waves decaying exponentially in the direction away from the trajectory plane $z=z_0$. In absence of any perturbing device, the free electron moving in empty space does not radiate. If a perturbation is applied to this field, evanescent waves can become propagative, as in the Cerenkov effect when the waves are refracted by a medium of index n. If the electron moves close to a grating, the evanescent waves are diffracted by the grating and give rise to propagating reflected waves which constitute the Smith-Purcell radiation. Therefore, the calculation of the Smith-Purcell spectra is reduced to the calculation of the amplitudes of the diffracted waves, a problem referred to as the *grating problem*, and may be solved by the same techniques. The only difference is the nature of the incoming plane wave, which is in this case evanescent.

### 1.1.2 The reflected field

The reflected field is given by $\mathbf{E}^r = \mathbf{E} - \mathbf{E}^i$ and $\mathbf{H}^r = \mathbf{H} - \mathbf{H}^i$, with $\mathbf{E}=\mathbf{E}(x,y,z,t)$ and $\mathbf{H}=\mathbf{H}(x,y,z,t)$ being the total field above the grating. These reflected fields are also expanded as Fourier integrals $\boldsymbol{E}^r(x,z,\beta,\omega)$ and $\boldsymbol{H}^r(x,z,\beta,\omega)$ which satisfy the source-free Maxwell equations

$$\begin{aligned} (\nabla + i\beta \mathbf{i}_y) \times \boldsymbol{H}^r + i\omega\varepsilon_0 \boldsymbol{E}^r = 0 \\ (\nabla + i\beta \mathbf{i}_y) \times \boldsymbol{E}^r - i\omega\mu_0 \boldsymbol{H}^r = 0 \end{aligned} \qquad (1.21)$$

and a boundary condition at the surface. For a perfectly conducting surface this boundary condition is written as:

$$\mathbf{n} \times (\boldsymbol{E}^i + \boldsymbol{E}^r) = 0 \qquad (1.22)$$

in which **n** is the unit vector normal to the surface pointing into it (see figure 1.1).

As for the incident field, from the Maxwell equations one can show that the x- and z-components of the electric and magnetic reflected fields can be expressed in terms of $E_y^r$ and $H_y^r$. Neither the Helmholtz equations nor the boundary conditions lead to a coupling between $E_y$ and $H_y$ and the three-dimensional vectorial problem can be separated into two scalar problems of two dimensions called the two fundamental cases of polarization, viz. the E-polarization and the H-polarization.

For the E-polarization case, $E_y \neq 0$ , $H_y = 0$ the Helmholtz equation for the reflected field $E_y^r$ is:

$$(\partial_x^2 + \partial_z^2)\, E_y^r + (k_0^2 - \beta^2)\, E_y^r = 0 \qquad (1.23)$$

with the boundary condition for the total field on the surface of the grating:

$$E_y = 0 \qquad (1.24)$$

For the H-polarization case, where $H_y \neq 0$ and $E_y = 0$ the reflected field $H_y^r$ satisfies:

$$(\partial_x^2 + \partial_z^2)\, H_y^r + (k_0^2 - \beta^2)\, H_y^r = 0 \qquad (1.25)$$

The total field satisfies the boundary condition:

$$\mathbf{n} \cdot \nabla H_y = 0 \tag{1.26}$$

From physical considerations the existence of a solution is assumed and a supplemental condition is introduced: the reflected field must be made up of outgoing waves, propagating away from the grating and must be bounded for $z \to \infty$. This is called the radiation condition [39].

Let $E_y^r(x, z;\beta, \omega)$ and $H_y^r(x, z;\beta, \omega)$ be solutions for the reflected fields. It is straightforward to show that these solutions are unique. Moreover, because $exp(-i\alpha_0 x)\, E_y^i$ and $exp(-i\alpha_0 x)\, H_y^i$ are periodic in x and the boundary condition is also periodic in x, the quantities $exp(-i\alpha_0 x)\, E_y^r$ and $exp(-i\alpha_0 x)\, E_y^r$ are also periodic in x. They are represented as Fourier series and the reflected fields are written as:

$$\begin{aligned} E_y^r(x, z;\beta, \omega) &= \sum_{n=-\infty}^{\infty} E_{y,n}^r(z;\beta, \omega)\, exp(i\alpha_n x) \\ H_y^r(x, z;\beta, \omega) &= \sum_{n=-\infty}^{\infty} H_{y,n}^r(z;\beta, \omega)\, exp(i\alpha_n x) \end{aligned} \tag{1.27}$$

with:

$$\alpha_n = \alpha_0 + 2\pi n / D \tag{1.28}$$

These expressions are inserted in the Helmholtz equations. For $0 < z < \infty$ the orthogonality of the functions $exp(i\alpha_n x)$ on an interval $x_1 \le x \le x_1 + D$ gives:

$$\begin{aligned} \partial_z^2 E_{y,n}^r(z;\beta, \omega) + \gamma_n^2 E_{y,n}^r(z;\beta, \omega) &= 0 \\ \partial_z^2 H_{y,n}^r(z;\beta, \omega) + \gamma_n^2 H_{y,n}^r(z;\beta, \omega) &= 0 \end{aligned} \tag{1.29}$$

with:

$$\gamma_n^2 = k_0^2 - \beta^2 - \alpha_n^2 \tag{1.30}$$

Above the grating, the radiation condition obliges to consider only the solutions:

$$\begin{aligned} E_{y,n}^r(z;\beta, \omega) &= E_{y,n}^r(\beta, \omega)\, exp(i\gamma_n z) \\ H_{y,n}^r(z;\beta, \omega) &= H_{y,n}^r(\beta, \omega)\, exp(i\gamma_n z) \end{aligned} \tag{1.31}$$

with $Re(\gamma_n) \ge 0$ and $Im(\gamma_n) \ge 0$. From the mathematical point of view, the solutions involving an $exp(-i\gamma_n z)$ dependence are also valid. They have to be rejected, because for $\gamma_n^2 \ge 0$ they would represent waves propagating into the grating and for $\gamma_n^2 < 0$ and $z \to \infty$ the amplitude of the wave would become infinite.

Then the diffracted field above the grating can be written as an infinite sum of outgoing progagative or evanescent plane waves:

$$E_y^r(x, z;\beta, \omega) = \sum_{n=-\infty}^{\infty} E_{y,n}^r(\beta, \omega)\, exp(i\alpha_n x + i\gamma_n z)$$
$$\text{for } 0 < z < \infty \qquad (1.32)$$
$$H_y^r(x, z;\beta, \omega) = \sum_{n=-\infty}^{\infty} H_{y,n}^r(\beta, \omega)\, exp(i\alpha_n x + i\gamma_n z)$$

in which $\alpha_n = \alpha_0 + 2\pi n/D$ and $\gamma_n = (k_o^2 - \beta^2 - \alpha_n^2)^{1/2}$ with $Re(\gamma_n) \geq 0$ and $Im(\gamma_n) \geq 0$.

It seems that Lord Rayleigh [40] was the first who used these expansions for the "classical" diffraction of radiation in spectroscopy. Therefore, Eqs. ( 1.32 ) are called the "Rayleigh expansions".

### 1.1.3 Solution of the grating problem

The incident field generated by a moving electron has been calculated. The calculation of the Smith-Purcell radiation is a special case of diffraction by a grating. It is worthwhile to note that the validity of the Rayleigh expansion has been established only for $0 < z < \infty$ because the differential equation system ( 1.29 ) has been proved only in this part of the space. In other terms, except for the boundary conditions, no information about the field inside the grooves of the grating is available up to now.

On the other hand, the demonstration of the Rayleigh expansion does not refer to the boundary conditions. It is valid whatever the grating profile is, even for non-analytic profile like semi-infinite screens of vanishing thickness, and whatever the grating material is (perfectly conducting surface, metallic or dielectric material). Only the method to find the value of the Rayleigh coefficients has to be adapted to the grating peculiarities.

The next step is to solve this "grating problem" in order to find the coefficients of the Rayleigh expansions giving the reflected field above the grating. For the moment, no details will be given for this part of the problem, which will be explained in detail in the chapter 2. In the following it is assumed that given the different parameters for the electron (trajectory, speed) and the grating geometry, the grating problem has been solved and the Rayleigh coefficients are known.

## 1.2 The Smith-Purcell spectra

In practice, a detector will always be placed at a distance from the grating much larger than the distance between the electron and the grating, than the grating period, and much larger than one wavelength. This means that neither the evanescent field of the electron hitting directly the detector will be detected, nor the evanescent waves of the Rayleigh expansion.

This simply means that only the far field will be detected. Then, the Smith-Purcell radiation is made up of the emerging propagating waves, i.e. those waves for which $Im(\gamma_n) = 0$.

Therefore, one must have:

$$\alpha_n^2 + \beta^2 \le k_0^2 \qquad (1.33)$$

As a first consequence, for propagative waves the parameter $\beta$ is restricted to $-k_0 \le \beta \le k_0$. Then it is easy to see from ( 1.20 ) that $\alpha_0 > k_0$.

Since $\alpha_n = \alpha_0 + 2\pi n/D$ and $\gamma_n^2 = k_0^2 - \beta^2 - \alpha_n^2$, only some of the negative orders n<0 from the Rayleigh expansions are propagative and contribute to the SP spectra. Fig. 1.2 gives a simple graphical illustration of the condition for a wave of spectral order -1 to be propagative by constructing the intersection between the plane described by Eqs. ( 1.20 ), ( 1.28 ) and the cone described by Eq. ( 1.33 ):

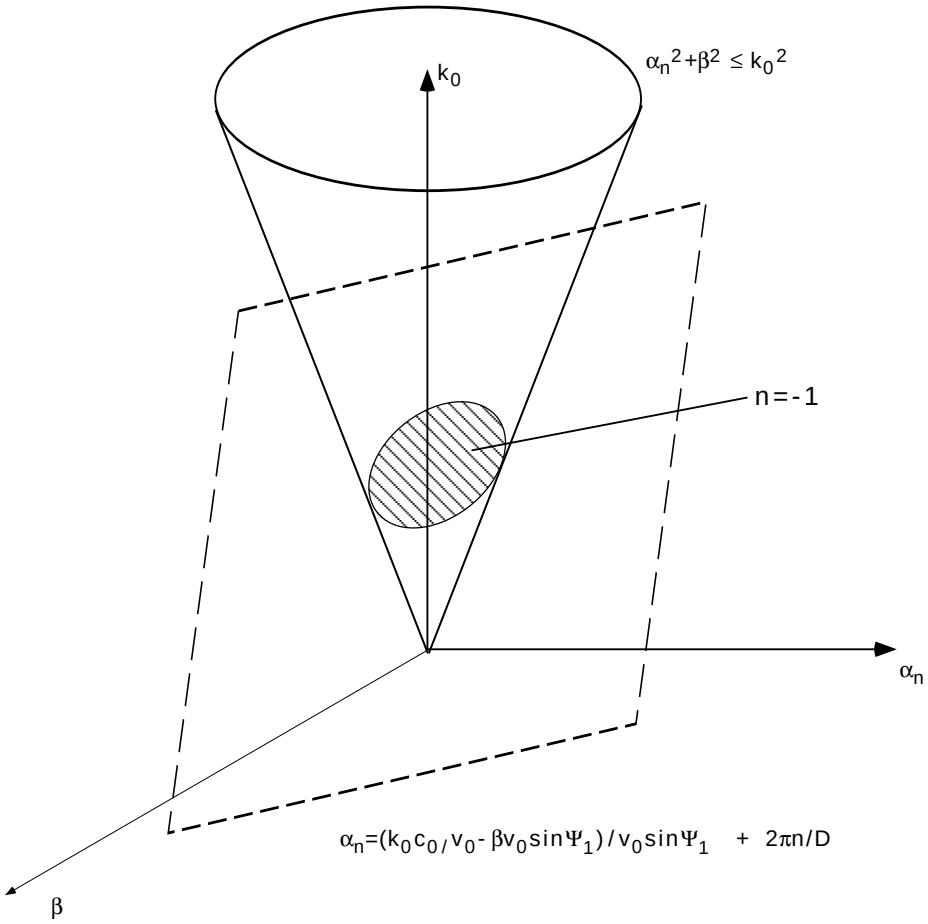


**FIGURE 1.2 : Graphical construction illustrating the condition for a diffracted wave to be propagative for diffraction order n=-1.**

First, waves resulting from the diffraction of an incident wave with fixed parameters $k_0$ and $\beta$ will be considered. It is then natural to define a set of angles of emergence $(\Phi,\Theta_n)$ in relation to the quantities $\alpha_n,\beta,\gamma_n$ such that:

$$\begin{aligned} \alpha_n &= -k_0 \sin\Phi \sin\Theta_n \\ \beta &= k_0 \cos\Phi \\ \gamma_n &= k_0 \sin\Phi \cos\Theta_n \end{aligned} \qquad (1.34)$$

with $-\pi/2 \le \Theta_n \le \pi/2$ and $0 \le \Phi \le \pi$

This set of angles is useful to understand one peculiar aspect of the Smith-Purcell effect. For an incident wave with parameters $k_0,\alpha_0,\beta,\gamma_0$ the corresponding propagative diffracted waves with parameters $\alpha_n,\beta,\gamma_n$ are located on a cone. Fig. 1.3 illustrates the construction of the emerging waves for the different diffraction orders n. The Smith-Purcell effect is a case of conical diffraction. When using conical diffraction mounting in spectroscopy, the parameters of the incident wave $k_0,\alpha_0,\beta,\gamma_0$ are fixed by the experiment. In the Smith-Purcell case, for a fixed $k_0$ all values of $-k_0 \le \beta \le k_0$ are possible. This means that for each value of $\beta$ there corresponds one cone for the different orders of diffraction.

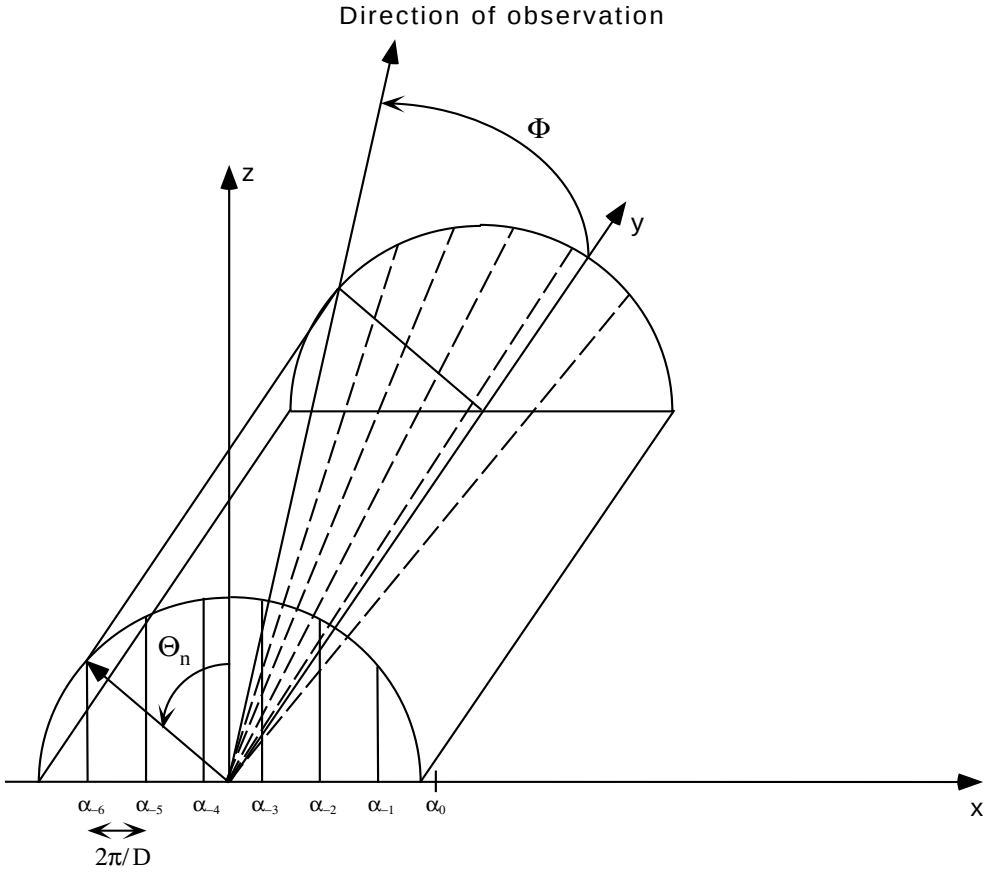


**FIGURE 1.3 : The direction of emergence of a radiating wave of order n in the $(\Theta_n,\Phi)$ reference frame.**

The wavelength $\lambda = 2\pi/k_0$ of the n$^{th}$ order is given by the dispersion relation:

$$\lambda = \frac{-D}{n\cos\Psi_1}\left(c_0/v_0 - \cos\Phi\sin\Psi_1 - \cos\Psi_1\sin\Phi\sin\theta_n\right) \qquad (1.35)$$

Considering waves with fixed parameter $k_0$ (the parameters $\beta$,$\alpha_0$ and $\gamma_0$ being free), this relation can be simplified introducing angles of emergence ($\theta_n$,$\varphi_n$) with:

$$\begin{aligned} \alpha_n &= k_0\left(\cos\Psi_1\cos\theta_n - \sin\Psi_1\sin\theta_n\sin\varphi_n\right) \\ \beta &= k_0\left(\sin\Psi_1\cos\theta_n + \cos\Psi_1\sin\theta_n\sin\varphi_n\right) \\ \gamma_n &= k_0\sin\theta_n\cos\varphi_n \end{aligned} \qquad (1.36)$$

with $0 \le \theta_n \le \pi$ and $-\pi/2 \le \varphi_n \le \pi/2$

From Eqs. (1.20), (1.32) and (1.36) the following relation is obtained for the wavelength:

$$\lambda = \frac{-D}{n\cos\Psi_1}\left(c_0/v_0 - \cos\theta_n\right) \qquad (1.37)$$

Fig. 1.4 gives a geometrical construction of the emerging waves in this new reference frame. In the drawing, the considered direction of observation is characterized by $\varphi_n \le 0$.

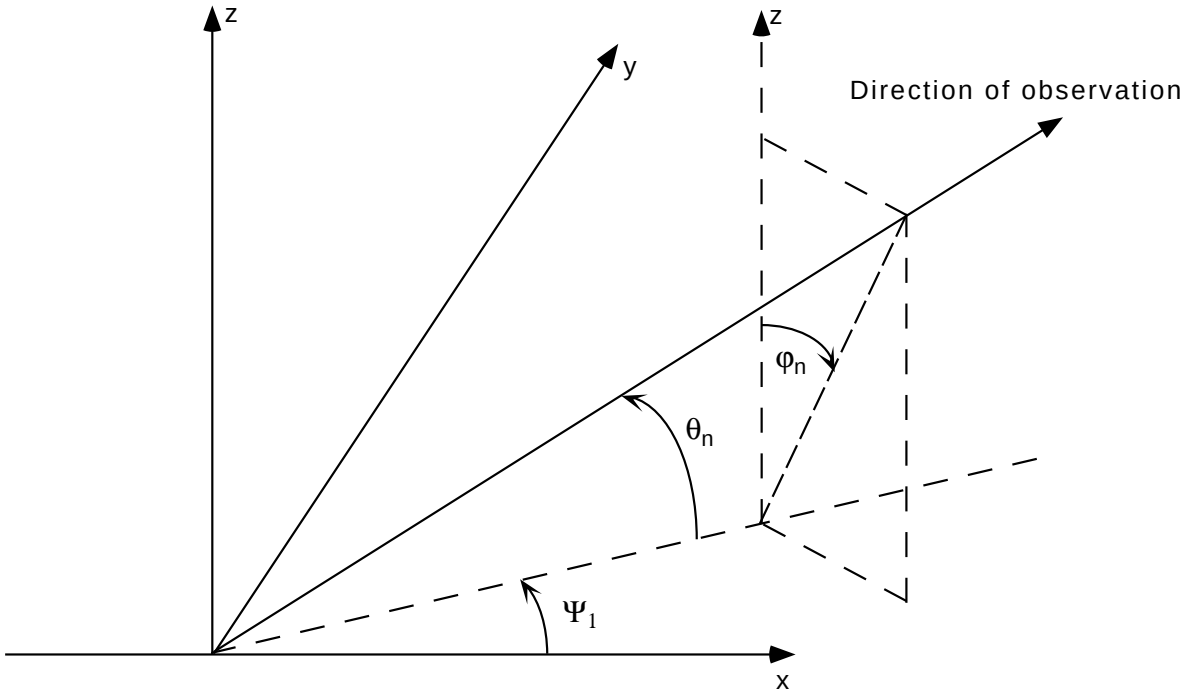


**FIGURE 1.4 : The direction of emergence of a radiating wave of order n in the ($\theta_n$,$\varphi_n$) reference frame.**

This shows that radiation of constant wavelength is emitted along a cone of aperture $\theta_n$ the axis being the projection of the electron trajectory onto the (x-y) plane. Rotating the grating around the z axis (i.e. changing the angle $\Psi_1$) changes the apparent grating period seen by the electron and Eq. ( 1.37 ) shows that continuous wavelength tuning is possible without changing the electron speed, nor the direction of observation contrary to Smith-Purcell radiation produced by electrons moving perpendicular to the grating rulings [2][7][20].

In previous calculations of the Smith-Purcell radiation [29] a different set of angles ($\eta_n$, $\zeta_n$) was used for the emerging waves. Figure 1.5 gives a geometrical construction of the emerging waves. With this set of angles, one has:

$$\begin{aligned} \alpha_n &= k_0 \sin\eta_n \\ \beta &= k_0 \cos\eta_n \sin\zeta_n \\ \gamma_n &= k_0 \cos\eta_n \cos\zeta_n \end{aligned} \qquad (1.38)$$

with $-\pi/2 \le \eta_n \le \pi/2$ and $-\pi/2 \le \zeta_n \le \pi/2$

The dispersion relation in this reference frame is given by:

$$\frac{-n\lambda_0}{D} = \frac{c_0}{v_0 \cos\Psi_1} - \sin\eta_n - \cos\eta_n \sin\zeta_n \tan\Psi_1 \qquad (1.39)$$

Rewriting these relations for the particular case $\Psi_1 = 0$ gives the well known dispersion formula given by Van den Berg and other authors:

$$\lambda = \frac{-D}{n}(c_0/v_o - \sin\eta_n) \qquad (1.40)$$

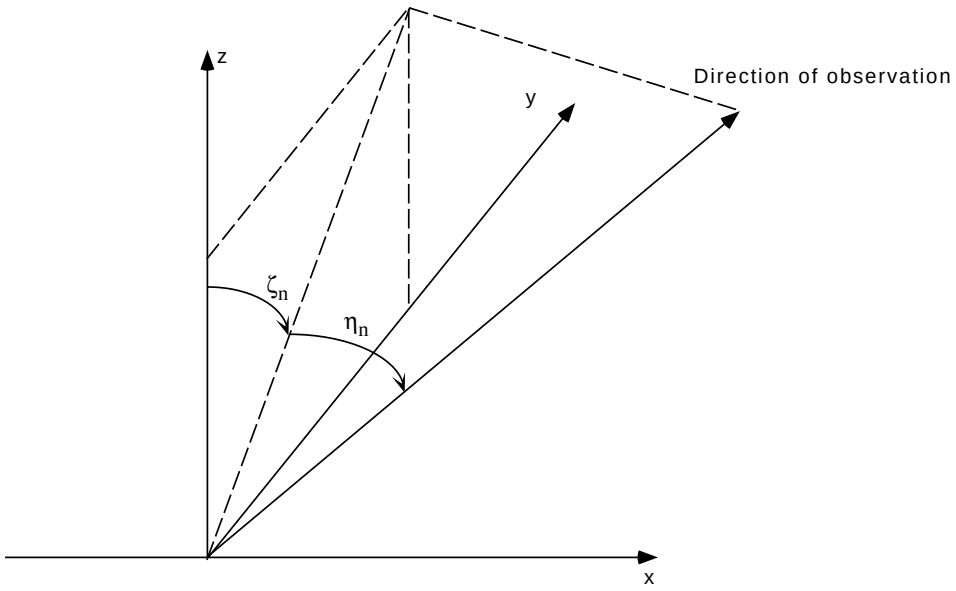


**FIGURE 1.5 : The direction of emergence of a radiating wave of order n in the ($\zeta_n$,$\eta_n$) reference frame. In this example $\eta_n \ge 0$.**

## 1.3 Some properties of the Smith-Purcell spectra

### 1.3.1 Lemma

Before calculating the power radiated due to the Smith-Purcell mechanism some important results will be established, which will be useful to check the results obtained when solving the grating problem.

Let S be a periodic perfectly conducting surface with period D, described by $z = f(x)$. Let $U$ and $U'$ be two functions satisfying the Helmholtz equation and one of the boundary conditions ( 1.24 ), ( 1.26 ).

$$\left.\begin{aligned}\nabla^2 U + k_0^2 U = 0 \\ \nabla^2 U' + k_0^2 U' = 0\end{aligned}\right\} \quad \text{when } f(x) < z \tag{1.41}$$

As a consequence:

$$U'\nabla^2 U - U\nabla^2 U' = 0 \text{ when } f(x) < z \tag{1.42}$$

Applying the two dimensional Green's theorem to a domain S inside the closed contour C described in Fig. 1.6, the following equation is obtained:

$$\iint_S (U\nabla^2 U' - U'\nabla^2 U)\, dS = \oint_C \{ U(\boldsymbol{n} \cdot \nabla U') - U'(\boldsymbol{n} \cdot \nabla U) \}\, ds = 0 \tag{1.43}$$

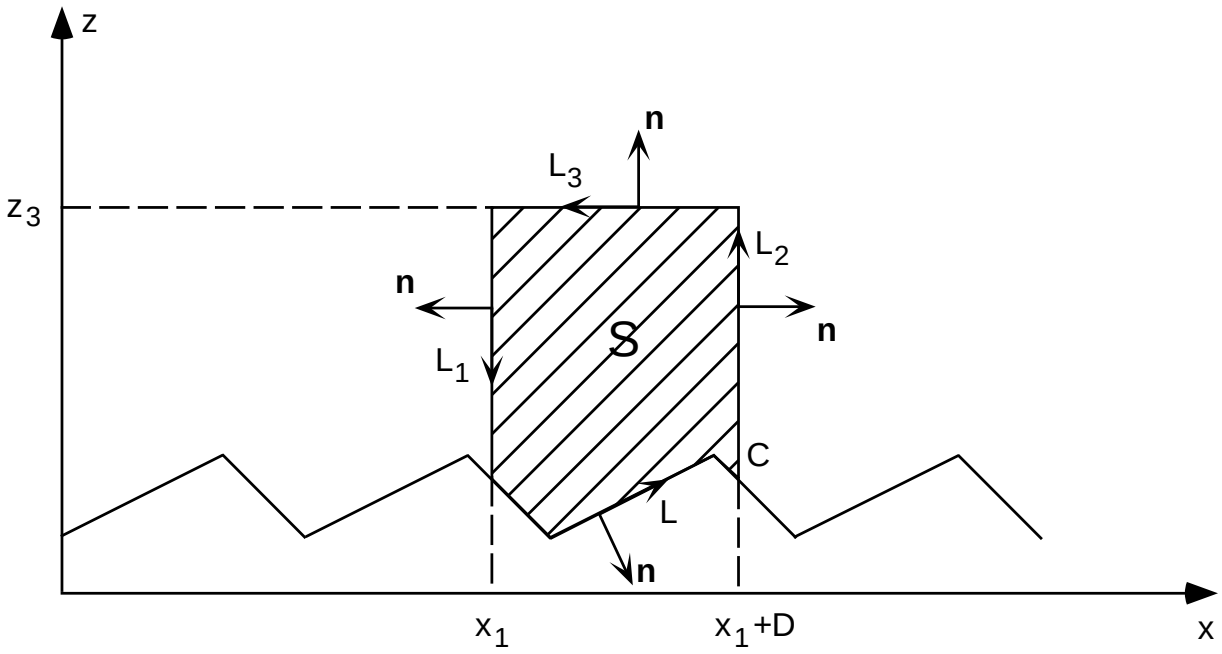


**FIGURE 1.6 : Domain to which Green's theorem is applied.**

Taking into account the boundary conditions, the contribution from L to the integrals in equation ( 1.43 ) vanishes.

On account of the periodicity of $exp\,(-i\alpha_0 x)\,E_y$ and $exp\,(-i\alpha_0 x)\,H_y$ , the contributions from $L_1$ and $L_2$ to the integral ( 1.43 ) cancel.

As a consequence, only the contribution from $L_3$ remains in the contour integration:

$$\int_{x_1}^{x_1+D} \{U\partial_z U' - U'\partial_z U\}\,dx \;=\; 0 \;\text{ when }(0 < z < z_0) \qquad (1.44)$$

This lemma is useful in demonstrating some properties of the Smith-Purcell radiation [29][39].

## 1.3.2 Two complementary experiments

Let us consider the two following Smith-Purcell experiments described on Fig. 1.7. The electron moves with a speed $\boldsymbol{v}_0 = v_0\cos\Psi_1\boldsymbol{i}_x + v_0\sin\Psi_1\boldsymbol{i}_y$ in the first case and with a speed $\boldsymbol{v}'_0 = -\boldsymbol{v}_0$ in the second case. All other parameters remain the same.

The electric field above the grating is given in the first case by:

$$E_y = \frac{1}{2}q\left(\frac{\mu_0}{\varepsilon_0}\right)^{1/2}\frac{\beta}{k_0}\frac{\alpha_0}{\gamma_0}\cdot exp\,(i\alpha_0 x - i\gamma_0\,(z-z_0))$$

$$+\frac{q}{2\gamma_0}\left(-\mu_0\omega + \frac{\beta^2}{\omega\varepsilon_0}\right)\tan\Psi_1\,exp\,(i\alpha_0 x - i\gamma_0\,(z-z_0)) + \sum_{n=-\infty}^{\infty} E^r_{y,n}\,exp\,(i\alpha_n x + i\gamma_n z)$$

$$\text{when }(0 < z < z_0) \qquad (1.45)$$

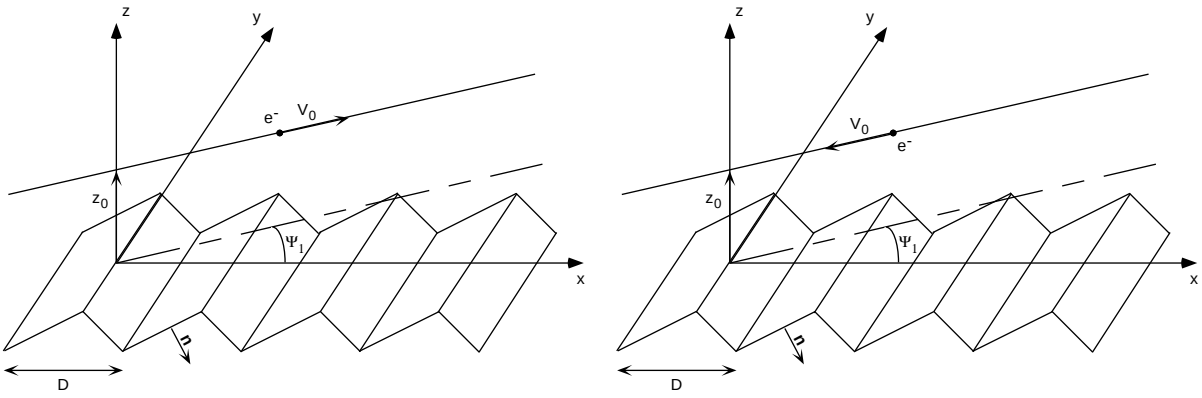


**FIGURE 1.7 : Two complementary Smith-Purcell experiments.**

The magnetic field is written as:

$$H_y = \frac{1}{2} q exp\left(i\alpha_0 x - i\gamma_0 (z - z_0)\right) + \sum_{n=-\infty}^{\infty} H^r_{y,n} exp\left(i\alpha_n x + i\gamma_n z\right) \quad when\ (0 < z < z_0) \qquad (1.46)$$

In the second case, it is straight-forward to show that the fields above the grating are expressed as:

$${}_{back}E_y = -\frac{1}{2} q \left(\frac{\mu_0}{\varepsilon_0}\right)^{1/2} \frac{\beta'}{k_0} \frac{\alpha_0'}{\gamma_0'} \cdot exp\left(i\alpha_0' x - i\gamma_0' (z - z_0)\right)$$

$$-\frac{q}{2\gamma_0'} \left(-\mu_0 \omega + \frac{(\beta')^2}{\omega \varepsilon_0}\right) \tan\Psi_1 exp\left(i\alpha_0' x - i\gamma_0' (z - z_0)\right) + \sum_{m=-\infty}^{\infty} {}_{back}E^r_{y,m} exp\left(i\alpha_m' x + i\gamma_m' z\right) \quad when\ (0 < z < z_0) \qquad (1.47)$$

$${}_{back}H_y = -\frac{1}{2} q exp\left(i\alpha_0' x - i\gamma_0' (z - z_0)\right) + \sum_{m=-\infty}^{\infty} {}_{back}H^r_{y,m} exp\left(i\alpha_m' x + i\gamma_m' z\right) \quad when\ (0 < z < z_0) \qquad (1.48)$$

with $\alpha_0' = (-\omega - \beta' v_0 \sin\Psi_1) / (v_0 \cos\Psi_1)$ and $\gamma_0' = i\left[(\alpha_0')^2 + (\beta')^2 - k_0^2\right]^{1/2}$

and with $\alpha_m' = \alpha_0' + 2\pi m / D$ and $(\gamma_m')^2 = k_0^2 - (\beta')^2 - (\alpha_m')^2$ with $Re(\gamma_m') \geq 0$ and $Im(\gamma_m') \geq 0$.

For clarity, the following quantities are introduced:

$$K = \frac{1}{2} q \left(\frac{\mu_0}{\varepsilon_0}\right)^{1/2} \frac{\beta}{k_0} \alpha_0 + \frac{1}{2} q \left(-\mu_0 \omega + \frac{\beta^2}{\omega \varepsilon_0}\right) \tan\Psi_1$$
$$K' = -\frac{1}{2} q \left(\frac{\mu_0}{\varepsilon_0}\right)^{1/2} \frac{\beta'}{k_0} \alpha_0' - \frac{1}{2} q \left(-\mu_0 \omega + \frac{(\beta')^2}{\omega \varepsilon_0}\right) \tan\Psi_1 \qquad (1.49)$$

### 1.3.3 Power relations

The relation ( 1.44 ) is applied first to the couples $(E_y; \bar{E}_y)$ and $(H_y; \bar{H}_y)$ and then to the couples $({}_{back}E_y; {}_{back}\bar{E}_y)$ and $({}_{back}H_y; {}_{back}\bar{H}_y)$. Taking into account that when $\gamma_n$ is real, $\bar{\gamma}_n$ is equal to $\gamma_n$ and when $\gamma_n$ is imaginary, $\gamma_n$ is equal to $-\gamma_n$, the following relations are obtained for the first experiment:

$$\sum_{real\gamma_n} E^r_{y,n} \bar{E}^r_{y,n} \gamma_n = 2K \cdot Re\left(E^r_{y,0} exp\left(i\gamma_0 z_0\right)\right)$$
$$\sum_{real\gamma_n} H^r_{y,n} \bar{H}^r_{y,n} \gamma_n = -q \cdot Re\left(H^r_{y,0} \gamma_0 exp\left(i\gamma_0 z_0\right)\right) \qquad (1.50)$$

In the second case, one obtains:

$$\sum_{\text{real}\gamma_m} {}_{back}E^r_{y,m} \cdot {}_{back}\bar{E}^r_{y,m}\gamma_m{}' = 2K' \cdot Re\left({}_{back}E^r_{y,0} exp\left(i\gamma_0{}' z_0\right)\right)$$
$$\sum_{\text{real}\gamma_m} {}_{back}H^r_{y,m} \cdot {}_{back}\bar{H}^r_{y,m}\gamma_m{}' = q \cdot Re\left({}_{back}H^r_{y,0}\gamma_0{}' exp\left(i\gamma_0{}' z_0\right)\right) \qquad (1.51)$$

In the "classical" grating problem, a grating is illuminated by an incident plane wave, and one calculates the distribution of the diffracted waves and their intensities. A first test to check the validity of the obtained results is to apply the energy conservation theorem: the sum of the energies of the diffracted propagating waves has to be equal to the energy of the incident wave.

In the special case of the Smith-Purcell diffraction, such a theorem does not hold, because the waves emitted by the moving electron are evanescent. The relations given by equation ( 1.51 ) constitute the equivalent of the energy balance criterion [41] obtained when applying the conservation of energy in spectroscopy, and they can be used to test the validity of the results.

### 1.3.4 Reciprocity theorem for the zero order

Applying the lemma ( 1.44 ) to the couples $\left({}_{back}E_y(-\beta,\omega);E_y(\beta,\omega)\right)$ and $\left({}_{back}H_y(-\beta,\omega);H_y(\beta,\omega)\right)$ and noting that:

$$\int_{x_0}^{x_o+D} exp\left(i\frac{2\pi}{D}(n+m)x\right) = \delta_{n+m,0}$$
$$(\beta' = -\beta) \Rightarrow (\alpha_0{}' = -\alpha_0) \text{ and } (\gamma_0{}' = \gamma_0) \text{ and } (K' = -K) \qquad (1.52)$$
$$(-m = n) \Rightarrow (\alpha_{-m}{}' = -\alpha_n)$$
$$(-m = n) \Rightarrow (\gamma_{-m}{}' = \gamma_n)$$

the following relations are obtained:

$${}_{back}E^r_{y,0}(-\beta,\omega) = -E^r_{y,0}(\beta,\omega)$$
$${}_{back}H^r_{y,0}(-\beta,\omega) = -H^r_{y,0}(\beta,\omega) \qquad (1.53)$$

These relations constitute the equivalent of the reciprocity theorem applied to the zero order of diffraction in spectroscopy [41]. The main difference is that in our case the zero order is evanescent, while it is propagative when using the grating for spectroscopy.

### 1.3.5 Reciprocity theorem for the -1st order

An interesting consequence of the above property is obtained by considering a wavelength λ for which there is only one propagative diffracted order.

The combination of the relations ( 1.50 ), ( 1.51 ) and ( 1.53 ) gives the following relations:

$$\begin{aligned} E^r_{y,-1} \cdot \bar{E}^r_{y,-1}(\beta, \omega) &= {}_{back}E^r_{y,1} \cdot {}_{back}\bar{E}^r_{y,1}(-\beta, \omega) \\ H^r_{y,-1} \cdot \bar{H}^r_{y,-1}(\beta, \omega) &= {}_{back}H^r_{y,1} \cdot {}_{back}\bar{H}^r_{y,1}(-\beta, \omega) \end{aligned} \qquad (1.54)$$

which means that the amplitude of these waves are the same in the two experimental configurations described in Fig. 1.7. This result is well known in optics [41], but was never mentioned in the case of the Smith-Purcell radiation.

## 1.4 Relation between radiation loss and the Poynting vector

### 1.4.1 Mechanical work

In this section the radiation loss when the electron has traversed one period D of the grating will be calculated. The electron moves parallel to the surface of the grating at a constant speed, so that the radiation loss should be equal to the mechanical work W done to move the electron at constant speed against the action of the reflected field [29]. It is assumed that the radiation loss is negligible compared to the kinetic energy of the electron.

By definition of the mechanical work of a force $\boldsymbol{F}$:

$$W = -\int \boldsymbol{F} \cdot \boldsymbol{ds} \qquad (1.55)$$

with the Lorentz force:

$$\boldsymbol{F} = q \cdot (\boldsymbol{E}^r + \boldsymbol{v}_o \times \boldsymbol{H}^r) \qquad (1.56)$$

and since the work of the magnetic field is always zero one obtains the following expression, where the contributions of the x and the y components of the E-polarized reflected field are separated:

$$W = W_x + W_y \qquad (1.57)$$

with:

$$W_x = -\int_{t_1}^{t_1 + D/(v_o \cos\Psi_1)} q v_0 \cos\Psi_1 \cdot \mathrm{E}^r_x(v_0 t \cos\Psi_1, v_0 t \sin\Psi_1, z_0, t)\, dt \qquad (1.58)$$

and:

$$W_y = -\int_{t_1}^{t_1 + D/(v_o \cos\Psi_1)} q v_0 \sin\Psi_1 \cdot \mathrm{E}^r_y(v_0 t \cos\Psi_1, v_0 t \sin\Psi_1, z_0, t)\, dt \qquad (1.59)$$

The x component of the reflected field is given by:

$$E_x^r(x, y, z, t) = (2\pi)^{-1} Re\left(\int_0^{\infty} d\omega \int_{-\infty}^{\infty} E_x^r(x, z; \beta, \omega)\, exp\,(i\beta y - i\omega t)\, d\beta\right) \quad (1.60)$$

and the Rayleigh expansion gives the expression of the field in terms of the different diffracted orders:

$$E_x^r(x, z, \beta, \omega) = \sum_{n=-\infty}^{\infty} E_{x,n}^r(\beta, \omega) \cdot exp(i\alpha_n x + i\gamma_n z) \quad (1.61)$$

Taking into account ( 1.59 ), ( 1.60 ) and ( 1.61 ), and by interverting the summation and the integration, one obtains:

$$W_x = -\frac{q v_0 \cos\Psi_1}{2\pi^2} Re\left(\sum_{n=-\infty}^{\infty} \int_{t_1}^{t_1 + \frac{D}{v_0 \cos\Psi_1}} exp\,(\frac{i2\pi n}{D} v_0 \cos\Psi_1 t)\, dt \int_0^{\infty} d\omega \int_{-\infty}^{\infty} E_{x,n}^r exp\,(i\gamma_n z_0)\, d\beta\right) \quad (1.62)$$

Only the n=0 term gives a non zero contribution to the integration, and the x component of the zero order is obtained from the Maxwell equations as:

$$E_{x,o}^r = (k_0^2 - \beta^2)^{-1} (-\beta\alpha_0 E_{y,0}^r + \omega\mu_0\gamma_0 H_{y,0}^r) \quad (1.63)$$

then:

$$W_x = -\frac{qD}{2\pi^2} Re\left(\int_0^{\infty} d\omega \int_{-\infty}^{\infty} (k_0^2 - \beta^2)^{-1} (-\beta\alpha_0 E_{y,0}^r + \omega\mu_0\gamma_0 H_{y,0}^r)\, exp\,(i\gamma_0 z_0)\, d\beta\right) \quad (1.64)$$

For $W_y$ the calculations are similar and one obtains:

$$W_y = -\frac{qD}{2\pi^2} \tan\Psi_1 Re(\int_0^{\infty} d\omega \int_{-\infty}^{\infty} E_{y,0}^r exp\,(i\gamma_0 z_0)\, d\beta) \quad (1.65)$$

For $\Psi_1 \to 0$ the work $W_x$ of Eq. ( 1.64 ) agrees with the expression obtained by Van den Berg [29] for the total work $W$.

## 1.4.2 Poynting vector and radiation factor

One now makes use of the power relations ( 1.50 ) which are inserted into the expressions ( 1.64 ) and ( 1.65 ) giving the mechanical work. After interverting summation and integration one obtains:

$$W_x = \frac{qD}{2\pi^2} \int_0^{\infty} d\omega \int_{-\infty}^{\infty} (k_0^2 - \beta^2)^{-1} \cdot \left( \frac{\beta \alpha_0}{2K} \sum_{\text{real}\gamma_n} E^r_{y,n} \bar{E}^r_{y,n} \gamma_n + \frac{\omega \mu_0}{q} \sum_{\text{real}\gamma_n} H^r_{y,n} \bar{H}^r_{y,n} \gamma_n \right) d\beta \qquad ( 1.66 )$$

and:

$$W_y = \frac{qD}{2\pi^2} \tan\Psi_1 \int_0^{\infty} d\omega \int_{-\infty}^{\infty} \left( \frac{1}{2K} \sum_{\text{real}\gamma_n} E^r_{y,n} \bar{E}^r_{y,n} \gamma_n \right) d\beta \qquad ( 1.67 )$$

After some simplification, the expression giving the total work is:

$$W = \frac{D}{2\pi^2} \int_0^{\infty} d\omega \int_{-\infty}^{\infty} (k_0^2 - \beta^2)^{-1} \cdot \sum_{\text{real}\gamma_n} (\varepsilon_0 E^r_{y,n} \bar{E}^r_{y,n} + \mu_0 H^r_{y,n} \bar{H}^r_{y,n}) \, \omega \gamma_n d\beta \qquad ( 1.68 )$$

The real part of the complex Poynting vector:

$$\boldsymbol{P}_n = \frac{1}{2} \boldsymbol{E}^r_n \times \bar{\boldsymbol{H}}^r_n \qquad ( 1.69 )$$

represents the power density (power per unit area) radiated in the spectral order n.

From the Maxwell equations, one obtains:

$$\frac{1}{2} \boldsymbol{E}^r_n \times \bar{\boldsymbol{H}}^r_n = \frac{1}{2} (k_0^2 - \beta^2)^{-1} \omega \, (\varepsilon_0 E^r_{y,n} \bar{E}^r_{y,n} + \mu_0 H^r_{y,n} \bar{H}^r_{y,n}) \, \boldsymbol{k}_n \qquad ( 1.70 )$$

in which $\boldsymbol{k}_n = (\alpha_n, \beta, \gamma_n)$ is the wave vector of the reflected radiating wave of spectral order n.

Comparing this expression with the expression giving the total work leads to:

$$W = \frac{D}{\pi^2} \int_0^{\infty} d\omega \int_{-\infty}^{\infty} \sum_{\text{real}\gamma_n} \left( \frac{1}{2} \boldsymbol{E}^r_n \times \bar{\boldsymbol{H}}^r_n \right) \cdot \boldsymbol{i}_z d\beta \qquad ( 1.71 )$$

A closed relation between the mechanical work and the Poynting vector of the emitted radiation is obtained.

Using the ($\eta_n$, $\zeta_n$) reference frame of Fig. 1.5, and recalling Eq. ( 1.39 ), Eq. ( 1.68 ) is rewritten in function of the angles of emergence. A new expression for the integrant of Eq. ( 1.68 ) is obtained after some tedious work:

$$\frac{2Dc_0\left(\varepsilon_0 E^r_{y,n}\bar{E}^r_{y,n}+\mu_0 H^r_{y,n}\bar{H}^r_{y,n}\right)\omega\gamma_n\cos^2\eta\cos\zeta\,d\eta\,d\zeta}{(k_0^2-\beta^2)\left(\dfrac{c_0-v_0\left(\sin\eta\cos\Psi_1+\cos\eta\sin\zeta\sin\Psi_1\right)}{v_0\cos\Psi_1}\right)^3} \qquad (1.72)$$

Recalling equations ( 1.38 ) and ( 1.39 ) the integrant is rewritten as:

$$\frac{2}{D\varepsilon_0}\cdot\frac{U^r_n\bar{U}^r_n\cos^2\eta\cos^2\zeta}{\left(\dfrac{c_0-v_0\left(\sin\eta\cos\Psi_1+\cos\eta\sin\zeta\sin\Psi_1\right)}{v_0\cos\Psi_1}\right)^3}\cos\eta\,d\eta\,d\zeta \qquad (1.73)$$

with:

$$U^r_n\bar{U}^r_n = \left\{(\varepsilon_0/\mu_0)\,E^r_{y,n}\bar{E}^r_{y,n}+H^r_{y,n}\bar{H}^r_{y,n}\right\}\left(1-\sin^2\zeta\cos^2\eta\right)^{-1} \qquad (1.74)$$

The $z_0$ dependence of the incident fields is introduced explicitly, which permits to define a new quantity which is independent from $z_0$:

$$R_n(\omega) = \frac{2}{q}\cdot exp\left\{-i\gamma_0 z_0\right\}U^r_n(\omega) \qquad (1.75)$$

so that:

$$R^r_n\bar{R}^r_n = \frac{4}{q^2}exp\left(2|\gamma_0|z_0\right)\cdot U^r_n\bar{U}^r_n \qquad (1.76)$$

This quantity $R^r_n\bar{R}^r_n$ will be referred to now as the “radiation factor” and plays a key role in the calculation of the Smith-Purcell radiation.

Taking into account the condition for a wave to be radiative, equation ( 1.68 ) is finally rewritten as:

$$W = \sum_{\text{real}\gamma_n} W_n \qquad (1.77)$$

with:

$$W_n = \frac{q^2}{D\varepsilon_0}\int_{-\pi/2}^{\pi/2}\int_{-\pi/2}^{\pi/2}\frac{\cos^2\eta\cos^2\zeta\left|R_n(\zeta,\eta)\right|^2 exp\left(-\dfrac{z_0}{h_{int,n}(\zeta,\eta)}\right)}{\left[\dfrac{c_0-v_0\left(\sin\eta\cos\Psi_1+\cos\eta\sin\zeta\sin\Psi_1\right)}{v_0\cos\Psi_1}\right]^3}\cos\eta\,d\eta\,d\zeta \qquad (1.78)$$

in which:

$$h_{int,\,n} = \frac{1}{2|\gamma_0|} \tag{1.79}$$

From Eqs. ( 1.20 ) and ( 1.37 ) one obtains:

$$h_{int,\,n}(\zeta,\eta) = \frac{\lambda_n}{4\pi\left[\left(\frac{c_o}{v_o} - \cos\eta\sin\zeta\right)^2 + \cos^2\Psi_1\left(2\frac{c_o}{v_o}\cos\eta\sin\zeta - 1\right)\right]^{1/2}} \tag{1.80}$$

This parameter can be considered as an effective interaction range, analogue to the "formation zone" found in other types of radiation e.g. transition radiation [11] or the Cerenkov effect [9]. If the electron passes within the interaction range above the grating, it effectively contributes to the $n^{th}$ order Smith-Purcell radiation in the $(\zeta,\eta)$ direction. If it passes far from the grating surface (i.e. several times the interaction range) the electron will not produce Smith-Purcell radiation with a significant intensity.

Recalling the definition of the Poynting vector, and taking into account equations ( 1.71 ), ( 1.77 ) and ( 1.80 ), we can introduce the energy emitted in direction $(\eta,\zeta)$ per period length D and per solid angle in the $n^{th}$ radiative order:

$$\left(\frac{dP}{d\Omega}\right)_n = \frac{q^2}{\varepsilon_0 D}\frac{\cos^2\eta\cos^2\zeta|R_n(\zeta,\eta)|^2 exp\left(-\frac{z_0}{h_{int,\,n}(\zeta,\eta)}\right)}{\left[\frac{c_0 - v_0(\sin\eta\cos\Psi_1 + \cos\eta\sin\zeta\sin\Psi_1)}{v_0\cos\Psi_1}\right]^3} \tag{1.81}$$

which can be rewritten as:

$$\left(\frac{dP}{d\Omega}\right)_n = \frac{q^2D^2}{\varepsilon_0|n|^3\lambda^3}\cos^2\eta\cos^2\zeta|R_n(\zeta,\eta)|^2 exp\left(-\frac{z_0}{h_{int,\,n}(\zeta,\eta)}\right) \tag{1.82}$$

### 1.4.3 Invariance theorem

The two complementary experiments considered in paragraph 1.3 are in fact obtained by turning the grating by 180° around the z axis. Taking into account the expressions of the fields in both cases, the definition of the radiation factor and the definition of the radiative energy, the reciprocity theorem for the zero order and the $-1^{st}$ order allows to establish the following invariance theorem:

The coefficients of the zero order of the Rayleigh expansion remain the same when the grating is rotated by 180° around the z axis:

$$\begin{aligned} {}_{180}E^r_{y,\,0}(\beta,\omega) &= E^r_{y,\,0}(\beta,\omega) \\ {}_{180back}H^r_{y,\,0}(\beta,\omega) &= H^r_{y,\,0}(\beta,\omega) \end{aligned} \tag{1.83}$$

As long as there is only one diffracted order the Smith-Purcell emission diagram remains the same when the grating is rotated by 180° around the z axis:

$$|R_{-1}|^2 = |_{180}R_{-1}|^2 \qquad (1.84)$$

and then:

$$\left(\frac{dP}{d\Omega}\right)_{-1} = {}_{180}\left(\frac{dP}{d\Omega}\right)_{-1} \qquad (1.85)$$

It is worthwhile to note that this last theorem holds even if the grating profile is not symmetrical with respect to the y axis.

## 1.5 Radiation by an electron beam

Up to now, only one electron was considered. In an experiment however, an electron beam will be used in order to obtain reasonable intensities. The term $exp\,(2|\gamma_0|z_0)$ in equation ( 1.76 ) has been introduced in order to compensate for the $z_0$ dependence of the reflected fields $E^r_{y,n}$ and $H^r_{y,n}$ induced by the $z_0$ dependence of $E^i_y$.

With this definition, the radiation factor does not depend on the distance of the electron trajectory to the grating surface and the power of SP radiation emitted by an electron beam in direction $(\eta,\zeta)$ per period and per solid angle in the $n^{th}$ radiative order is obtained integrating Eq. ( 1.81 ) analytically over y and $z_0$, i.e., over the beam profile.

From a theoretical point of view, the extension of the grating is infinite. In practice, the grating has a finite extension. It is assumed in the following that the length L of the grating is much larger than the period D (the number of grooves of the grating is large enough for the infinite length grating hypothesis to hold). Then one has simply to multiply the previous result by the number of grooves L/D to obtain the total power emitted by the electron beam.

### 1.5.1 Ribbon-like electron beam

Let us assume a ribbon like electron beam passing over a grating with period D and length L. The ribbon like electron beam is supposed to be of width b much smaller than the width B of the grating (no edges effect) and of height H with a constant current density $J_0$. It is passing over a grating of period D and length L at an altitude $h_0$. Figure 1.8 describes the experimental set up.

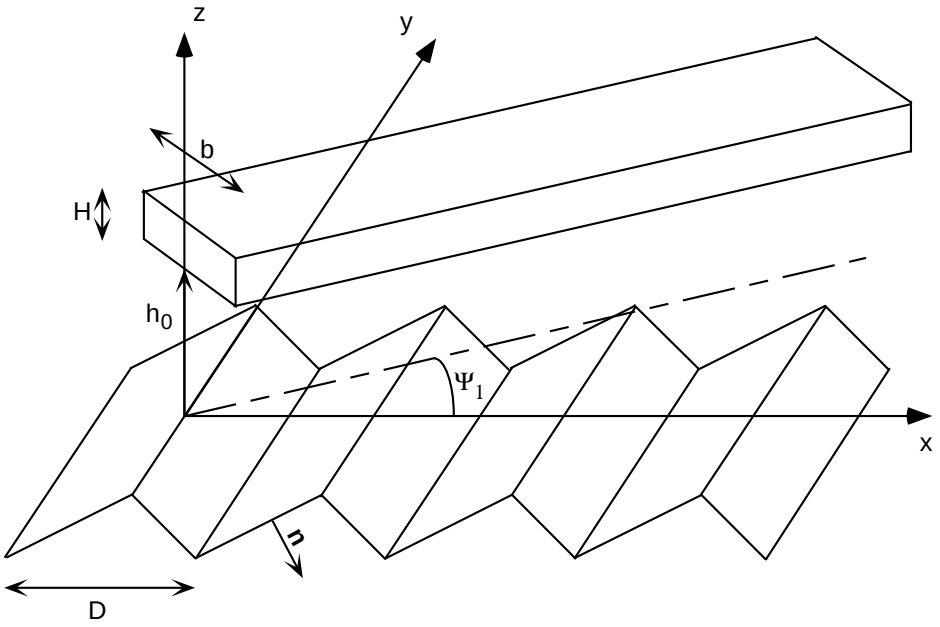


**FIGURE 1.8 : A ribbon like beam passing over a grating.**

Then, the power emitted in order n by the beam per unit solid angle into the direction $(\eta,\zeta)$ is given by:

$$\left(\frac{dP}{d\Omega}\right)_n = \frac{qLbJ_0}{D^2\varepsilon_0} \cdot \frac{\cos^2\eta\cos^2\zeta\,(h_{int,n}-h_0)\,\left(1-exp\left(-\frac{H}{h_{int,n}}\right)\right)}{\left[\frac{c_0 - v_0\,(\sin\eta\cos\Psi_1 + \cos\eta\sin\zeta\sin\Psi_1)}{v_0\cos\Psi_1}\right]^3} \cdot \left|R_n(\zeta,\eta)\right|^2 \qquad (1.86)$$

The first factor characterizes the experimental setup and includes the current density, the size of the electron beam, the size and period of the grating.

The second factor is a function of the electron energy and the angles of observation $(\eta_n,\zeta_n)$ for the spectral order n.

The last factor is the radiation factor and has to be calculated independently.

For $\Psi_1 = 0$, $z_0$=0 and b->∞, one obtains the expression given by Gover *et al.* [38]:

$$\frac{dP}{d\Omega} = \frac{eJ_0bL}{4\pi\varepsilon_0 D|n|} \cdot \frac{\cos^2\eta\cos^2\zeta}{(\beta^{-1}-\sin\eta)^2\,(\gamma^{-2}+\cos^2\eta\sin^2\zeta)^{0,5}} \cdot \left|R_n(\eta,\zeta)\right|^2 \qquad (1.87)$$

## 1.5.2 Gaussian electron beam

In reality, an electron beam often exhibits a Gaussian distribution of the current density. Fig. 1.9 describes the experimental set-up: a two-dimensional Gaussian distribution with widths $\sigma_y$ and $\sigma_z$ passes over a grating with period D with the beam axis at a distance $z_0$ above the grating which is shielded against electrons at z<0 (i.e. electrons passing at an altitude z<0 do not contribute).

Integrating Eq. ( 1.81 ) over the beam profile gives the power emitted in order n by the beam per unit solid angle in direction $(\eta,\zeta)$:

$$\frac{dP}{d\Omega} = \frac{ei_0LD}{\varepsilon_0|n|^3\lambda^3}\cdot\cos^2\eta\cos^2\zeta\cdot|R_{-1}|^2\cdot\frac{1}{2}erf\left(\frac{B}{\sqrt{8}\sigma_y}\right)exp\left(\frac{c^2}{4}-s_0\right)\left\{1-erf\left(\frac{c}{2}-\frac{s_0}{c}\right)\right\} \qquad (1.88)$$

$i_0 = J_0 2\pi\sigma_y\sigma_z$ is the total beam current.

For clarity, $c = \sqrt{2}\sigma_z/h_{int}$, $s_0 = z_0/h_{int}$ have been introduced

No angular divergence of the electron beam is considered in this approximation.

For $\Psi_1 = 0$, $\sigma_x$->∞ and $\sigma_y$->∞, the above expression converges to the expression given by Gover *et al.* [38]

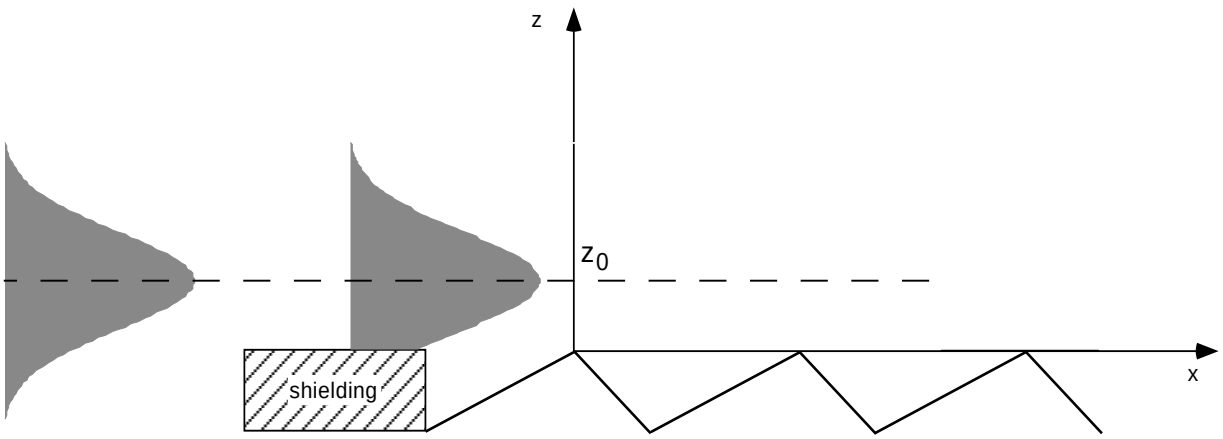


**FIGURE 1.9 : A Gaussian beam passing over a grating.**

## 1.6 Some remarks

### 1.6.1 Gratings with finite conductivity

When using relativistic electrons (c0/v0 ≈1) photons of very short wavelength are emitted in forward directions η->90˚. For example, using a commercial optical grating of 1800 lines per mm, at η=80˚ the corresponding wavelength is λ = 84 Å for $\Psi_1$=0°. At such short wavelengths, however, the hypothesis of a perfect conducting surface fails and one has to use a more complete theoretical model including the conductivity σ(λ). Some approximate models have been given [37], but to the author's knowledge, at present there is no available accurate theory of SP radiation including a finite conductivity σ(λ). The demonstration of section 1.3 using the Green's theorem is no longer valid, because the contribution of L does not vanish any more and one should adapt the Van den Berg approach taking into account the field inside the grating. Another method could also be used to calculate the contribution of the propagative field, as proposed by Bachheimer [20] using a direct calculation of the field based on the method of steepest descent.

In addition, the small ratio λ/D implies a very large number of propagative diffracted orders (131 in the previous case for ζ=0°). Under these circumstances, the solution of the grating problem can become difficult and an asymptotic theory for the diffraction of small wavelengths at large incident angles should be used. In a recent publication, Moran [27] presented a different approach based on the Ter-Mikaelian [42] description of radiation produced when a relativistic electron passes a linear slit. In this approach, the radiation is expressed in a closed form, which is very convenient for designing SP experiments. It assumes, however, infinitely thin screens, an assumption which may be questionable for photon wavelengths around 100 Å.

Some peculiar effects appear for not perfect conducting metallic surfaces diffracting electromagnetic waves [39]. Bachheimer [36] has shown that surface plasmons can in some cases greatly enhance the Smith-Purcell emission for the shortest wavelengths in the visible range. However, special formalisms have to be applied for the solution of the metallic grating problem.

Due to these limitations, the predictions presented in this work will be restricted to:

(i) wavelengths for which the conductivity of the surface can be considered as infinite, i.e. from millimeter wavelengths to infrared. For the visible range, the predictions will only be qualitative.

(ii) conditions for which the ratio λ/D is not too small, which means for relativistic electrons that the emission angles are not too close to the forward direction, typically η < 45˚ in most cases.

### 1.6.2 Non-parallel electrons

Up to now, only electrons moving parallel to the grating have been considered. The electromagnetic problem was then pseudoperiodic and the Floquet theorem (equivalent to the use of the Rayleigh expansion) holds.

In practice, one will always use electron beams and not single electrons in order to increase the Smith-Purcell emission. An electron beam has always a finite divergence, which means that electrons moving not parallel to the surface also contribute to the emitted radiation. The solution of the grating problem becomes in this case difficult, because of the non-periodicity of the incoming field. Moreover, electrons can hit the grating surface, due to their non parallel trajectories. An approximation for small angles of incidence was given by Bachheimer [20] who has shown that for low incidence angles, the obtained radiation was closely related to Smith-Purcell radiation.

In a first approach, assuming that the divergence of the electron beam is small, the incoming field is considered as pseudo-periodic and the solution of the grating problem obtained with the hypothesis of parallel electrons is considered to still hold. $\Theta<h_{int}/L$ is probably a good approximation and is easily satisfied if one considers the following example: E=5 MeV, D=1 mm, L=10 cm and $\lambda$=1 mm (observation at $\eta=\zeta=0°$) we obtain then $\Theta$<8.6 mrad. Considering an electron beam which interacts entirely with the grating (with a diameter $r=h_{int}$=0.86 mm in this case) one obtains an estimation of the maximum beam emittance $\varepsilon=r*\Theta$=7 mm mrad, which is quite large. In that case, even the positioning of the beam above the grating would not be too difficult. Then for long wavelengths, the finite beam emittance is not considered as a limiting factor when designing a Smith-Purcell experiment. The result is quite different if one considers emission in the visible or X-ray domain, for which the electrons have to pass extremely close to the grating in order to interact [27].

# CHAPTER 2 Solutions for the grating problem

Using the ideas of Toraldo di Francia [8] and Van den Berg [29], the electromagnetic field of a charged particle moving at constant speed has been calculated in the previous chapter, and the Smith-Purcell radiation has been expressed as a function of the diffracted field when this particle passes close to a periodic diffractive structure. Therefore, the calculation of the Smith-Purcell emission has been reduced to the so called “grating problem” (see paragraph 1.1.1). Several methods are now available to solve this problem and the choice of a particular method greatly depends on the grating profile. Some of the modern techniques will be described and their domain of usefulness will be given.

## 2.1 Description of the problem

The theoretical problem may be described in general terms as follows: an incident monochromatic plane electromagnetic wave impinges on a periodic diffractive structure resulting in a discrete set of reflected waves; the amplitude and the parameters $(k_0,\alpha_0,\beta,\gamma_0)$ characterizing the incoming wave are known as the parameters $(k_0,\alpha_n,\beta,\gamma_n)$ of the diffracted waves. The unknowns are the amplitudes of these waves. The reflection grating is assumed to be electrically perfectly conducting and is described by the equation $z = f(x)$. The Cartesian reference frame with the y-axis chosen parallel to the grating grooves and the x-axis chosen in the direction of the periodicity is used. The medium above the grating is assumed to be the vacuum.

The major difference between the “classical” grating problem in spectroscopy and the SP effect is the nature of the incoming plane wave, which in the latter case is evanescent. Therefore, it is not possible to define incident angles for the incoming plane wave as usually.

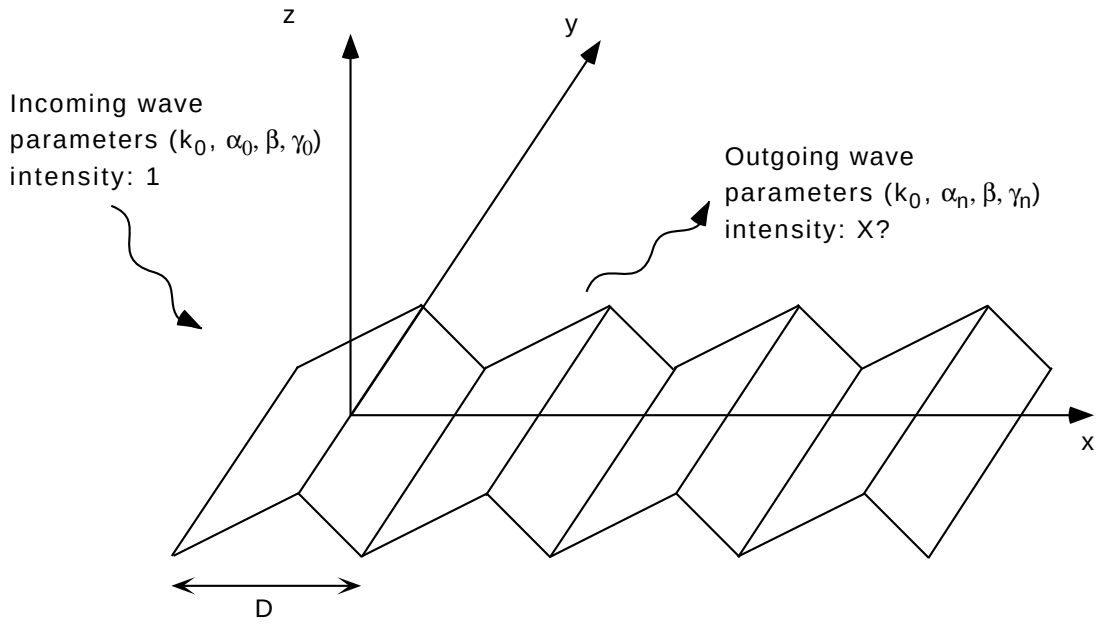


**FIGURE 2.1 : The grating problem scheme for SP radiation.**

As described in chapter 1, one assumes that a plane wave with wave vector $k_0$ and incoming parameters $\alpha_0$,$\beta$,$\gamma_0$ impinges on the diffraction grating. The incident field has the form:

$$E^i = exp\,(i\alpha_0 x - i\gamma_0 z)$$
$$H^i = exp\,(i\alpha_0 x - i\gamma_0 z) \qquad (2.1)$$

with:

$$\alpha_0 = \frac{\omega - \beta v_0 \sin\Psi_1}{v_0 \cos\Psi_1} \qquad (2.2)$$
$$\gamma_0 = i\,(\alpha_0^2 + \beta^2 - k_0^2)^{1/2} \text{ with } (\alpha_0^2 + \beta^2 - k_0^2)^{1/2} \geq 0$$

The constants in the expressions of the incident fields of the moving electron have been omitted here. The actual field is of course given by Eqs. ( 1.17 ) to ( 1.20 ) of chapter 1. But as the Maxwell equations are linear, the solutions which are going to be obtained have just to be multiplied by the proper factor to get back the solution of the physical problem.

The reflected field satisfies the source-free Maxwell equations:

$$(\nabla + i\beta \mathbf{i}_y) \times \boldsymbol{H}^r + i\omega\varepsilon_0 \boldsymbol{E}^r = 0$$
$$(\nabla + i\beta \mathbf{i}_y) \times \boldsymbol{E}^r - i\omega\mu_0 \boldsymbol{H}^r = 0 \qquad (2.3)$$

The total field satisfies the boundary condition:

$$n \times (\boldsymbol{E}^i + \boldsymbol{E}^r) = 0 \qquad (2.4)$$

Therefore, one has to consider the two cases of polarisation separately.

The diffracted field above the grating can be written using the Rayleigh expansions:

$$E_y^r(x, z;\beta, \omega) = \sum_{n=-\infty}^{\infty} E_{y,n}^r(\beta, \omega)\, exp(i\alpha_n x + i\gamma_n z)$$
$$\text{for } 0 < z < \infty \qquad (2.5)$$
$$H_y^r(x, z;\beta, \omega) = \sum_{n=-\infty}^{\infty} H_{y,n}^r(\beta, \omega)\, exp(i\alpha_n x + i\gamma_n z)$$

in which $\alpha_n = \alpha_0 + 2\pi n/D$ and $\gamma_n = (k_o^2 - \beta^2 - \alpha_n^2)^{1/2}$ with $Re(\gamma_n) \geq 0$ and $Im(\gamma_n) \geq 0$.

It is important to remember that the validity of the Rayleigh expansion has been established for z>0 only (i.e. over the grating), and up to now no information is available on the field in the grooves and one cannot calculate the Rayleigh coefficients. In the following paragraphs are described some of the modern methods to solve this problem, referred to as the "grating problem" in the literature. For the presentation, inspiration has been mostly taken from [29], [30], [31] and [39], adapting the different formalisms to the nature of the incoming wave (evanescent fields and conical diffraction).

## 2.2 The Rayleigh Assumption

The validity of the Rayleigh expansions has been proved outside the grooves, but there is no proof that it is also valid inside the grooves. If one assumes that it is (this constitute the so-called Rayleigh assumption because Rayleigh [40] was the first to use it) the determination of the amplitudes of the diffracted waves is simple. The pioneering works on Smith-Purcell radiation of Bachheimer [20] were made using this hypothesis and gave reasonable results.

In E-polarisation, assuming that on the grating surface the diffracted field is correctly described by the Rayleigh expansion and taking into account the boundary condition, the following infinite system of linear equations has to be solved for $z = f(x)$:

$$\sum_{n=-\infty}^{\infty} E_{y,n}^r exp(i\alpha_n x + i\gamma_n z) = -E_y^i(x, z) \qquad (2.6)$$

For the H-polarization case, the boundary condition leads to solve for $z = f(x)$:

$$\sum_{n=-\infty}^{\infty} \frac{(i\alpha_n f'(x) - i\gamma_n)}{(1 + f'(x)^2)^{1/2}} \cdot H_{y,n}^r exp(i\alpha_n x + i\gamma_n z) = -\frac{(i\alpha_0 f'(x) + i\gamma_0)}{(1 + f'(x)^2)^{1/2}} \cdot H_y^i(x, z) \qquad (2.7)$$

Both problems have in fact the same form:

$$\sum_{n=-\infty}^{\infty} F_n \phi_n(x) = F(x) \qquad (2.8)$$

One recognizes the expansion of a function with respect to a basis of functions. This problem has been intensively studied in the literature: in order to find the unknown coefficients $F_n$, one truncates the infinite series to $N$ and calculates an approximate value $F_n^N$. Then, $N$ is increased until convergence is achieved.

Two commonly used methods are presented. The first one was used by Lord Rayleigh himself to calculate the properties of gratings at the beginning of the century. The second one is a variant recently introduced.

### 2.2.1 Point Matching Method

The infinite series ( 2.8 ) is truncated, keeping only $2N+1$ terms and verified for $2N+1$ points of the surface. Then, a finite linear equations system is obtained:

$$\left[A_{p,n}\right] \cdot \left[F_n^N\right] = \left[B_p\right] \qquad (2.9)$$

with:

$$\begin{aligned} A_{p,n} &= \phi_n(x_p) \\ B_p &= F(x_p) \end{aligned} \qquad (2.10)$$

This method is called the Point Matching Method. It appears to be very simple. The major problem is the inversion of the matrix $A_{p,n}$.

### 2.2.2 Improved Point Matching Method

A variational method can also be used. It was first introduced by Meecham [45] and called the Improved Point Matching Method by Ikuno and Yasuura [46] who studied it intensively in order to solve the grating problem.

In this approach, the diffracted fields are approximated by truncated Rayleigh expansions, and the coefficients of these expansions are found by minimizing the following quantities $I_E$ and $I_H$ for the two fundamental cases of polarization:

$$I_E = \int_L \left| E_y^i + E_y^r \right|^2 ds \qquad (2.11)$$

$$I_H = \int_L \left| \mathbf{n} \cdot \nabla \left( H_y^i + H_y^r \right) \right|^2 ds \qquad (2.12)$$

The truncated Rayleigh expansions are given by:

$$E_y^r(x, z;\beta, \omega) = \sum_{n=-N}^{N} E_{y,n}^r(N;\beta, \omega)\, exp(i\alpha_n x + i\gamma_n z)$$
$$H_y^r(x, z;\beta, \omega) = \sum_{n=-N}^{N} H_{y,n}^r(N;\beta, \omega)\, exp(i\alpha_n x + i\gamma_n z) \qquad (2.13)$$

Minimizing $I_E$ and $I_H$, one obtains two systems of linear equations which can be expressed in the form of matrix equations $M_E \cdot E = V_E$ and $M_H \cdot H = V_H$.

For the E-polarization, the following elements of the matrix $M_E$ and the vector $V_E$ are obtained:

$$M_{Ep,n} = \int_L exp\{ i(n-p)\frac{2\pi}{D}x + i(\gamma_n - \gamma_p^*) f(x) \}\, ds$$
$$V_{Ep} = \int_L exp\{ i(-p)\frac{2\pi}{D}x + i(-\gamma_0 - \gamma_p^*) f(x) \}\, ds \qquad (2.14)$$

For the H-polarization, one obtains:

$$M_{Hp,n} = \int_L \frac{(i\alpha_n f'(x) - i\gamma_n)\,(i\alpha_p f'(x) - i\gamma_p)^*}{(1 + f'(x)^2)} exp\{ i(n-p)\frac{2\pi}{D}x + i(\gamma_n - \gamma_p^*) f(x) \}\, ds$$
$$V_{Hp} = \int_L \frac{(i\alpha_0 f'(x) + i\gamma_0)\,(i\alpha_p f'(x) - i\gamma_p)^*}{(1 + f'(x)^2)} exp\{ i(-p)\frac{2\pi}{D}x + i(-\gamma_0 - \gamma_p^*) f(x) \}\, ds \qquad (2.15)$$

The solution of the matrix problem involves the numerical computation of a large number of integrals which can be time consuming, depending on the grating profile. For some grating profiles however, the matrix coefficients can be obtained in closed form: when the grating profile consists of piecewise linear functions the coefficients are easy to calculate and the method seems particularly attractive for the triangular and rectangular gratings: one decomposes the integrals ( 2.14 ) and ( 2.15 ) into sub-integrals on each facet were f(x) is a linear function of x. Moreover, there is a direct link between the integrals giving the $M_H$ and $V_H$ matrices and the integrals giving the $M_E$ and $V_E$ matrices, which saves computing time.

### 2.2.3 The validity of the Rayleigh hypothesis

The Rayleigh assumption has been widely used by many authors but it turned out very soon that when using the Point Matching Method, the predictions were not correct for deep sinusoidal gratings nor for triangular gratings with large slope for the facets. The validity of the Rayleigh assumption was then seriously questioned and this problem gave rise to a number of theoretical works about it. It has been proved that for an arbitrary grating profile, it is not possible to say whether the Rayleigh assumption is valid or not [21].

The validity of the Rayleigh assumption is not related to the nature of the incoming wave (evanescent in the Smith-Purcell diffraction case, propagative in spectroscopy) but only to the grating profile. When using the Point Matching Method, this hypothesis is not valid for sinusoidal grating when h/D≥0.1426 [44]. For grating profiles which are not analytic (rectangular or triangular gratings) the Rayleigh assumption, combined with the Point Matching Method, is in general not correct: Millar proved that its validity is linked to the singularities of a conformal mapping. Therefore, it will not be used for this kind of gratings for which more reliable methods are preferable.

In contrast to the Point Matching Method, exact results can be obtained with the Improved Point Matching Method: it has been proved [46], [58] that both quantities $I_E$ and $I_H$ vanish for $N \to \infty$ and that the set of coefficients $E^r_{y,n}(N;\beta,\omega)$ and $H^r_{y,n}(N;\beta,\omega)$ converges to the Rayleigh coefficients: the method is rigorous for any grating profile.

## 2.3 The Integral Method

### 2.3.1 Description of the integral method

The first rigorous methods available for solving the diffraction problem for a perfectly conducting grating of arbitrary profile were the integral methods proposed at the beginning of the sixties by Petit and Cadilhac [47], Wirgin [48] and Uretsky [49] for the E-polarization case. For the H-polarization case the first rigorous approach was given in 1967 by Pavageau *et al.* [50].

Later, Van den Berg [29] was the first to propose a complete and correct theory of the Smith-Purcell effect using the Integral Method which he had developed to solve the grating problem [51]. In fact, Van den Berg proposed several integral equations of either the first or the second kind. From a numerical point of view, Fredholm integral equations of the second kind seem easier to be solved, because possible singularities in the kernels may lead to numerical problems in solution of integral equations of the first kind.

A complete demonstration of this method, involving the use of a two-dimensional form of the Green's theorem, can be found in [51] or in the book of Petit [39]. In this work only the main results will be explained.

The coefficients $E^r_{y,n}$ and $H^r_{y,n}$ are expressed as functions of the total field at the surface of the grating:

$$E^r_{y,n} = \frac{i}{2\gamma_n D} \cdot \int_L (\mathbf{n} \cdot \nabla E_y)\, exp\,(-i\alpha_n x - i\gamma_n z)\, ds \qquad (2.16)$$

$$H^r_{y,n} = -\frac{i}{2\gamma_n D} \cdot \int_L H_y\,(\mathbf{n} \cdot \nabla)\, exp\,(-i\alpha_n x - i\gamma_n z)\, ds \qquad (2.17)$$

in which the path of integration L is taken at the grating surface along one period and at constant y.

The quantities $\mathbf{n} \cdot \nabla E_y$ and $H_y$ are calculated from the integral equations of the second kind:

$$\frac{1}{2}\mathbf{n}_p \cdot \nabla_p E_y\,(x_p, z_p) + P\int_L (\mathbf{n} \cdot \nabla E_y)\ (-\mathbf{n}_p \cdot \nabla_p G)\, ds = \mathbf{n}_p \cdot \nabla_p E^i_y\,(x_p, z_p) \qquad (2.18)$$

$$\frac{1}{2}H_y\,(x_p, z_p) + P\int_L H_y\,(\mathbf{n} \cdot \nabla G)\, ds = H^i_y\,(x_p, z_p) \qquad (2.19)$$

where the point $(x_p,y_p)$ is on L and P denotes the Cauchy principal value of the integral.

G is a Green function given by:

$$G\,(x_p, z_p; x, z) = \sum_{n=-\infty}^{\infty} \frac{i}{2\gamma_n D} exp\,\{i\alpha_n\,(x_p - x) + i\gamma_n |z_p - z|\} \qquad (2.20)$$

There exists no general analytic solution of integral equations and therefore the solution has to be found numerically. The general technique consists in reducing the integral equation into a linear system of equations [39], [51]. Two methods have been commonly used: the Fourier series method and the Point Matching Method. The Fourier series method transforms the integral equation into a linear system of equations. It requires the computation of Fourier coefficients of the kernels, which are given by Fourier integrals. Therefore, it is of practical use only when these integrals are analytically calculable, which is the case for piece-wise linear grating profiles like the triangular or the trapezoidal profiles. Due to this restriction, in this work the more general Point Matching Method is used, which also transforms the integral equation into a linear system, but has the advantage that with some precautions, it can be adapted to every grating profile.

### 2.3.2 Solution of the integral equations

The derivation of the integral equations following Van den Berg [51] makes no assumption about the grating profile. However, the solution is given only for cases where the grating profile is given by an analytic function z=f(x). This excludes a priori rectangular

gratings, or triangular gratings with one vertical facet. Simple techniques to overcome this difficulty will be given, which allow to adapt the Integral Method to almost any grating profile.

The integral equations corresponding to both cases of polarization have the same form as the integrals giving $E^r_{y,n}$ and $H^r_{y,n}$:

$$\frac{1}{2}X(x_p, z_p) + \int_0^D K(x_p, z_p; x, z)\, X(x, z)\, dx = Y(x_p, z_p)$$
$$R_n = \int_0^D B_n(x, z)\, X(x, z)\, dx \qquad (2.21)$$

using in the E-polarization case:

$$X(x, z) = exp(-i\alpha_0 x)\ (n \cdot \nabla E_y)$$
$$Y(x, z) = exp(-i\alpha_0 x)\ (n \cdot \nabla E^i_y)$$
$$K(x_p, z_p; x, z) = \sqrt{1 + f'(x)^2}\, exp(i\alpha_0 (x_p - x))\ (-\mathbf{n}_p \cdot \nabla_p G) \qquad (2.22)$$
$$B_n(x, z) = \sqrt{1 + f'(x)^2}\, (i/2\gamma_n D)\, exp(i\alpha_0 x - i\alpha_n x - i\gamma_n x)$$
$$R_n = E^r_{y,n}$$

and in the H-polarization case:

$$X(x, z) = exp(-i\alpha_0 x)\ (H_y)$$
$$Y(x, z) = exp(-i\alpha_0 x)\ (H^i_y)$$
$$K(x_p, z_p; x, z) = \sqrt{1 + f'(x)^2}\, exp(i\alpha_0 (x_p - x))\ (-\mathbf{n} \cdot \nabla G) \qquad (2.23)$$
$$B_n(x, z) = -\sqrt{1 + f'(x)^2}\, (i/2\gamma_n D)\, exp(i\alpha_0 x)\ (\mathbf{n} \cdot \nabla)\, exp(-i\alpha_n x - i\gamma_n x)$$
$$R_n = H^r_{y,n}$$

The unknown function $X(x, z)$ is approximated by a combination of M values $X_m = X(x_m, z_m)$ $m = 1, \ldots, M$ at M points $x_m$ of the interval [0 $D$[

$$X(x, z) \approx S(x, z) = \sum_{m=1}^{M} P_m(x, z)\, X_m(x_m, z_m) \qquad (2.24)$$

The approximate integral equation becomes:

$$\frac{1}{2}X(x_p, z_p) + \sum_{m=1}^{M} \left( \int_0^D K(x, z; x_p, z_p)\, P_m(x, z)\, dx \right) X_m \approx Y(x_p, z_p) \qquad (2.25)$$

One writes this equation for each point $(x_p, z_p) = (x_j, z_j)$ $j = 1, \ldots, k$ and obtains the following system of linear equations:

$$\sum_{m=1}^{M} (K_{j,m} + \frac{1}{2}\delta_{j,m})\, X_m = Y_j \qquad j = 1, \ldots, M \tag{2.26}$$

with:

$$K_{j,m} = \int_0^D K(x, z; x_j, z_j)\, P_m(x, z)\, dx$$
$$Y_j = Y(x_j, z_j) \tag{2.27}$$

In the same way, the integrals giving the Rayleigh coefficients are calculated as:

$$R_n = \sum_{k=1}^{K} B_{n,k} X_k \tag{2.28}$$

with:

$$B_{n,m} = \int_0^D P_m(x, z)\, B_n(x, z)\, dx \tag{2.29}$$

The crucial point consists in the choice of the approximating function $S(x, z)$ i.e. the choice of the functions $P_k(x, z)$. Van den Berg [51] proposed to use periodic splines and to carry out the numerical integrations with a 4-point Gauss-Legendre quadrature which is accurate enough when the kernel of the integral equation is smooth.Since the grating profile is periodic, and due to the terms $exp(i\gamma_n|z - f(x)|)$ in the expression of the kernel, it has been proven [39] that the best quadrature is the rectangular rule with equidistant points.

In this case, the matrix coefficients are simply given by:

$$K_{j,k} = K(x_j, z_j; x_k, z_k) \cdot D/K \tag{2.30}$$

As soon as the $X_m$ values of the field are known on the $M$ points on the grating surface, the Rayleigh coefficients are calculated from ( 2.29 ) with:

$$B_{n,m} = B_n(x_m, z_m) \cdot D/M \tag{2.31}$$

Some problems remain however in order to calculate the $M^2$ elements of the matrix system. First the kernel $K$ of the integral equations are given by slowly converging series especially when $x_p \to x$.

Several methods have been proposed to calculate efficiently this series. Among these, a simple method consists in evaluating the remainder of the series giving the kernel [51]. This series has the form:

$$K(x_p, z_p; x, z) = \sum_{n=-\infty}^{\infty} \{ (\alpha_n / \gamma_n) A + B \} \exp(i\alpha_n C + i\gamma_n |D|) \qquad (2.32)$$

with $A$, $B$, $C$ and $D$ being function of $x_p$, $z_p$, $x$, $z$.

This series is truncated in the form:

$$K(x_p, z_p; x, z) = \sum_{n=-N+1}^{N-1} \{ (\alpha_n / \gamma_n) A + B \} \exp(i\alpha_n C + i\gamma_n |D|) + K_+ + K_- \qquad (2.33)$$

with the remainders:

$$\begin{aligned} K_+ &= \sum_{n=N}^{\infty} \{ (\alpha_n / \gamma_n) A + B \} \exp(i\alpha_n C + i\gamma_n |D|) \\ K_- &= \sum_{n=-\infty}^{-N} \{ (\alpha_n / \gamma_n) A + B \} \exp(i\alpha_n C + i\gamma_n |D|) \end{aligned} \qquad (2.34)$$

The series ( 2.32 ) does not converge very fast, especially as $|D| \to 0$ and one cannot simply neglect $K_+$ and $K_-$ even for relatively large $N$.

However, for large $N$ one finds $\gamma_n \approx i\alpha_n$ when $n \geq N$ and $\gamma_n \approx -i\alpha_n$ when $n \leq -N$ and therefore:

$$\begin{aligned} K_+ &\approx \sum_{n=N}^{\infty} \{ -iA + B \} \exp(\alpha_n (iC - |D|)) \\ K_- &\approx \sum_{n=N}^{\infty} \{ iA + B \} \exp(\alpha_n (iC + |D|)) \end{aligned} \qquad (2.35)$$

Since $\alpha_n = \alpha_0 + 2\pi n / D$ the remainders $K_+$ and $K_-$ are given by converging geometric series which are calculated in closed form:

$$\begin{aligned} K_+ &\approx \frac{\{ -iA + B \} \exp(\alpha_N (iC - |D|))}{1 - \exp(2\pi / D (iC - |D|))} \\ K_- &\approx \frac{\{ iA + B \} \exp(\alpha_{-N} (iC + |D|))}{1 - \exp(-2\pi / D (iC + |D|))} \end{aligned} \qquad (2.36)$$

The order of truncation $N$ is increased until the results converge to a prescribed accuracy.

The second problem is that the presence of the term $|z_p - z| = |f(x_p) - f(x)|$ in the expression of the Green function ( 2.20 ) gives after derivation a term $\operatorname{sgn}(f(x_p) - f(x))$ in

the expression of the kernel of the integral equation ( 2.21 ), which would seem to indicate that the kernels are not continuous when $x = x_p$. A careful analysis [52] shows that they are continuous and that the limits when $x \to x_p$ are given by:

$$\lim_{x \to x_p} (-\mathbf{n}_p \cdot \nabla_p G) = \frac{1}{\sqrt{1 + f'(x_p)^2}} \left[ f'(x_p) \left[ \frac{1}{2D} \sum_{n=-\infty}^{\infty} \frac{\alpha_n}{\gamma_n} + \frac{i\alpha_0}{2\pi} \right] + \frac{f''(x_p)}{4\pi (1 + f'(x_p)^2)} \right]$$

$$\lim_{x \to x_p} (-\mathbf{n} \cdot \nabla G) = \frac{1}{\sqrt{1 + f'(x_p)^2}} \left[ f'(x_p) \left[ \frac{1}{2D} \sum_{n=-\infty}^{\infty} \frac{\alpha_n}{\gamma_n} + \frac{i\alpha_0}{2\pi} \right] - \frac{f''(x_p)}{4\pi (1 + f'(x_p)^2)} \right] \qquad ( 2.37 )$$

The presence of the term f''(x) clearly indicates that the grating profile must have no edge and the diffraction problem for blazed gratings can not be solved using this technique. A simple method which permits to overcome this difficulty is given in section 2.5.

## 2.4 The Modal Expansion Method

When the trajectory of the charged particle is perpendicular to the grating rulings the Smith-Purcell effect in the (x,z)-plane (i.e. for $\zeta$=0°) is reduced to the study of the H-polarization diffraction because $\zeta$=0 implies $\beta$=0, for which the E-polarized contribution of the incoming wave vanishes [29]. In this special case the formalism is very similar to the one applied in calculations of the Smith-Purcell radiation produced by a line charge extended in the y direction, and moving in the x direction, parallel to the grating [28]. Such a theory has been developed by Van den Berg [30] for gratings with rectangular profile (also called lamellar gratings) using the Deryugin treatment [31].

As soon as the parameters $\alpha_0$,$\beta$,$\gamma_0$ of the incoming wave are known, there is complete freedom to choose the method to solve the grating problem. The Deryugin method is also adaptable to the E-polarized component [31] of the field produced by a point charge. A complete description of the Smith-Purcell radiation produced by an electron passing over a grating with rectangular profile is presented in this section. As it is the generalisation of the Van den Berg [29] description, similar notations are adopted. Figure 2.2 shows the relevant parameters for the grating.

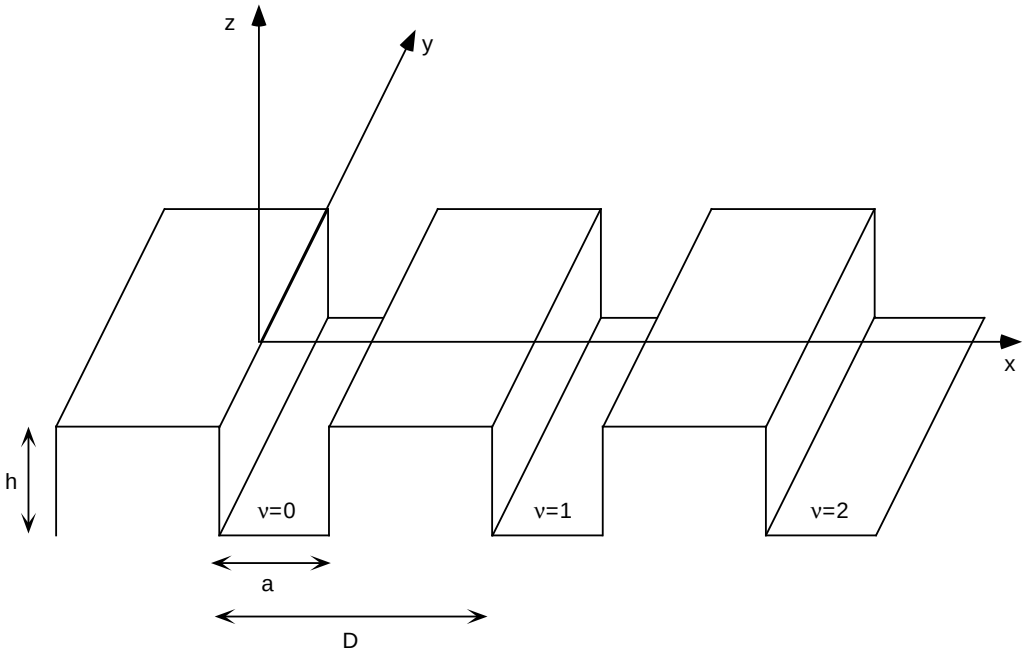


**FIGURE 2.2 : Profile of a rectangular grating.**

Above the grating, (i.e. in the half space z>0), the total fields are given by the sum of the incoming fields produced by the electron and of the refracted fields which can be written using the Rayleigh expansions:

$$E_y(x, z;\beta, \omega) = exp(i\alpha_0 x - i\gamma_0 z) + \sum_{n=-\infty}^{\infty} E^r_{y,n}(\beta, \omega)\, exp(i\alpha_n x + i\gamma_n z)$$
$$H_y(x, z;\beta, \omega) = exp(i\alpha_0 x - i\gamma_0 z) + \sum_{n=-\infty}^{\infty} H^r_{y,n}(\beta, \omega)\, exp(i\alpha_n x + i\gamma_n z) \qquad (2.38)$$

In order to obtain expressions for the fields inside the grooves (z<0), the boundary conditions on the walls of the grooves are used:

$$\begin{aligned} E_y(x, z;\beta, \omega) &= 0 \\ n \cdot \nabla H_y(x, z;\beta, \omega) &= 0 \end{aligned} \quad \text{for } x = 0, a \qquad (2.39)$$

From ( 2.39 ) it can be shown that the total electric field inside the groove can be written as a Fourier sine series [31] while the total magnetic field can be written as a Fourier cosine series [31]:

$$E_y(x, z;\beta, \omega) = \sum_{m=1}^{\infty} E_{y,m}(z;\beta, \omega) \sin\left(\frac{m\pi x}{a}\right)$$
$$H_y(x, z;\beta, \omega) = \sum_{m=0}^{\infty} H_{y,m}(z;\beta, \omega) \cos\left(\frac{m\pi x}{a}\right) \qquad (2.40)$$

These expressions are inserted into the Helmoltz equations for the source free fields:

$$\begin{aligned}(\partial_x^2 + \partial_z^2)\, E_y^r + (k_0^2 - \beta^2)\, E_y^r = 0 \\ (\partial_x^2 + \partial_z^2)\, H_y^r + (k_0^2 - \beta^2)\, H_y^r = 0\end{aligned} \qquad (2.41)$$

At the bottom of the groove, the boundary conditions are:

$$\begin{aligned}E_y(x, -h; \beta, \omega) &= 0 \\ n \cdot \nabla H_y(x, -h; \beta, \omega) &= 0\end{aligned} \quad \text{for } 0 \le x \le a \qquad (2.42)$$

From equations ( 2.40 ), ( 2.41 ), and ( 2.42 ), the following expressions for the fields inside the grooves are obtained:

$$\begin{aligned}E_y(x_\nu, z; \omega) &= exp(i\alpha_0 \nu D) \sum_{m=1}^{\infty} E_{y,m} \sin\left(\frac{m\pi x_\nu}{a}\right) \left[exp(-i\kappa_m z) - \Gamma_m exp(i\kappa_m z)\right] \\ H_y(x_\nu, z; \omega) &= exp(i\alpha_0 \nu D) \sum_{m=0}^{\infty} H_{y,m} \cos\left(\frac{m\pi x_\nu}{a}\right) \left[exp(-i\kappa_m z) + \Gamma_m exp(i\kappa_m z)\right]\end{aligned} \qquad (2.43)$$

with $0 \le x_\nu \le a$ and $-h \le z \le 0$, $\kappa_m = (k_0^2 - \beta^2 - (m\pi/a)^2)^{1/2}$ and $\Gamma_m = exp(2i\kappa_m h)$.

The modal expansions ( 2.44 ) which are valid inside the grooves are matched to the Rayleigh expansions valid above the grating using the continuity conditions at the open end of the grooves $0 \le x_\nu \le a$:

$$\begin{aligned}\lim_{z \to 0^+} E_y &= \lim_{z \to 0^-} E_y \\ \lim_{z \to 0^+} H_y &= \lim_{z \to 0^-} H_y\end{aligned} \qquad (2.44)$$

This gives a relation between the $E_{y,m}$ and $H_{y,m}$ of the Modal Expansion and the $E_{y,n}$ and $H_{y,n}$ of the Rayleigh expansion:

$$\begin{aligned}exp(i\alpha_0 x) + \sum_{n=-\infty}^{\infty} E_{y,n}^r(\beta, \omega)\, exp(i\alpha_n x) &= \sum_{m=1}^{\infty} E_{y,m} \sin\left(\frac{m\pi x_\nu}{a}\right) [1 - \Gamma_m] \\ exp(i\alpha_0 x) + \sum_{n=-\infty}^{\infty} H_{y,n}^r(\beta, \omega)\, exp(i\alpha_n x) &= \sum_{m=0}^{\infty} H_{y,m} \cos\left(\frac{m\pi x_\nu}{a}\right) [1 + \Gamma_m]\end{aligned} \qquad (2.45)$$

A second set continuity conditions for $0 \le x_\nu \le a$ is:

$$\begin{aligned}\lim_{z \to 0^+} \partial_z E_y &= \lim_{z \to 0^-} \partial_z E_y \\ \lim_{z \to 0^+} \partial_z H_y &= \lim_{z \to 0^-} \partial_z H_y\end{aligned} \qquad (2.46)$$

which gives:

$$(-i\gamma_0)\,exp\,(i\alpha_0 x) + \sum_{n=-\infty}^{\infty} E^r_{y,n}\,(\beta,\omega)\;(i\gamma_n)\,exp(i\alpha_n x) = \sum_{m=1}^{\infty} E_{y,m}\,(-i\kappa_m)\,\sin\,(\frac{m\pi x_\nu}{a})\;[1+\Gamma_m]$$
$$(-i\gamma_0)\,exp\,(i\alpha_0 x) + \sum_{n=-\infty}^{\infty} H^r_{y,n}\,(\beta,\omega)\;(i\gamma_n)\,exp(i\alpha_n x) = \sum_{m=0}^{\infty} H_{y,m}\,(-i\kappa_m)\,\cos\,(\frac{m\pi x_\nu}{a})\;[1-\Gamma_m] \qquad (2.47)$$

The boundary conditions on the ridges $a \le x_\nu \le D$ are:

$$\lim_{z\to 0^+} E_y = 0$$
$$\lim_{z\to 0^+} \partial_z H_y = 0 \qquad (2.48)$$

giving the equalities for $a \le x_\nu \le D$:

$$exp\,(i\alpha_0 x) + \sum_{n=-\infty}^{\infty} E^r_{y,n}\,(\beta,\omega)\,exp(i\alpha_n x) = 0$$
$$(-i\gamma_0)\,exp\,(i\alpha_0 x) + \sum_{n=-\infty}^{\infty} H^r_{y,n}\,(\beta,\omega)\;(i\gamma_n)\,exp(i\alpha_n x) = 0 \qquad (2.49)$$

Combining Eqs. ( 2.45 ), ( 2.47 ) and ( 2.49 ) with ( 2.38 ) allows to get rid of the coefficients $E_{y,m}$ and $H_{y,m}$ of the modal expansion and to obtain a linear system involving only the coefficients $E_{y,n}$ and $H_{y,n}$ of the Rayleigh expansion needed to calculate the intensity of the Smith-Purcell radiation.

In order to achieve this, one calculates first:

$$\left[\int_0^D exp\,(-i\alpha_k x)\,E_y\right]_{z=0}$$
$$\left[\int_0^D exp\,(-i\alpha_k x)\,\partial_z H_y\right]_{z=0} \qquad (2.50)$$

From the continuity relations ( 2.46 ) the equalities to be satisfied by the fields at the open end of the grooves are obtained:

$$\int_0^a \sin\,(\frac{p\pi x}{a})\,\lim_{z\to 0^+}\partial_z E_y = \int_0^a \sin\,(\frac{p\pi x}{a})\,\lim_{z\to 0^-}\partial_z E_y$$
$$\int_0^a \cos\,(\frac{p\pi x}{a})\,\lim_{z\to 0^+} H_y = \int_0^a \cos\,(\frac{p\pi x}{a})\,\lim_{z\to 0^-} H_y \qquad (2.51)$$

Recombining the relations obtained from ( 2.50 ) and ( 2.51 ), one extracts either systems involving only the Rayleigh coefficients or only the modal expansion coefficients, the latter one not being interesting for calculating Smith-Purcell radiation. The following linear systems is obtained for the electric field:

$$\sum_{n=-\infty}^{\infty} (D\delta_{k,n} - \gamma_n V_{k,n})\, E^r_{y,n} = C_k \quad k = 0, \mp 1, \mp 2, \ldots \tag{2.52}$$

in which:

$$C_k = \left[ D\delta_{k,0} + 2a\gamma_0 \sum_{m=1}^{\infty} \frac{\Gamma_m - 1}{\kappa_m (\Gamma_m + 1)} \Phi_{m,k} \Phi^*_{m,0} \right] \tag{2.53}$$

$$V_{k,n} = 2a \sum_{m=1}^{\infty} \gamma_m \frac{\Gamma_m - 1}{\kappa_m (\Gamma_m + 1)} (\Phi_{m,k} \Phi^*_{m,n}) \tag{2.54}$$

$$\Phi_{m,n} = a^{-1} \int_0^a \sin\left(\frac{m\pi x}{a}\right) exp\,(-i\alpha_n x)\, dx \tag{2.55}$$

In order to find the unknown Rayleigh coefficients, the infinite system of equation ( 2.52 ) and the infinite series ( 2.53 ), ( 2.54 ) are truncated. The orders of truncations are increased until convergence is obtained. The integrals giving $\Phi_{m,n}$ are calculated analytically.

For the magnetic field, the following system is obtained:

$$\sum_{n=-\infty}^{\infty} (\gamma_n D\delta_{k,n} - V_{k,n})\, H^r_{y,n} = C_k \quad k = 0, \mp 1, \mp 2, \ldots \tag{2.56}$$

in which:

$$C_k = \left[ \gamma_0 D\delta_{k,0} + a \sum_{m=0}^{\infty} \varepsilon_m \kappa_m \frac{\Gamma_m - 1}{\Gamma_m + 1} \Psi_{m,k} \Psi^*_{m,0} \right] \tag{2.57}$$

$$V_{k,n} = a \sum_{m=0}^{\infty} \varepsilon_m \kappa_m \frac{\Gamma_m - 1}{\Gamma_m + 1} \Psi_{m,k} \Psi^*_{m,n} \tag{2.58}$$

$$\Psi_{m,n} = a^{-1} \int_0^a \cos\left(\frac{m\pi x}{a}\right) exp\,(-i\alpha_n x)\, dx \tag{2.59}$$

$$\varepsilon_m = 2 - \delta_{m,0}$$

It is worthwhile to note that a simple relation exists between the $\Phi_{m,n}$ and the $\Psi_{m,n}$ which makes the computation of the $C_k$ and the $V_{k,n}$ coefficients very similar in both cases of polarization. This saves considerable computing time.

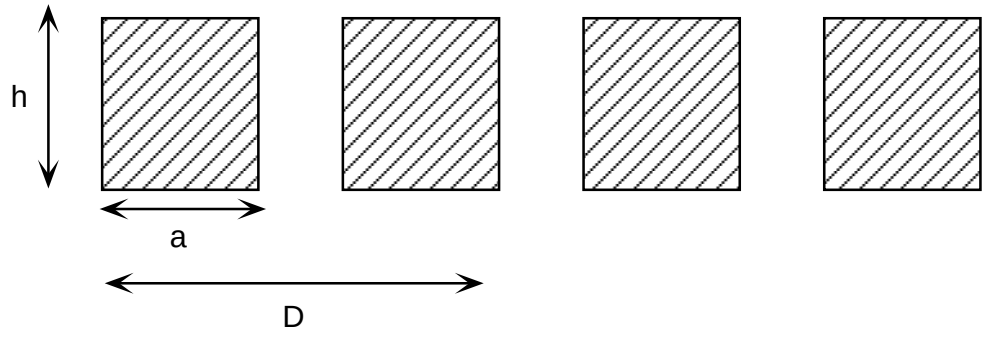


**FIGURE 2.3 : Scheme of a slab reflection-transmission grating.**

The modal expansion method is also useful to study the reflection and transmission grating described by Fig. 2.3. In this case, there exists also a transmitted field which in turn is given by a Rayleigh expansion.The field above the grating is given by the incident field plus a Rayleigh expansion and has to be matched with the field inside the grooves, which is given by a modal expansion, and the field under the grating which is also given by a Rayleigh expansion [53], [54].

## 2.5 Use of the Integral Method

As seen in paragraph 2.3, it is possible to study almost any type of gratings solving the integral equations with the aid of the Point Matching Method. Some problems appear however, when the grating surface has edges (see Eq. ( 2.37 )). A simple and efficient solution to overcome this difficulty consists in replacing the grating profile f(x) by an approximating profile $f_{app}(x)$, and testing the convergence of the results when the profile $f_{app}(x)$ tends to f(x). For triangular or trapezoidal gratings, one can use the grating profile $f_{app}(x)$ obtained with the summation of the N firsts coefficients of its Fourier series [39]:

$$f_{app}(x) = \sum_{n=0}^{N} c_n \cos\left(n\frac{2\pi x}{D}\right) + \sum_{n=1}^{N} s_n \sin\left(n\frac{2\pi x}{D}\right) \qquad (2.60)$$

This approximating profile has no edge, so that the integral method can be used without problem. The convergence of the results when N increases is a good check to test the validity of the results obtained with this method. The echelette gratings are easily treated with this method. One can for example use these properties to check that the results given by the IPPM method and the IE method applied to triangular gratings are identical.

When the function describing the grating profile is not analytic (rectangular grating or triangular grating with one vertical facet), the Fourier expansion however does not converge to the original profile for the singular points: this is the well known Gibbs effect. So one has to find other approximating profile.

A convenient way is to use nested sine functions of the form:

$f(X)=Y_n$ with $Y_n=SIN(\pi/2Y_{n-1})$ and $Y_0=SIN(2\pi X)$ for the rectangular grating

Fig. 2.4 illustrates the construction of the approximating profile for N=0,...,10. The curves are twice continuously differentiable. In the calculations, the number of iteration is increased until the obtained profile approaches the desired one. Then the integral method can be used to check the results given by other methods. The errors introduced by carrying out the calculations for rounded edges is probably not a serious restriction since in reality, the fabrication process of grating always results in some imperfections in the grating profile (see Fig. 2.5)

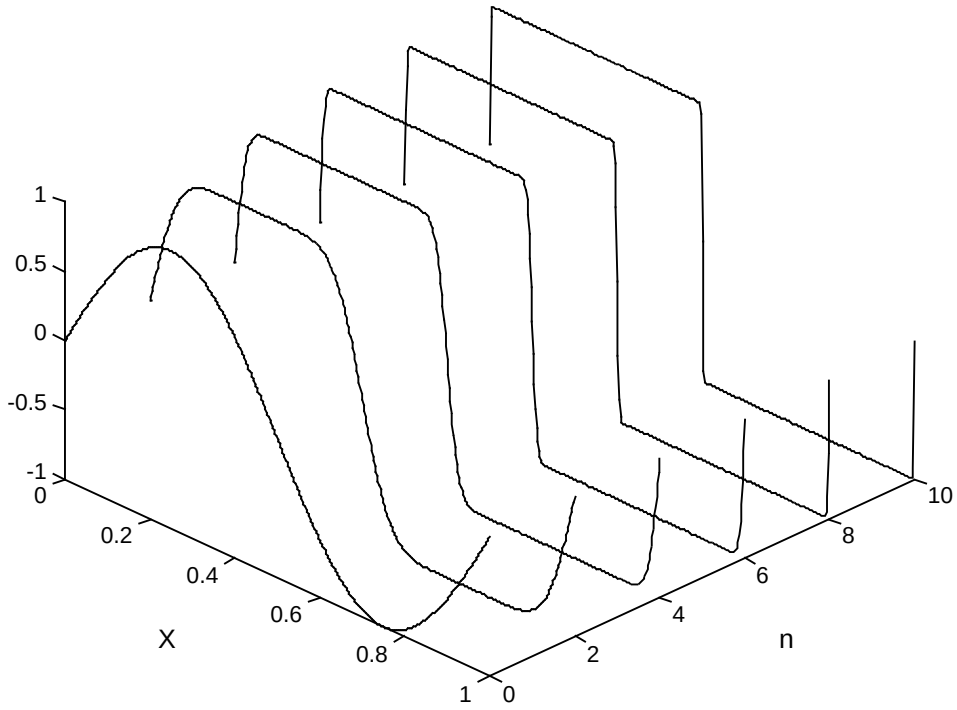


**FIGURE 2.4 : Nested sine functions giving a square profile.**

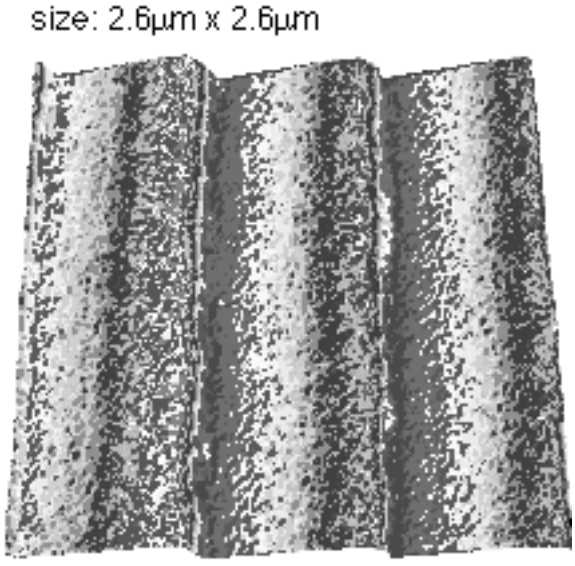


**FIGURE 2.5 : Picture of a short-period triangular grating with imperfections in the profile.**

## 2.6 Discussion

It is worth-while noting one particular difficulty, characteristic of the Smith-Purcell diffraction problem. The radiation factor can vary on a very large range of the order $10^{-3}....10^{2}$ and precise values of this factor are needed even if it is very small because this radiation factor is only one part of the expression giving the radiated power [29], [30], [32]. Reliable results are obtained when the convergence of the method has been achieved and when the power relations and the reciprocity theorem have been satisfied. In some cases, it is difficult to satisfy the power relations or the reciprocity theorem with a satisfactory accuracy. The convergence of the results when increasing the truncations or the number of points for the surface discretization becomes in this case a more useful criterion.

For symmetric grating profiles, the reciprocity theorem for the zero and first propagative orders is automatically satisfied and therefore not a criterion for the accuracy of the results. Only the power relations can be used to test the accuracy of the results when convergence has been achieved.

All methods described above lead to the solution of a system of linear equations, which often becomes a difficult numerical problem.The different programs have been written using MATLAB [55], a package for scientific and engineering numeric computation based on the LINPACK [56] and EISPACK [57] projects, which together represent the state of the art in software for matrix computation. The drawback of MATLAB is a rather low computational speed because it is an interpreted language. The results largely depend on how well the matrix to be inverted is conditioned. The condition number cond(X) of a matrix X measures the sensitivity of the solution of a linear system of equations due to uncertainties in the data and gives an indication of the accuracy of the results. The most common test is the 2-norm condition number which is the ratio of the largest singular value of the matrix to the smallest [55]. The larger the condition number is, the more reliable the results. Another MATLAB test is the estimate for the reciprocal of the condition of matrix X in 1-norm (largest column sum of X) rcond(X). When X is well conditioned, rcond(X) is close to 1. When X is badly conditioned, rcond(X) is close to 0.

For all methods (Rayleigh methods, MEM or Integral Method) it appears that the matrices are badly conditioned when one increases the different truncation orders. In some cases the matrices get extremely badly conditioned before the convergence has been achieved and no reliable results are obtained, e.g. the IPPM method for triangular gratings with large slopes or the Integral Method for comb-like gratings. More sophisticated treatments are necessary in these cases.

### 2.6.1 The Rayleigh method

As explained in paragraph 2.2, the Rayleigh method is not of general validity. For shallow sinusoidal gratings however the obtained results are correct when convergence has been achieved. Sinusoidal profile gratings are nowadays easily produced by photolithography even for short period gratings. One advantage of the Rayleigh method is that the inversion of the linear system of equations directly gives the radiation factor for all diffracted orders. Also

the coefficients of the matrix systems for the E and H polarizations are closely related, which saves computing time. Therefore, this method is well suited for shallow sinusoidal gratings.

### 2.6.2 The IPPM

In this approach the Rayleigh assumption is also used, but the variational method introduced to solve the boundary condition has been proved to be of general validity. An advantage is that this method gives also directly the radiation factor by inversion of the linear system for all diffracted orders. However, numerical problems appear for deep sinusoidal gratings, for which the convergence of the results becomes so slow that other methods become more appropriate, e.g. the Integral Method [58]. The same problem appears for triangular gratings, when one facette has a large slope, e.g. for echelette gratings [59].

Near Wood-Rayleigh anomalies, it also appears that convergence is difficult to achieve and the power relations are never well satisfied. The H-polarization case is the most difficult to be solved. The method has been improved by introducing smoothing procedures which accelerate the convergence [60][61]. Although the mathematical foundations of the method are rigorous, its implementation for arbitrary grating profiles is not simple.

### 2.6.3 The MEM

The MEM is a typical example of a specialized method applied to a particular grating profile. The method is valid only for rectangular gratings. This method has two advantages: the coefficients for the matrix systems for E and H polarizations are closely related and the solution of the matrix system gives the radiation factor for all the considered orders, which saves computing time. The method also takes care automatically of the edges of the grating profile, which require a special treatment when using more general methods like the Integral Method. Problems of convergence appear however for deep gratings ($h/D>0.5$) and for gratings with very small pitch ($a/D<0.1$) or very large pitch ($a/D>0.9$). The power relations can not be used to test the validity of the results because they are automatically satisfied. Only the convergence of the results when increasing the truncations is a reliable check of their validity. A variant has been introduced for symmetrical triangular gratings [62].

### 2.6.4 The Integral Method

As explained in paragraph 2.3, the Integral Method is of general validity and has been applied successfully for a large variety of profiles in calculating grating diffraction efficiencies. The coefficients of the matrix systems for both polarizations are also closely related. However, convergence can be slow in some cases. Also one integral has to be calculated for each diffracted order. There exist some grating profiles for which the method may not work, e.g. the comb-like grating. The Integral Method can be considered as the most general and the most reliable of the methods discussed in this work.

# CHAPTER 3 Calculations of Smith-Purcell radiation generated by electrons in the 1 MeV to 100 MeV energy range

In the previous chapters, a method to calculate the Smith-Purcell radiation emitted by an electron moving parallel to a grating has been given. It has been proved to lead to a grating problem, for which several solutions have been described. These techniques will now be applied to calculate Smith-Purcell radiation produced by electrons in the 1 MeV to 100 MeV energy range, an energy domain for which almost no calculations have been performed [32][63][64], and for which very few experiments have been carried out [65][66].

## 3.1 Some properties of the Smith-Purcell radiation pattern

The calculation of the emitted power requires the computation of the radiation factor, given by the solution of a grating problem. Knowing this radiation factor, one obtains the expression of the radiated power for one single electron, and integrating over the beam profile, the power emitted by the electron beam. For a ribbon-like electron beam of width b much smaller than the width B of the grating and of height $h >> h_{int}$ with a constant current density $J_0$ and passing over a grating of period D and length L, the expression of the power emitted in order n per unit solid angle is given by Eq. ( 1.87 ):

$$\frac{dP}{d\Omega} = \frac{eJ_0 bL}{(2)\,4\pi\varepsilon_0 D|n|} \cdot \frac{\cos^2\eta\cos^2\zeta}{(\beta^{-1}-\sin\eta)^2\,(\gamma^{-2}+\cos^2\eta\sin^2\zeta)^{0,5}} \cdot |R_n(\eta,\zeta)|^2$$

This expression is suitable to illustrate some peculiarities of the Smith-Purcell radiation pattern. The first factor characterizes the experimental setup, including the current density, the size of the electron beam, the size and period of the grating. The second factor, which will be

called G, is a function of the electron energy and the angles of observation (η,ζ) for the spectral order n. The third factor is the radiation factor.

Fig. 3.1 shows the η dependence of the factor G at 100 keV and 50 MeV. For high energies, G strongly increases in the forward direction η~90° where short wavelengths are emitted. A more detailed study shows that for relativistic electrons (β~1) and near η=0° a linear dependence with the energy is observed.

Fig. 3.2 shows the ζ dependence of G for the same energies. A strong effect of polarization seems to appear when the energy of the incoming electrons increases: The radiation is concentrated in the ζ=0° plane where the Smith-Purcell radiation is H polarized. This effect is more pronounced for observation angles near η=0°. Under favorable circumstances, the strong ζ dependence of G could be used to design a quasi monochromatic and polarized radiation source.

The intensity of the emitted Smith-Purcell radiation depends, of course, on the behaviour of the radiation factor, which itself strongly depends on the energy of the electron, on the grating profile and on the direction of observation (η,ζ). This radiation factor will be studied in the following sections.

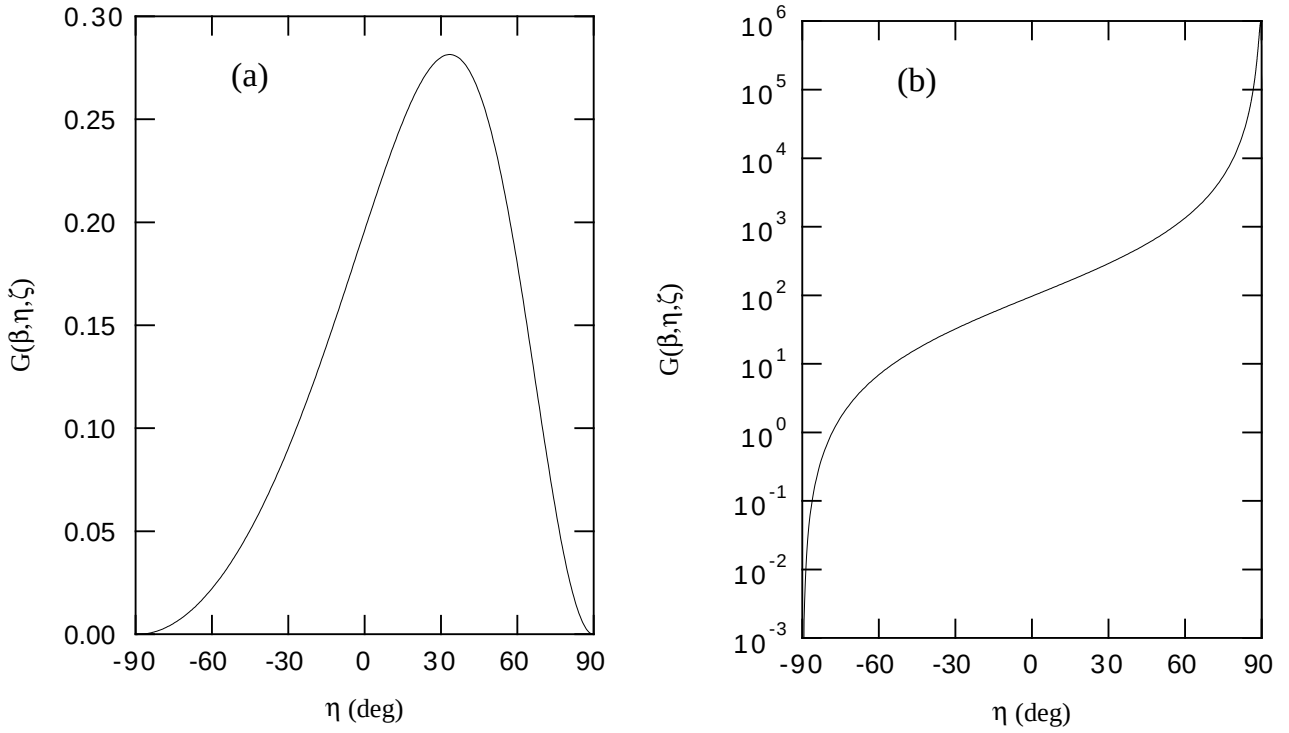


**FIGURE 3.1 : The η dependence of** G(β,η,ζ) **for** ζ=0° **and electron energies of (a) 100 keV and (b) 50 MeV.**

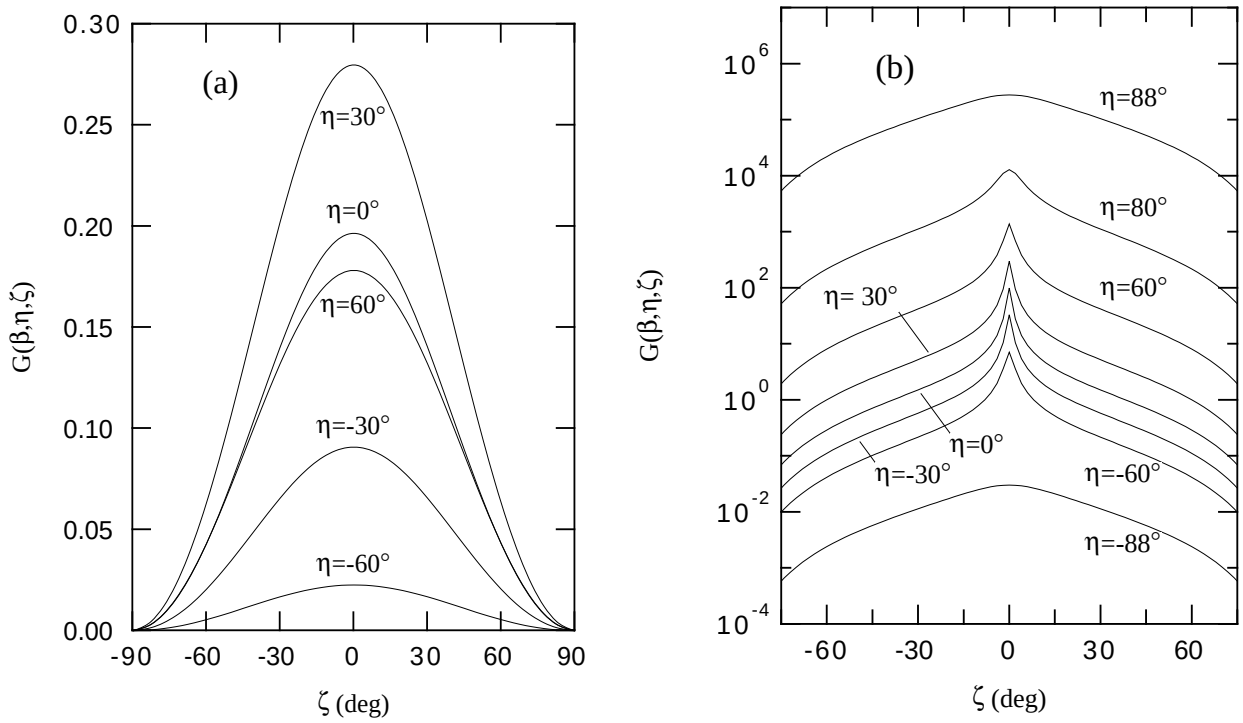


**FIGURE 3.2 : The ζ dependence of G(β,η,ζ) for several angles η and electron energies of (a) 100 keV and (b) 50 MeV.**

## 3.2 Summary of the methods

In the previous chapter, different methods to solve the grating problem in order to obtain the radiation factor have been presented. Some of these methods are restricted to special grating profiles, as for the MEM or the Rayleigh method, some others are of general validity, but their application can lead to long calculations or to numerical problems (IPPM, or IM when the grating profile has edges). Techniques which permit to overcome these problems in some cases have been detailed. It is not the goal of this work to test all the different possible methods and to find the advantages or disadvantages of them. Instead, the most simple and fastest method was chosen wherever its validity had been established. The following techniques have been used:

For shallow sinusoidal gratings (h/D<0.14), the Rayleigh method was used, with a point matching technique to solve the boundary condition.

For rectangular gratings, the Modal Expansion Method was used.

For deep sinusoidal gratings (h/D>0.14) and for triangular gratings, the Integral Equation Method was used.

A priori, these methods are rigorous. The numerical solution however requires truncation of infinite series, or discretization of continuous functions. Therefore the weak point of all these methods is the convergence of the solutions when the number of terms taken into account is increased. Then the different criteria discussed in paragraph 2.6 were used to check the validity of the obtained results.

## 3.3 Shallow gratings at $\zeta = 0°$ and $\Psi_1 = 0°$

The intensity of the emitted Smith-Purcell radiation is proportional to the radiation factor, which strongly depends on the grating profile and on the electron energy, as one can conclude from the previous theoretical works on the Smith-Purcell effect. The effect has been intensively studied both theoretically and experimentally for low-energy electrons in the order of some hundreds keV. However, no predictions have been made for relativistic electrons with energies larger than 1 MeV and only one experiment has been made in the far infrared range ($\lambda$~1 mm) with 2.3 MeV electrons. In all cases, the electrons were moving perpendicular to the grating rulings.

Figs.s 3.4-3.7 present some results of the calculations of the radiation factor $|R_{-1}(\eta_n, 0)|^2$ for relativistic electrons with energies in the 1 to 100 MeV range moving perpendicular to the grating rulings. All values have been calculated for the first propagative order n=-1 and for observation angles $\zeta$=0° for which the intensity is expected to be largest and are restricted to angles $\eta$<45° where a reliable convergence of the numerical solution of the grating problem has been obtained.

The results are given for shallow gratings with parameter h/D=0.1 for four types of gratings: the sinusoidal profile, the rectangular profile with parameter a/D=0.5, the symmetric triangular profile and the echelette profile for which we used respectively the Rayleigh method, the modal expansion method and the integral equations. The results were verified using the various tests described above.

In Fig. 3.4 the $\eta$ dependence of the radiation factor for a rectangular grating profile with parameters h/D=0.1, a/D=0.5 is given for several electron energies between 1 and 100 MeV. Strong variations of the radiation factor can be seen near certain values $\eta=\eta_w$ in the forward direction. These resonances are well known in spectroscopy and are named Wood-Rayleigh anomalies [16], [39]. They occur when an evanescent diffracted wave becomes propagative. The angles where these anomalies appear are given by the condition $\gamma_n = 0$ from which one obtains:

$$\sin\eta_w = \frac{(n+1)\,\beta^{-1}+1}{n} \qquad (3.1)$$

*n* being the order which becomes radiating (*n*<0). The calculations have been carried out on an angular mesh of 0.25° except near these anomalies, where the radiation factor has been calculated at angles $\eta_w \pm (10^{-7}, 10^{-4}, 10^{-3})$.

In most cases a strong decrease of the radiation factor is observed at angles near $\eta_w$, but in some cases a strong increase of the radiation factor is observed (see on Fig. 3.4 the sharp peak just before $\eta$=20° for an electron energy of 2 MeV). At these angles, the Smith-Purcell radiation is strongly collimated. The radiation factor decreases with increasing energy, the energy dependence being moderate for electron energies of 1 to 5 MeV but very strong at higher energies.

For the shallow sinusoidal grating with h/D=0.1, the calculations have been made using the Rayleigh method which is the fastest and verified for several angles using the integral method. Fig. 3.5 shows the obtained results. The radiation factor decreases strongly with increasing energy as for the rectangular grating with h/D=0.1 and a/D=0.5, but contrary to the results obtained for this rectangular grating, the $\eta$ dependence is rather smooth and fluctuations are restricted to a very narrow angular interval near a Wood-Rayleigh anomaly. Also for lower energies (1-10 MeV), the radiation factor is almost constant or even increases in the forward direction, in contrary to the rectangular grating, for which it tends to decrease in the forward direction.

For the symmetric triangular grating and the echelette grating, which is also often referred to as the blazed grating (see Fig. 3.3), the calculations were carried out using the Integral Method, approximating the profile by it's Fourier series; therefore, one expects accurate results when the local radius of curvature of the profile is small compared to the wavelength at the approximated edges. For the considered range of angles and energies and gratings, this is achieved when one takes approximately the 15 first coefficients of the Fourier series. The convergence of the results was verified by increasing the number of points for the surface discretization. For the blazed triangular profile, the results were also verified using the reciprocity theorem.

Figs.s 3.6 and 3.7 show the results obtained for a shallow symmetric triangular grating with h/D=0.1 and a blazed grating with blazing angle $\alpha_b$=10° respectively. For the symmetric triangular grating a lower radiation coefficient than for the shallow lamellar and sinusoidal gratings is observed, for electron energies of 1 to 5 MeV. For higher energies, the results are comparable. The Wood-Rayleigh anomalies are clearly visible, but no large peaks can be observed as for the lamellar grating. The behaviour of the radiation coefficient for the shallow blazed grating is very similar to that of the lamellar grating. The Wood-Rayleigh anomalies are very pronounced and strong resonances are visible at angles just before the angle where the anomalies occur.

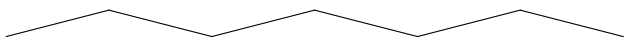

Profile of a symmetric triangular grating


Profile of a blazed triangular grating or echelette grating

**FIGURE 3.3 : Frofiles for symmetric and blazed triangular gratings.**

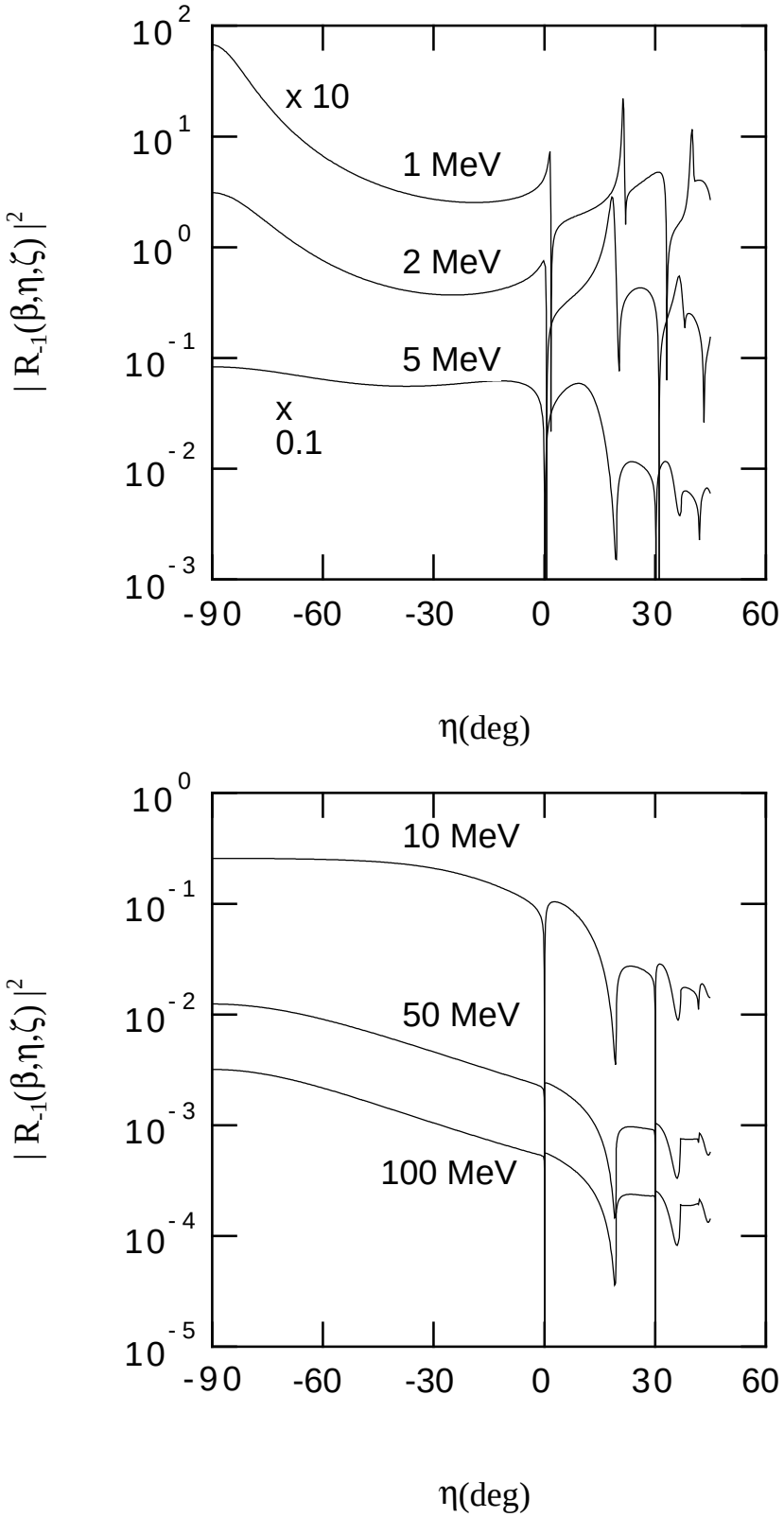


**FIGURE 3.4 :** **The radiation factor for a rectangular grating as a function of observation angle $\eta$ for $\zeta=0°$ and $\Psi_1=0°$ and for electron energies of 1, 2, 5, 10, 50 and 100 MeV. The grating parameters are h/D=0.1 and a/D=0.5. The data for 1 MeV and 5 MeV have been multiplied by factors of 10 and 0.1 respectively.**

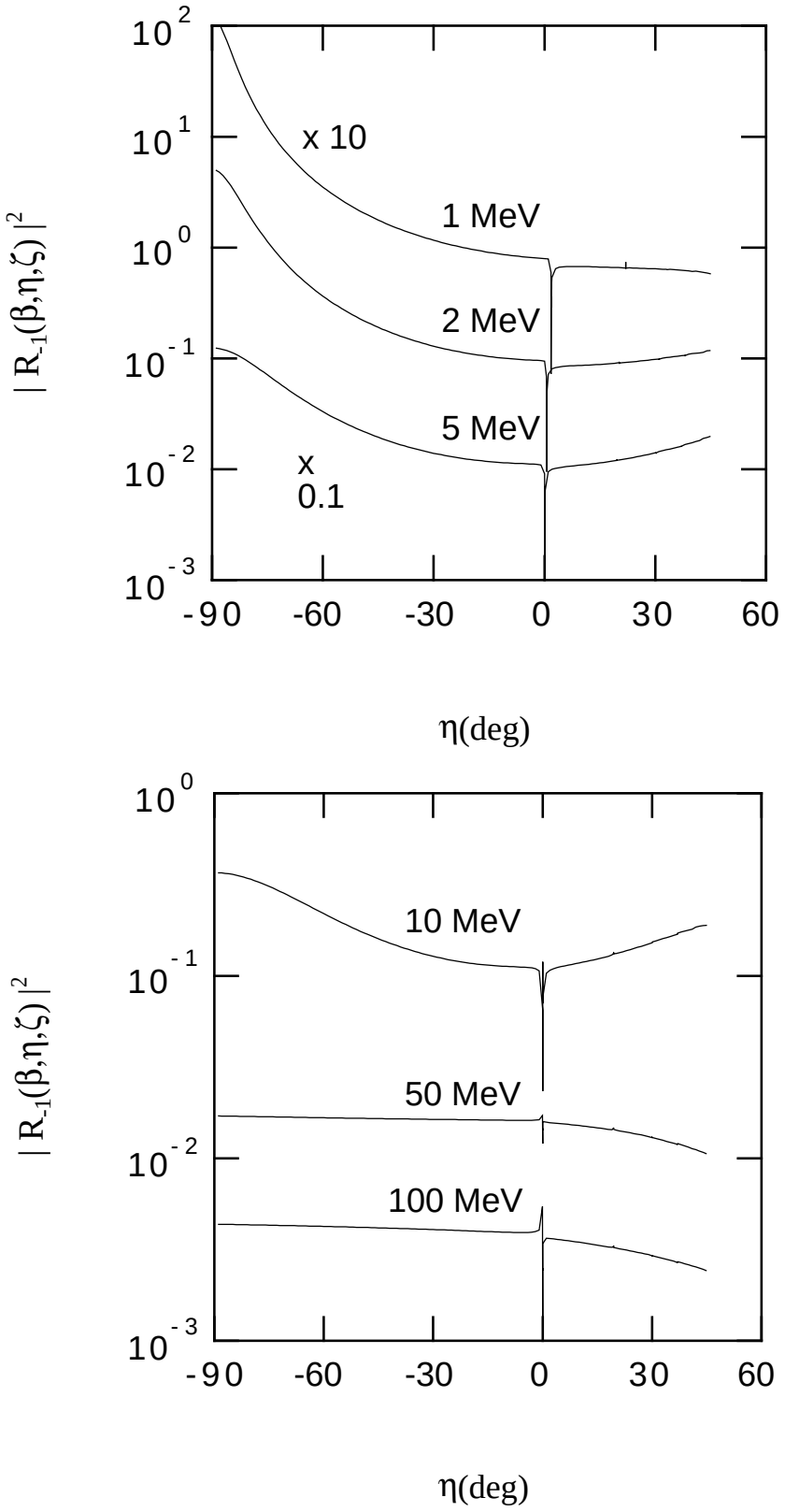


**FIGURE 3.5 : The radiation factor for a sinusoidal grating with h/D=0.1 as a function of observation angle η for ζ=0° and $\Psi_1$=0° and for electron energies of 1, 2, 5, 10, 50 and 100 MeV. The data for 1 MeV and 5 MeV have been multiplied by factors of 10 and 0.1 respectively.**

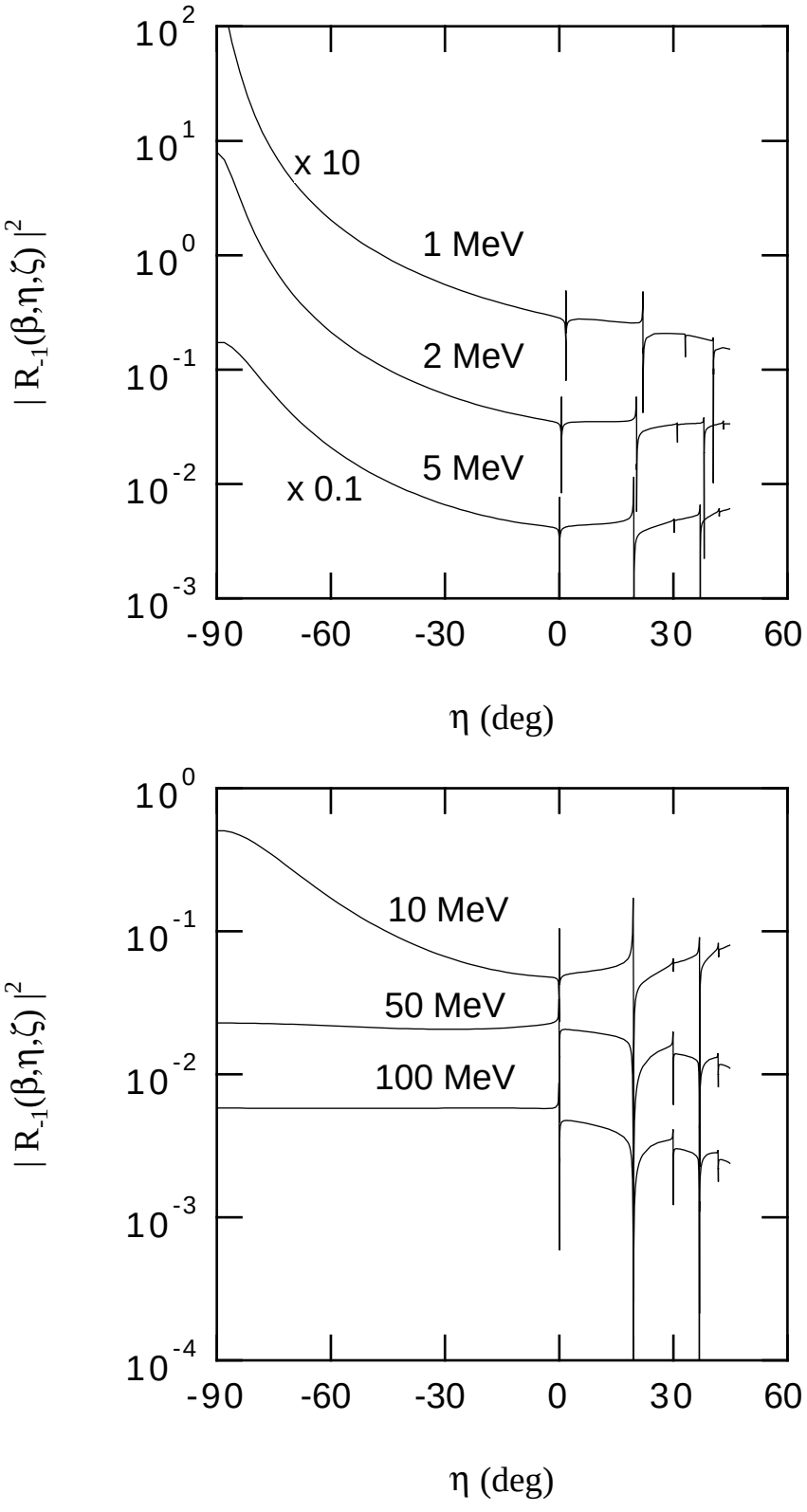


**FIGURE 3.6 : The radiation factor for a triangular symmetric grating as a function of observation angle $\eta$ for $\zeta=0°$ and $\Psi_1=0°$ and for electron energies of 1, 2, 5, 10, 50 and 100 MeV. The grating parameters is h/D=0.1. The data for 1 MeV and 5 MeV have been multiplied by factors of 10 and 0.1 respectively.**

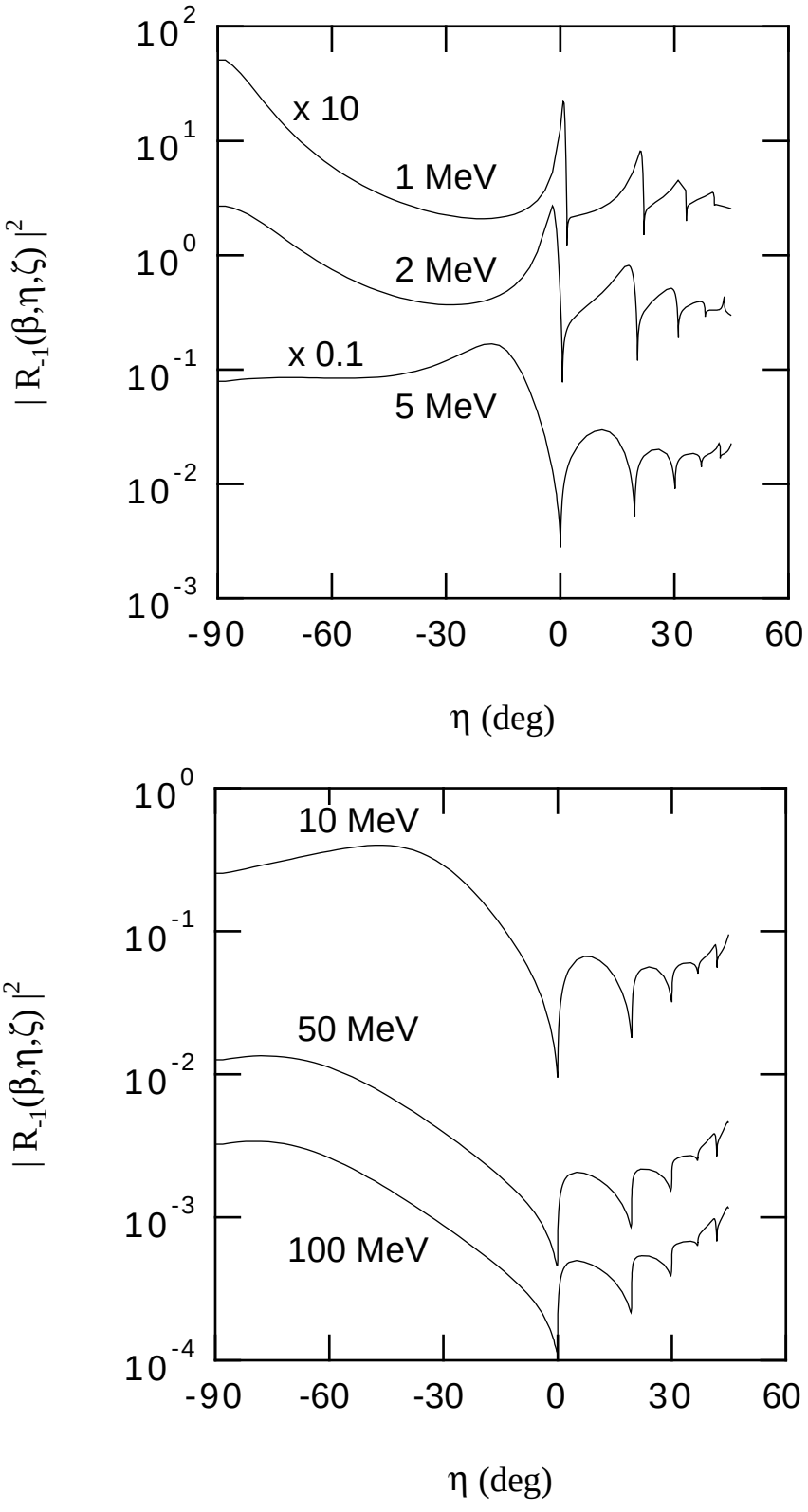


**FIGURE 3.7 : The radiation factor for an echelette grating as a function of observation angle η for ζ=0° and $\Psi_1$=0° and for electron energies of 1, 2, 5, 10, 50 and 100 MeV. The blazing angle of the grating is 10°. The data for 1 MeV and 5 MeV have been multiplied by factors of 10 and 0.1 respectively.**

For all the considered profiles a strong decrease of the radiation factor when increasing the electron energy above some 10 MeV was observed. A tentative explanation is formulated as follows: when increasing the electron energy, $v_0$ approaches $c_0$ and the factor $\gamma_0$ (characterizing the exponential decay of the incident field) becomes closer and closer to zero. The limiting case ($v_0$=$c_0$) would lead to $\gamma_0$=0; in that case, the incoming field would be propagative and as a consequence, the zero order would also be propagative. This can be interpreted from a mathematical point of view as the Wood-Rayleigh anomaly for the zero order. At the exact location of the Wood-Rayleigh anomaly, a strong decrease of the radiation factor is often observed. By analogy, coming closer to the Wood-Rayleigh anomaly corresponding to the zero order by increasing the electron energy could explain that the intensity of other radiative orders decreases. Therefore it seems not of great interest to use high energy electrons for radiation production using the Smith-Purcell effect in the considered angular range.

## 3.4 Influence of the grating depth at $\zeta = 0°$ and $\Psi_1 = 0°$

In the previous paragraphs shallow gratings with parameter h/D=0.1 have been considered. Deep gratings could lead to higher efficiencies. Figs. 3.10-3.11 show the results for the radiation factor $|R_{-1}(\eta_n, 0)|^2$ obtained as a function of the grating depth for two types of gratings: the sinusoidal grating and the rectangular grating with fixed parameter a/D=0.5 for electrons with energy in the 1-10 MeV range moving perpendicular to the grating rulings. The same angular mesh as in the previous chapter has been used. Fig. 3.8 shows the color map used in Figs. 3.10-3.11.

For rectangular gratings, a detailed study has been carried out for parameter a/D=0.5 and parameter h/D varying from 0.01 to 0.5 in steps of 0.01. Because the radiation factor is very large in the backward direction, the data have been cut off at maximum value of 4 for a better representation, and the color map of Fig. 3.8 has been used. For very shallow gratings (h/D->0) a strong decrease of the radiation factor is observed which corresponds to the fact that an electron moving parallel to a flat surface does not emit radiation. It is interesting to note that the best results are obtained for very shallow gratings with h/D~0.1. The use of deeper gratings seems to be of no advantage in this energy range. These results are quite different from the previous calculations for Smith-Purcell radiation produced by low energy electrons [30]. It is also worthwhile to note that small errors in the grating profile may constitute a severe restriction. In order to obtain high radiation emission for the rectangular grating with a/D=0.5 on a large angular range a value of h/D close to 0.1 is needed. In the forward direction deep gratings can be helpful to enhance the emission for 1-2 MeV electron.

Sinusoidal gratings with parameters h/D=0.01, 0.05, 0.1, 0.15, ....., 0.4 have been studied. In that case, the data are presented on a logarithmic scale. For such gratings rather smooth curves are obtained for all the considered energies and for radiation in the backward direction $\eta$<0. For deep sinusoidal gratings with h/D>0.30 strong variations are observed in the forward direction where shorter wavelengths are emitted. The best results are obtained for shallow and moderately deep gratings with h/D=0.1- 0.25. For deeper gratings the radiation factor decreases, especially in the forward direction. In some cases however, a strong increase is observed just before Wood-Rayleigh anomalies and at these angles the Smith-Purcell

radiation is strongly collimated as for the shallow rectangular grating studied previously. Except for deep gratings and in the forward direction, the variations of the radiation factor with the grating depth are rather smooth, which indicates that the Smith-Purcell emission would not be very sensitive to small errors in the profile.

The study of the influence of the grating depth for triangular gratings has not been carried out. However, a similar feature as for rectangular gratings has been observed for blazed gratings [67]: the Wood-Rayleigh anomalies are very pronounced and often a strong increase in the radiation factor was observed just before an anomaly. The best results have also been obtained for shallow gratings for the simulations using relativistic electrons up to 50 MeV.

Therefore, we conclude that, in general, shallow gratings appear to be more effective than deep gratings when using relativistic electrons moving perpendicular to the grating rulings and when the observations are done in the plane perpendicular to the grating. A full study of the grating performance in function of its characteristics and of the electron energy would be necessary to optimize a Smith-Purcell experiment and other types of grating could lead to different conclusions.

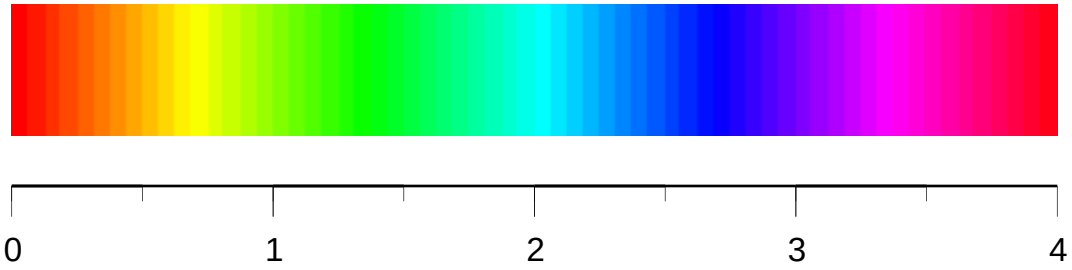


**FIGURE 3.8 : The color map used in Figs. 3.9-3.10.**

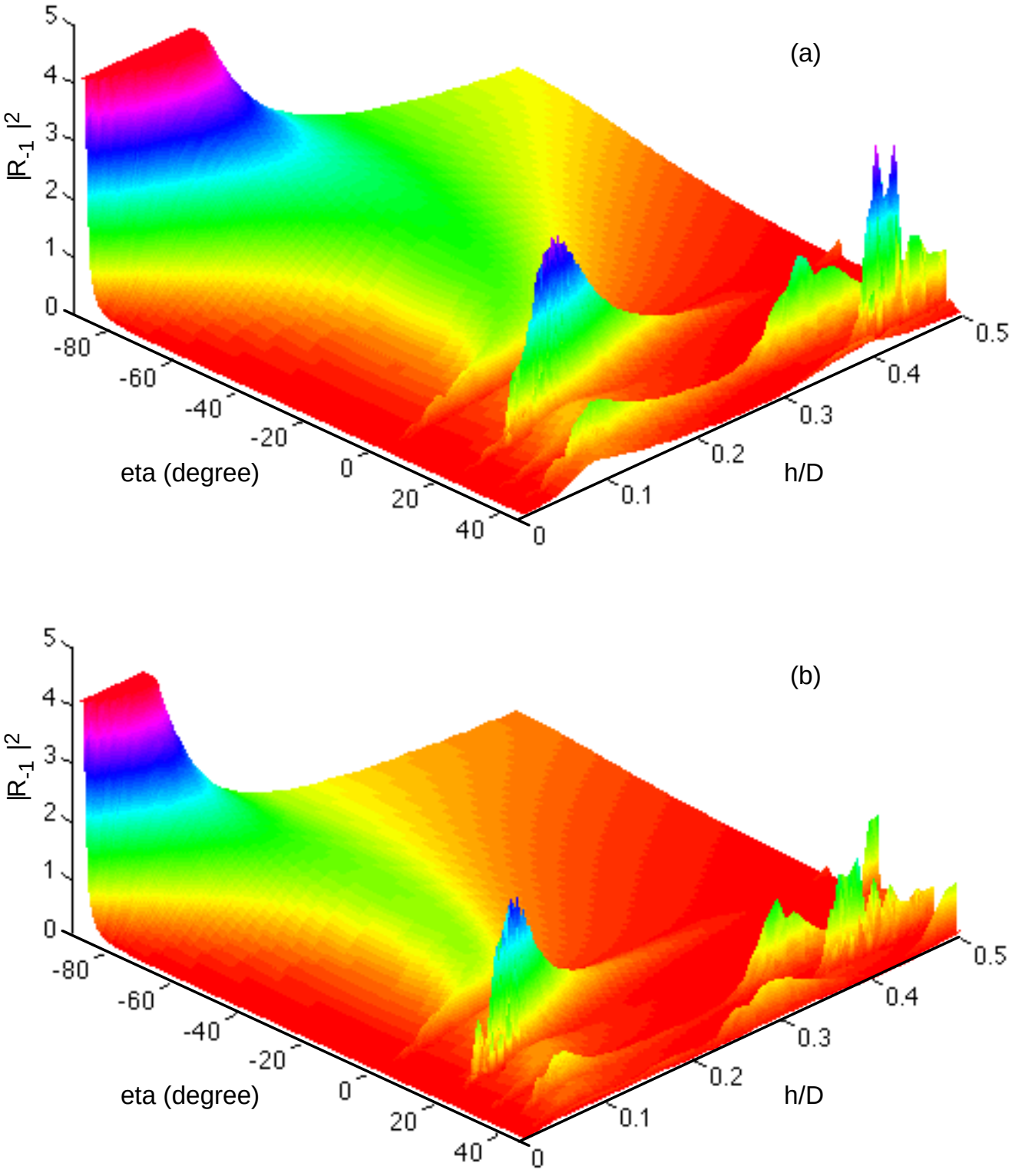


**FIGURE 3.9 :** **The radiation factor for a rectangular grating as a function of observation angle $\eta$ and grating depth for $\zeta$=0° and $\Psi_1$=0° and for electron energies of (a) 1 MeV and (b) 2 MeV.**

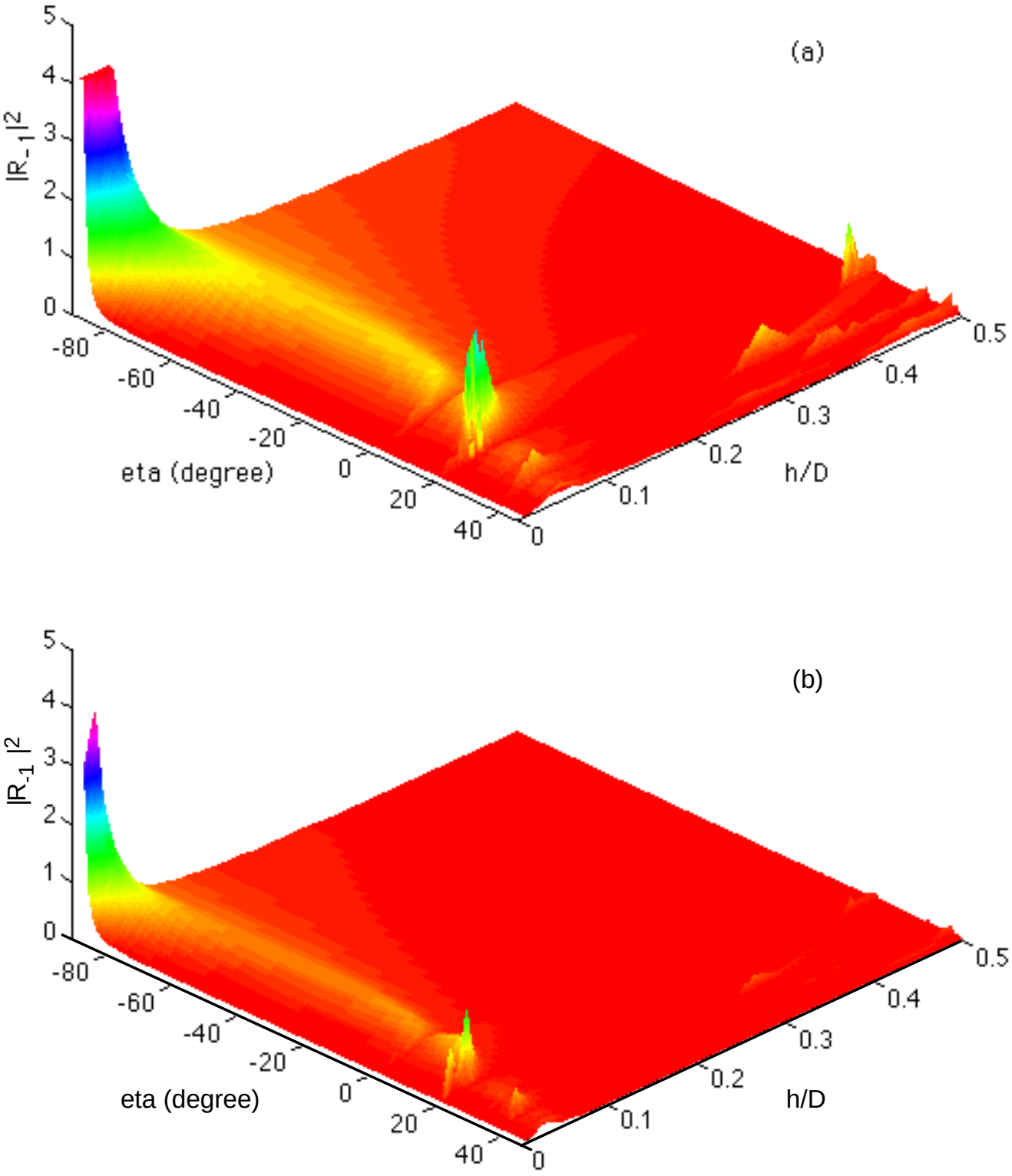


**FIGURE 3.10 : The radiation factor for a rectangular grating as a function of observation angle $\eta$ and grating depth for $\zeta=0°$ and $\Psi_1=0°$ and for electron energies of (a) 5 MeV and (b) 10 MeV.**

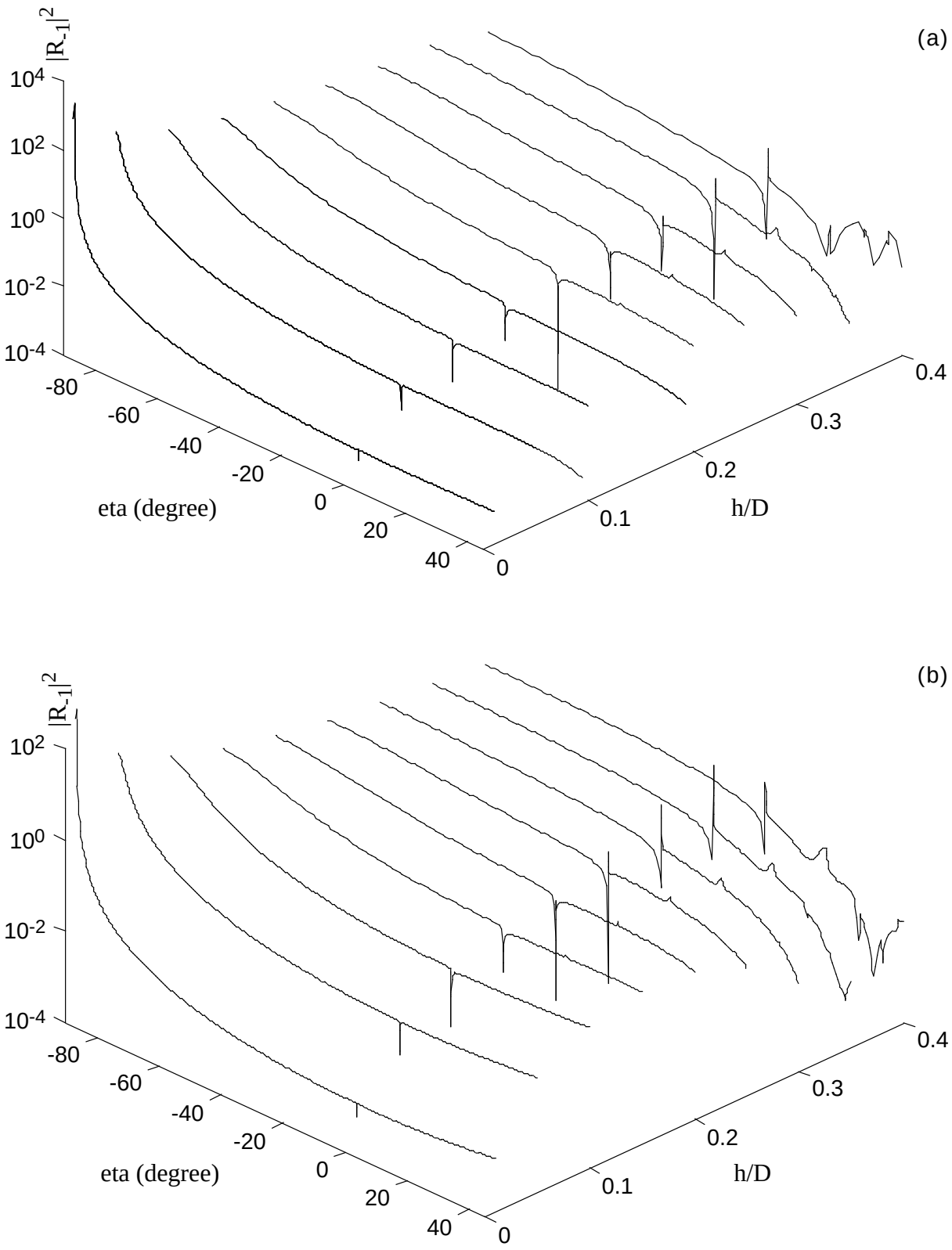


**FIGURE 3.11 : The radiation factor for a sinusoidal grating as a function of observation angle $\eta$ and grating depth for $\zeta$=0° and $\Psi_1$=0° and for electron energies of (a) 1 MeV and (b) 2 MeV.**

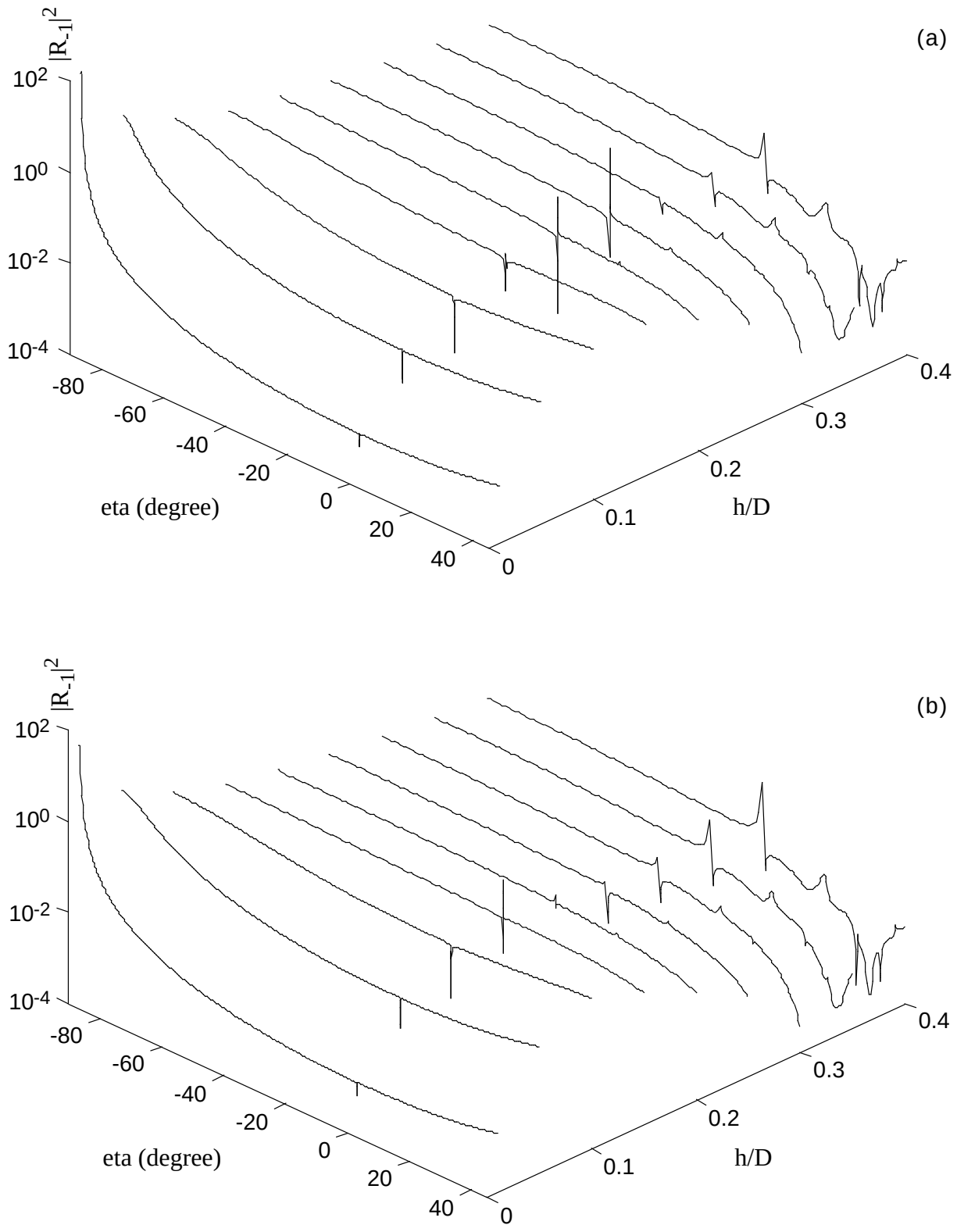


**FIGURE 3.12 : The radiation factor for a sinusoidal grating as a function of observation angle $\eta$ and grating depth for $\zeta=0°$ and $\Psi_1=0°$ and for electron energies of (a) 5 MeV and (b) 10 MeV.**

## 3.5 Full ($\eta$,$\zeta$) dependence of the radiation factor for $\Psi_1 = 0°$

Previous studies [38] have shown that for low energy electrons of about 100 keV, Smith-Purcell radiation is more intense out of the $\zeta$=0° plane, but no data are available yet for relativistic electrons. In the following, two types of grating will be discussed: the rectangular grating with parameters h/D=0.1 and a/D=0.5 and the sinusoidal grating with h/D=0.1. The radiation factor has been calculated for angles $\eta$<45° with the same angular mesh as before and for angles 0°≤$\zeta$≤85° in steps of one degree. The electrons are moving perpendicular to the grating rulings, therefore when using the reference frame described by Fig. 1.5, the calculations can be restricted to positive angles $\zeta$ (see equations ( 1.20 ), ( 1.38 ) and ( 1.39 ) for $\Psi_1$=0°).

Figs. 3.15 and 3.16 show the results obtained for an electron energy of 1 MeV displayed on 3D graphs with three different points of view for a better understanding. The view is specified in spherical coordinates by the azimuth and the elevation of the view point. Fig. 3.13 illustrates the coordinate system. In order to arrive at clear and understandable drawings, the following coding of the information has been used: the distance from a point to the origin is given by:

$$\log_{10}\left(\left|R_{-1}(\eta_n, \zeta_n)\right|^2\right) + 3 \qquad (3.2)$$

The color of a point of a surface is proportional to:

$$\left|R_{-1}(\eta_n, \zeta_n)\right|^2 \qquad (3.3)$$

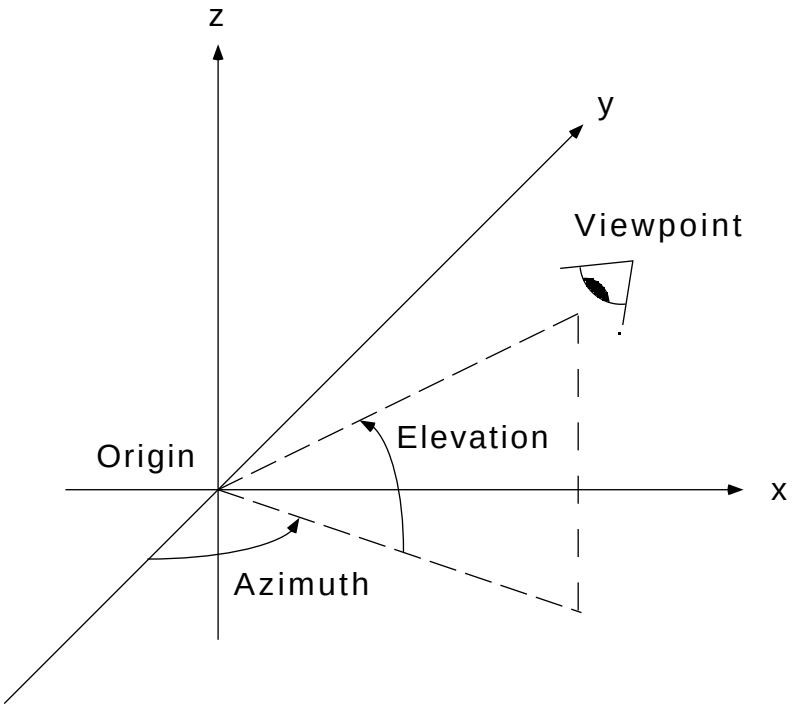


**FIGURE 3.13 : Coordinate system used in Figs. 3.15 and 3.16.**

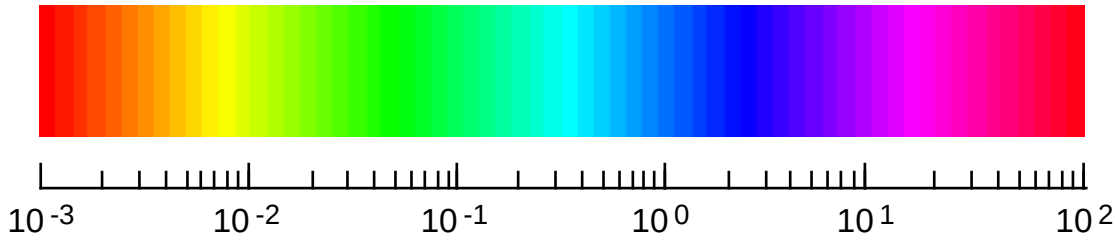


**FIGURE 3.14 : The color map used in Figs. 3.15 and 3.16.**

Fig. 3.14 shows the color map used in Figs. 3.15 and 3.16 according to Eq. 3.3.

As in the $\zeta$=0° plane, a strong increase of the radiation factor is observed for the rectangular grating with h/D=0.1 and a/D=0.5 just before a Wood-Rayleigh anomaly, where a strong decrease of the radiation factor occurs. The anomalies are strongly pronounced at all angles $\zeta$. A similar behaviour has been observed for this grating at 1, 2, 5 and 10 MeV.

Contrary to the rectangular profile, the radiation factor pattern for the shallow sinusoidal grating is very smooth, except in a small angular range near a Wood-Rayleigh anomaly, as for the $\zeta$=0° plane. The radiation factor patterns at 1, 2, 5 and 10 MeV are very similar.

For both gratings and at all considered energies, the radiation factor increases with increased angles $\zeta$ especially at backward angles $\eta$, but also in the forward direction ($\eta$>0). This property has been also observed at 2, 5 and 10 MeV.

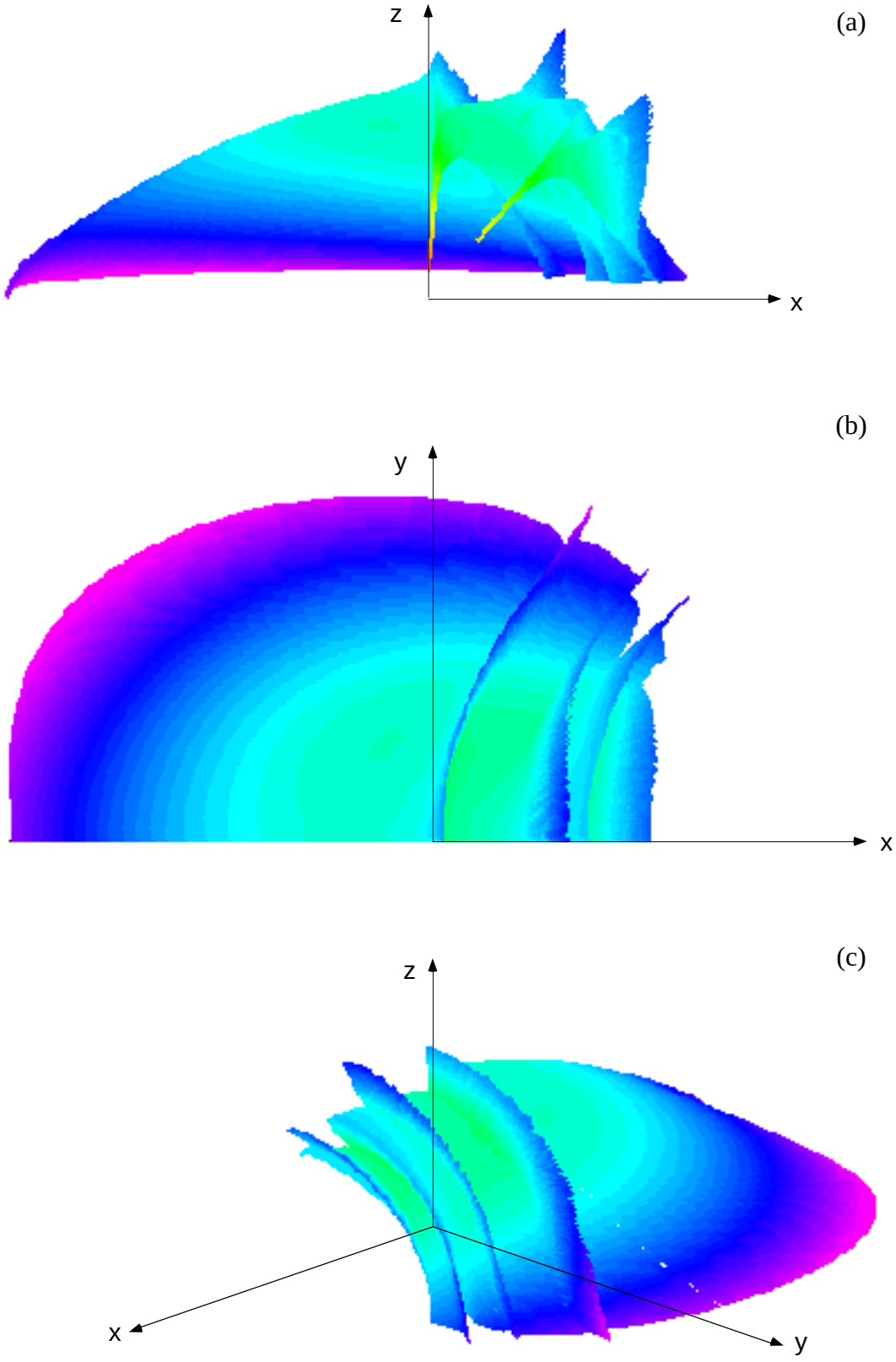


**FIGURE 3.15 : The radiation factor for a rectangular grating as a function of observation angles $(\eta,\zeta)$ for $\Psi_1=0°$ and for an electron energy of 1 MeV. The rectangular grating parameters are h/D=0.1 and a/D=0.5. (a) viewpoint (0,0), (b) viewpoint (0,90), (c) viewpoint (135,30).**

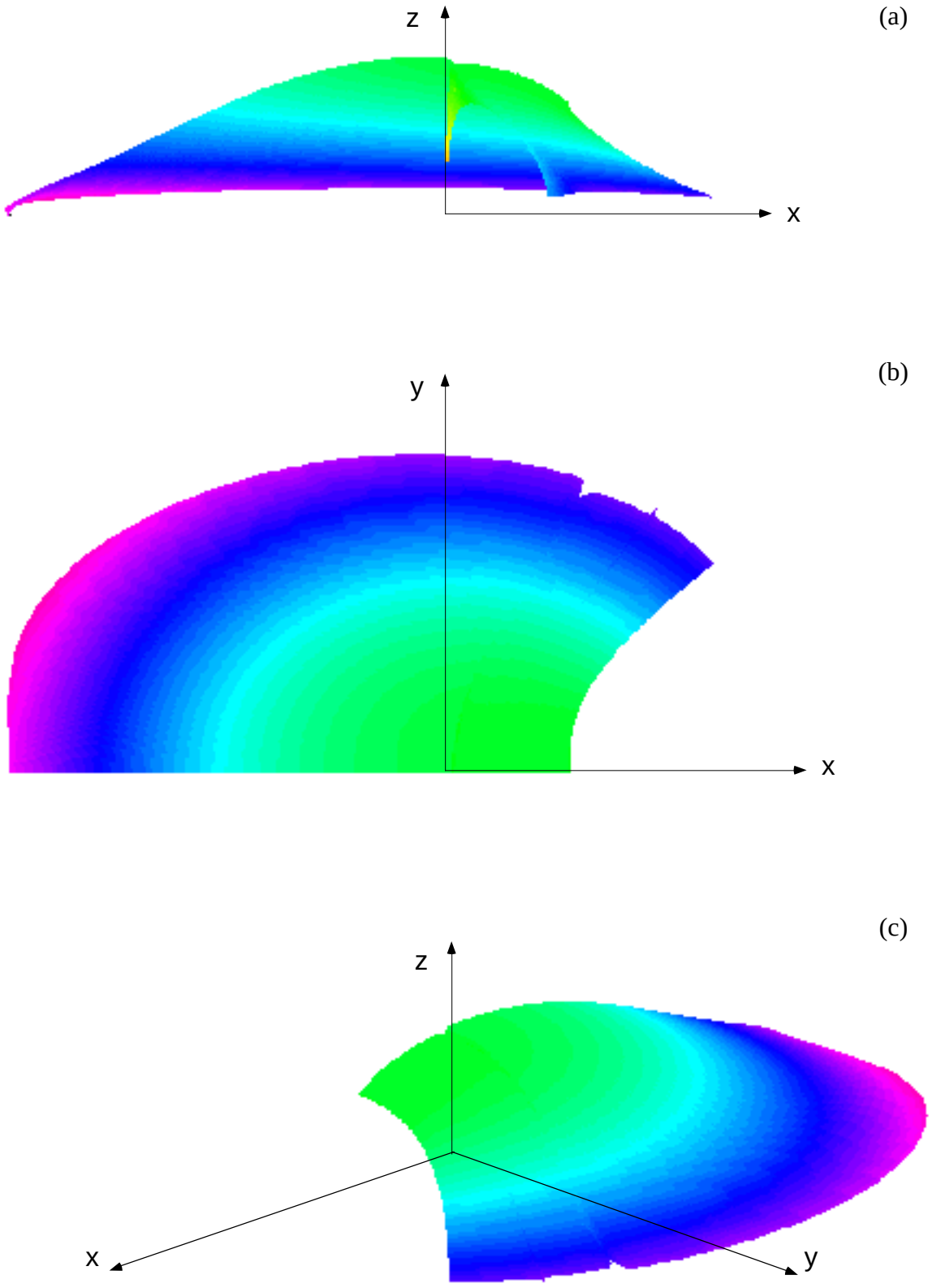


**FIGURE 3.16 : The radiation factor for a shallow sinusoidal grating as a function of observation angles $(\eta,\zeta)$ for $\Psi_1=0°$ and for an electron energy of 1 MeV. The grating parameter is h/D=0.1. (a) viewpoint (0,0), (b) viewpoint (0,90), (c) viewpoint (135,30).**

## 3.6 Influence of the tilting angle $\Psi_1$

Eq. 1.37 shows that rotating the grating around a vertical axis with respect to its surface provides an easy way to change the emitted radiation, because the apparent period as seen by the grating changes, and a continuous wavelength tuning is possible without changing the electron speed, nor the direction of observation, which is interesting from an experimental point of view. However, this property is useful only if the power emitted by the electron beam remains high when rotating the grating, which means that the radiation factor has to be kept large.

Fig. 3.17 shows the results as a function of the tilting angle $\Psi_1$ varying from 0 to 30° in steps of 5° and as a function the observation angle $\theta_n$ for $\varphi_n$=0°: the calculations were carried out using the ($\theta_n$,$\varphi_n$) reference frame described by Fig.1.4, which is more representative when $\Psi_1 \neq 0°$ than the ($\eta_n$,$\zeta_n$) reference frame usually used when $\Psi_1 = 0°$ [29][32]. Two cases have been considered: an electron energy of 2 MeV and a rectangular grating with a/D=0.1 and a/D=0.5 and an electron energy of 10 MeV and a shallow sinusoidal grating with h/D=0.1. For these two gratings, interesting results are obtained when $\Psi_1 = 0°$. The data are presented on a logarithmic scale.

For the lamellar grating with a/D=0.1 and h/D=0.5 at 2 MeV and in the forward direction, the radiation factor decreases slowly when tilting the grating. The curves are always characterized by strong variations of the radiation factor, especially near Wood-Rayleigh anomalies in the forward direction. For the sinusoidal grating at 10 MeV, the radiation factor is almost constant in the forward direction, and increases in the backward direction when $\Psi_1$ increases from 0 to 20°. For larger values of $\Psi_1$, the radiation factor decreases. The curves for the sinusoidal grating are smooth, with variations restricted in a very narrow angular range near the position of the Wood-Rayleigh anomalies. For both gratings, similar curves are obtained at 1, 2, 5 and 10 MeV.

It appears then that a grating which exhibits a high radiation factor when $\Psi_1 = 0°$ and therefore for which one expects a high intensity is not necessary suitable for tuning the emitted radiation according to Eq. 1.37. The radiation coefficient can be very low and therefore a weak emission of radiation is expected (sinusoidal grating at 10 MeV for $\Psi_1 = 30°$). Furthermore, a detailed investigation shows that for the considered lamellar grating, the position $\theta_n$ of the peak for the maximum of the radiation factor moves when $\Psi_1$ changes, and therefore the wavelength of maximum emission changes with $\Psi_1$ and with $\theta_n$. Then the interest of tuning the wavelength by tilting the grating decreases, because the direction of observation of maximal usefulness changes also.

A large tuning of the radiation needs a rapid dependence of the wavelength with the angle $\Psi_1$. Eq. 1.37 shows that the dependence is proportional to $1/\cos\Psi_1$. As a consequence, a strong dependence of the radiation factor with respect to $\Psi_1$ happens for large values of $\Psi_1$ only: an experiment designed to tune the wavelength by changing the angle of incidence of the electron beam necessitates a grating optimized for large angles $\Psi_1$ and for which the radiation factor is high in a fixed direction $\theta_n$.

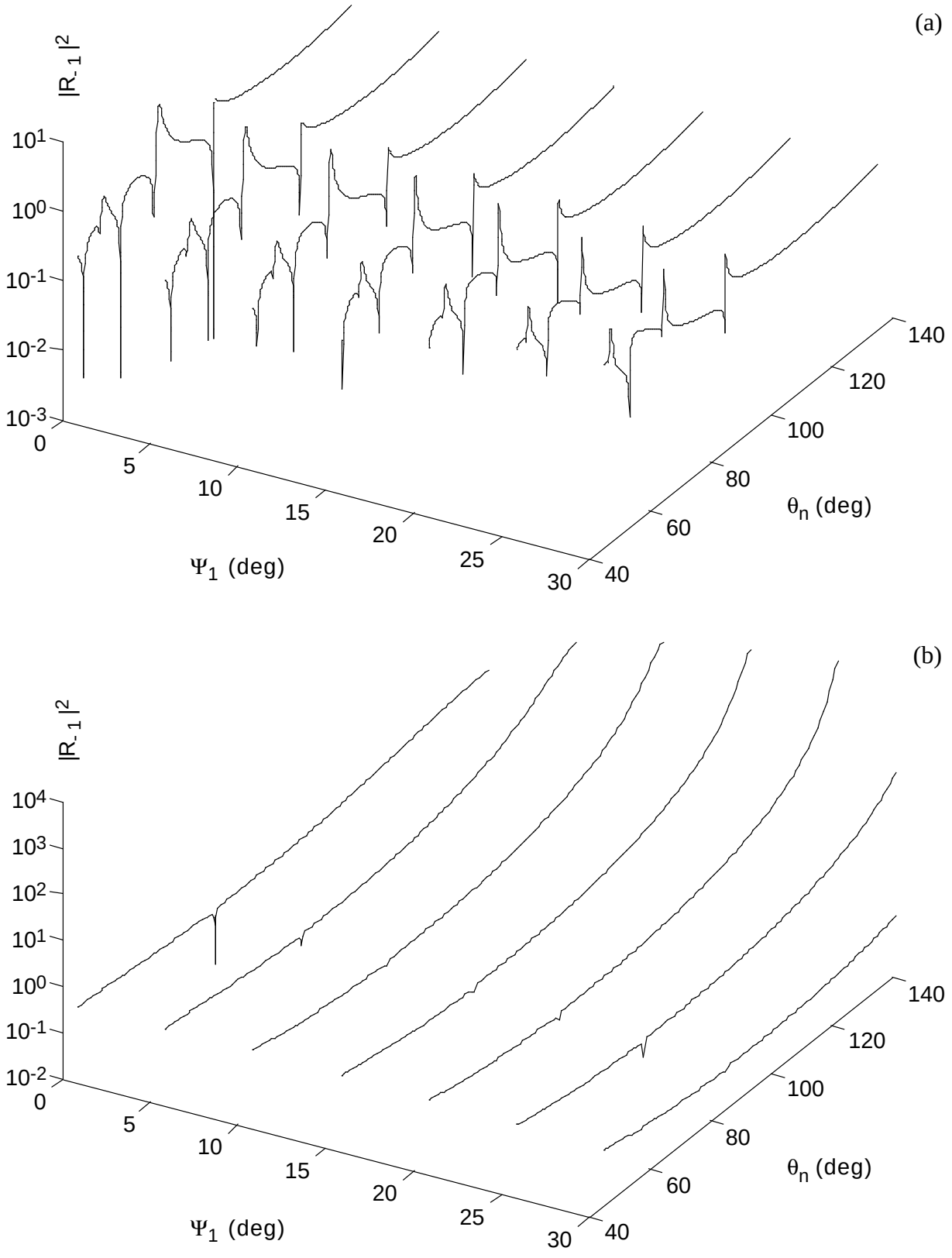


**FIGURE 3.17 : The radiation factor as a function of tilting angle $\Psi_1$ and angle $\theta_n$ at $\varphi_n=0°$ for: (a) a lamellar grating (a/D=0.1, h/D=0.5) and an electron energy of 2 MeV. (b) a sinusoidal grating with h/d=0.1 and an electron energy of 10 MeV.**

## 3.7 Emission diagrams

Figs. 3.18 to 3.25 show power distributions of Smith-Purcell radiation expressed in mW/sr for some of the electron energies and gratings discussed above. A two-dimensional Gaussian beam profile was assumed, but no divergence of the electron beam was considered. The beam axis is at a distance $z_0$ above the grating, which is shielded against electrons at z<0. The radiated power is given by Eq. ( 1.88 ):

$$\frac{dP}{d\Omega} = \frac{ei_0LD}{\varepsilon_0|n|^3\lambda^3} \cdot \cos^2\eta\cos^2\zeta \cdot |R_{-1}|^2 \cdot \frac{1}{2} erf\left(\frac{B}{\sqrt{8}\sigma_y}\right) exp\left(\frac{c^2}{4} - s_0\right) \left\{1 - erf\left(\frac{c}{2} - \frac{s_0}{c}\right)\right\}$$

with $i_0 = J_0 2\pi\sigma_y\sigma_z$ being the total current, $c = \sqrt{2}\sigma_z / h_{int}$, $s_0 = z_0 / h_{int}$

In the calculations, electron beam parameters achievable with modern linear accelerators have been used, i.e. a peak current $i_0$=10 A and $\sigma_x$=$\sigma_y$=1.5 mm. The beam axis is at $z_0$=1.5 mm which corresponds to $h_{int}$ at electron energies of 10 MeV and wavelengths of about 1 mm (observation at angle $\eta$ near 0° for a 1 mm period grating). The grating dimensions are a width B=5 cm and a length L=10 cm with a period D=1 mm. The beam and grating parameters were not optimized for maximizing the radiative power.

Figs. 3.18 and 3.19 show power distributions for shallow sinusoidal (h/D=0.1), rectangular gratings (a/D=0.5 and h/D=0.1) and blazed grating (with $\alpha_b$=10°) and for electron energies of 1, 2, 5, 10, 50 and 100 MeV. The plane of observation is perpendicular to the grating surface (i.e. at $\zeta$=0°) and the electron beam is moving perpendicular to the grating rulings (i.e. $\Psi_1$=0°).

For the shallow sinusoidal grating, the emission is higher in the forward direction, for short wavelengths and the emission increases when increasing the electron energy with a maximum for electrons of 10 MeV. For higher electron energies, the emission decreases again.

For the rectangular grating, the emission is concentrated in sharp peaks, generally located just before a Wood-Rayleigh anomaly. The maximum of emission is obtained at a rather low electron energy of 2 MeV and for longer wavelengths than for the sinusoidal grating.

For the shallow blazed grating, the emission is also concentrated in sharp peaks located before Wood-Rayleigh anomalies and the emission is maximum for electron energies of 2-5 MeV, but with lower values than for the lamellar or the sinusoidal gratings.

Due to the lower radiation coefficient calculated for the shallow symmetric triangular grating with h/D=0.1 (see Fig. 3.6), the Smith-Purcell emission is much lower than for the shallow lamellar, sinusoidal and blazed gratings, and this grating seems not interesting for Smith-Purcell radiation production.

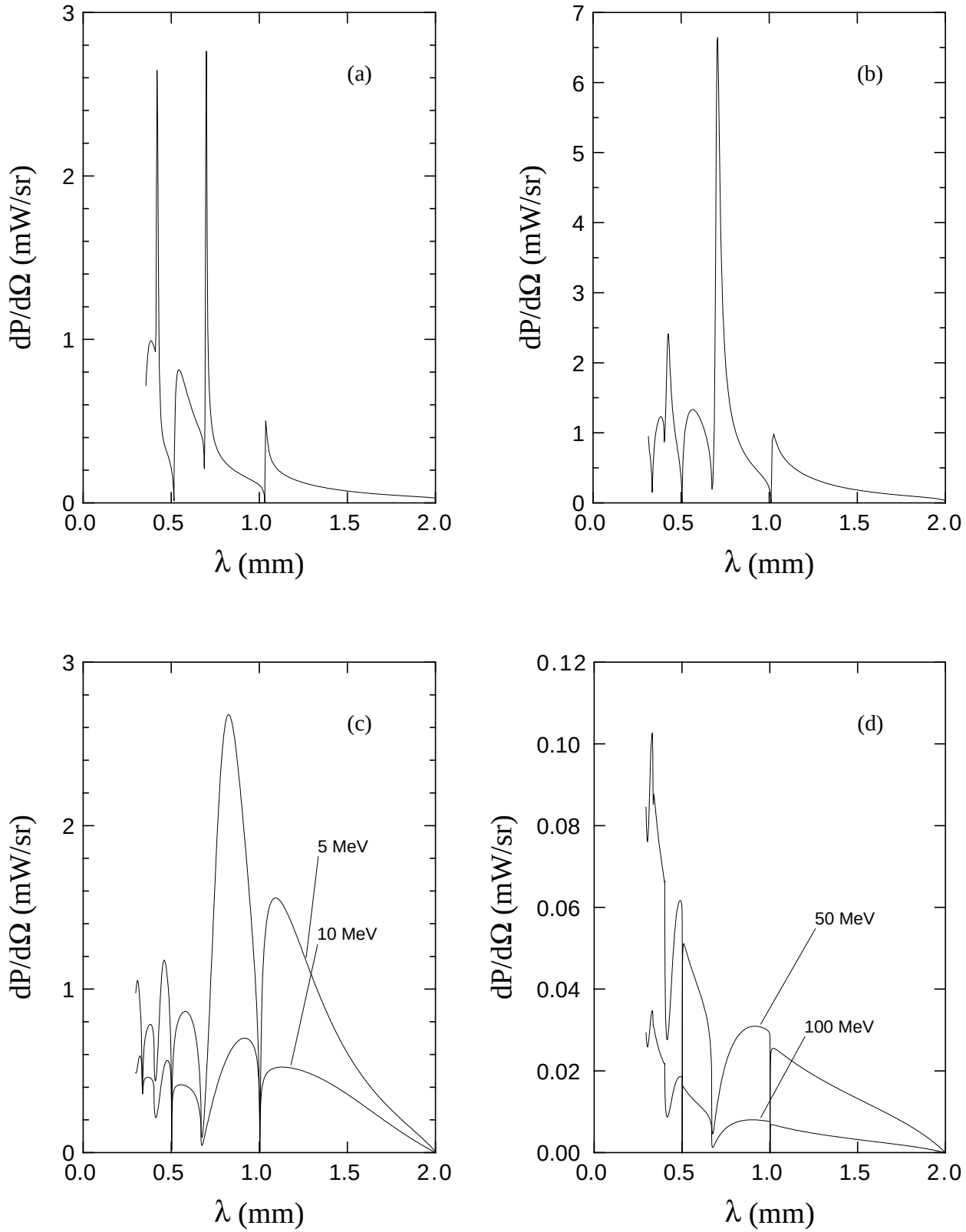


**FIGURE 3.18 : Spectra of SP radiation in first order at $\zeta$=0° and $\Psi_1$=0° using a rectangular grating with B=5 cm, L=10 cm, D=1 mm, h/D=0.1, a/D=0.5). Gaussian beam profile with $\sigma_y$=$\sigma_z$=1.5 mm at $z_0$=1.5 mm. Peak current of 10 A. Electron energies of (a) 1 MeV, (b) 2 MeV, (c) 5 and 10 MeV, (d) 50 and 100 MeV.**

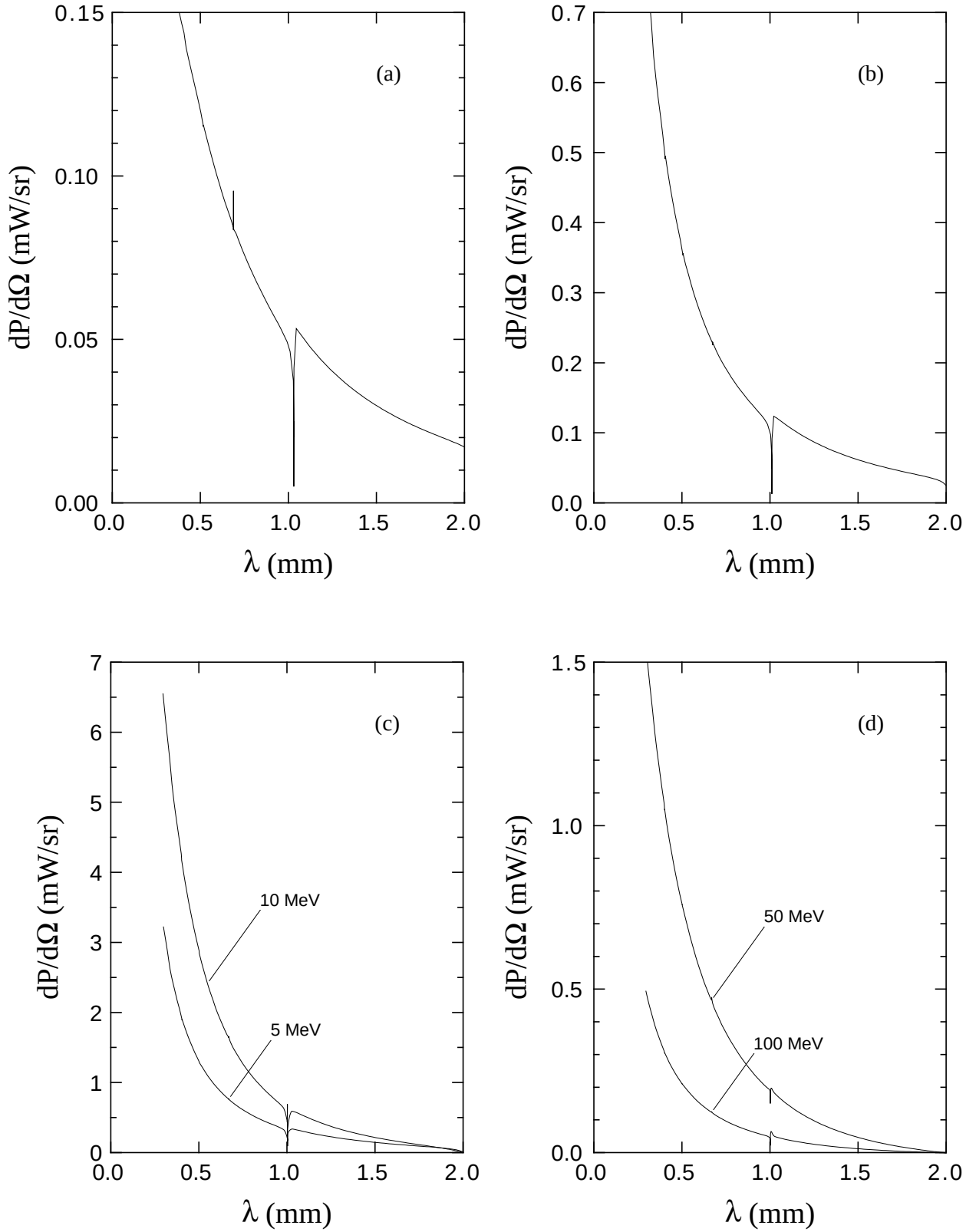


**FIGURE 3.19 : Spectra of SP radiation in first order at $\zeta$=0° and $\Psi_1$=0° using a sinusoidal grating with B=5 cm, L=10 cm, D=1 mm, h/D=0.1. Gaussian beam profile with $\sigma_y$=$\sigma_z$=1.5 mm at $z_0$=1.5 mm. Peak current of 10 A. Electron energies of (a) 1 MeV, (b) 2 MeV, (c) 5 and 10 MeV, (d) 50 and 100 MeV.**

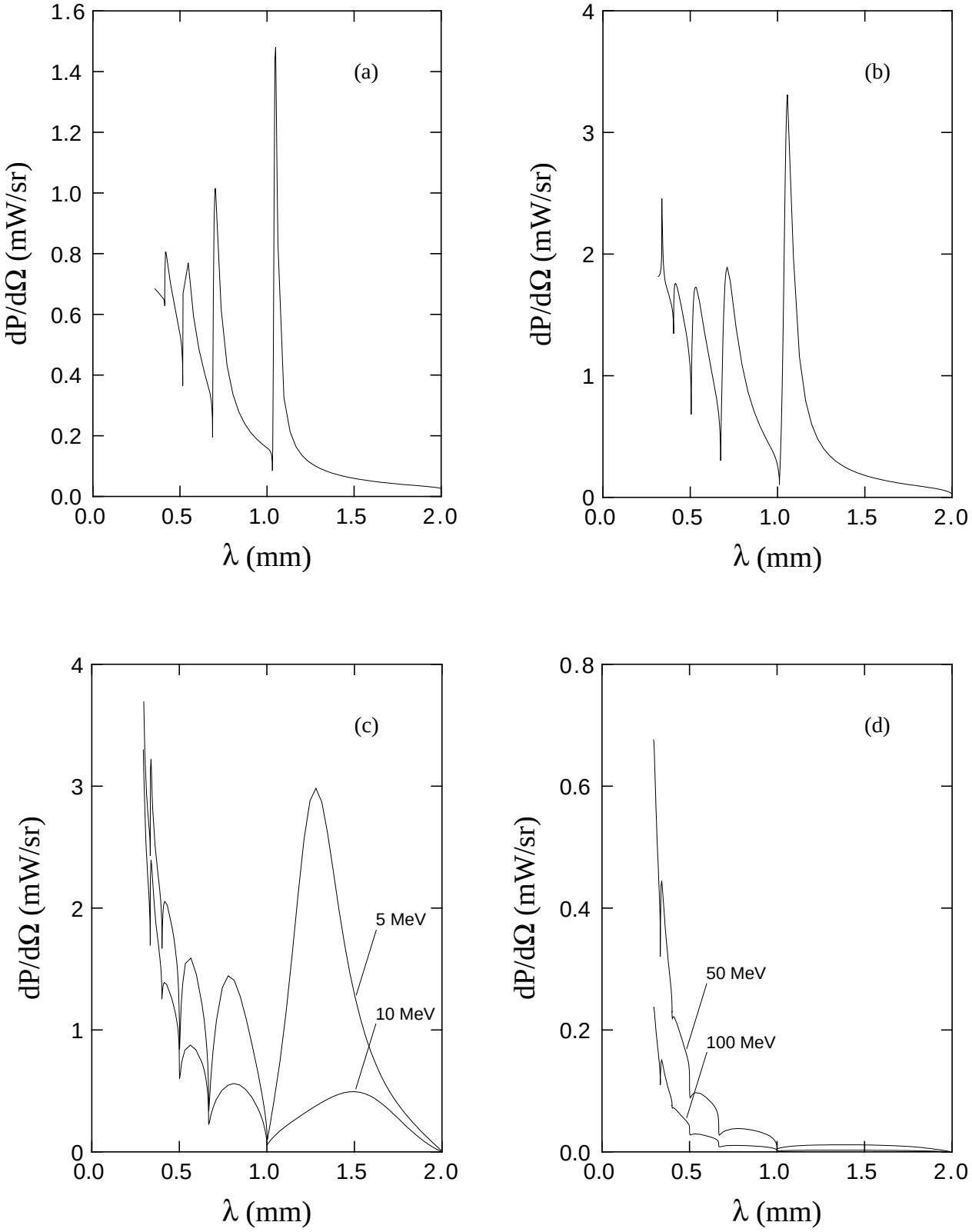


**FIGURE 3.20 : Spectra of SP radiation in first order at $\zeta$=0° and $\Psi_1$=0° using a blazed grating with B=5 cm, L=10 cm, D=1 mm, $\alpha_b$=10°. Gaussian beam profile with $\sigma_y$=$\sigma_z$=1.5 mm at $z_0$=1.5 mm. Peak current of 10 A. Electron energies of (a) 1 MeV, (b) 2 MeV, (c) 5 and 10 MeV, (d) 50 and 100 MeV.**

Fig. 3.21 shows a comparison of Smith-Purcell spectra calculated with a 5 MeV electron beam with $i_0$=10 A and $\sigma_x=\sigma_y$=1.5 mm passing over a grating at $z_0$=1.5 mm and different shallow gratings with sinusoidal or lamellar profile. A set of gratings with proper parameters could be used to tailor the emission to the experimental needs, adapting the characteristics of the Smith-Purcell spectra. The shallow sinusoidal grating emits more at short wavelengths, while the three considered rectangular gratings exhibit a peak of emission at different wavelengths.

Fig. 3.22 shows spectra calculated for a 1 mm period grating and several electron energies between 5 and 8 MeV (with same beam parameters as before). Continuous tuning of the peak intensity in the Smith-Purcell spectra is possible by varying the electron energy: the peak of emission is shifted from 1.04 to 1.18 mm when the electron energy increases from 5 to 8 MeV.

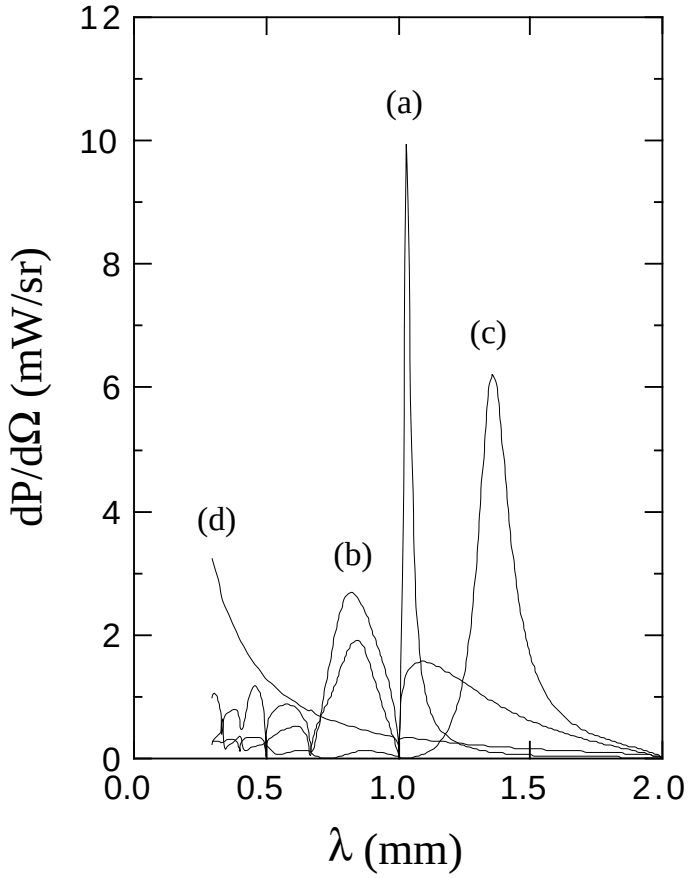


**FIGURE 3.21 : Comparison of Smith-Purcell spectra in the first order at $\zeta$=0° and $\Psi_1$=0° using a 5 MeV electron beam and different gratings with B=5 cm, L=10 cm, D=1 mm. Gaussian beam profile with $\sigma_y=\sigma_z$=1.5 mm at $z_0$=1.5 mm. Peak current: 10 A. (a) rectangular grating with h/D=0.1, a/D=0.1; (b) rectangular grating with h/D=0.1, a/D=0.5; (c) rectangular grating with h/D=0.1, a/D=0.9; (d) sinusoidal grating with h/D=0.1.**

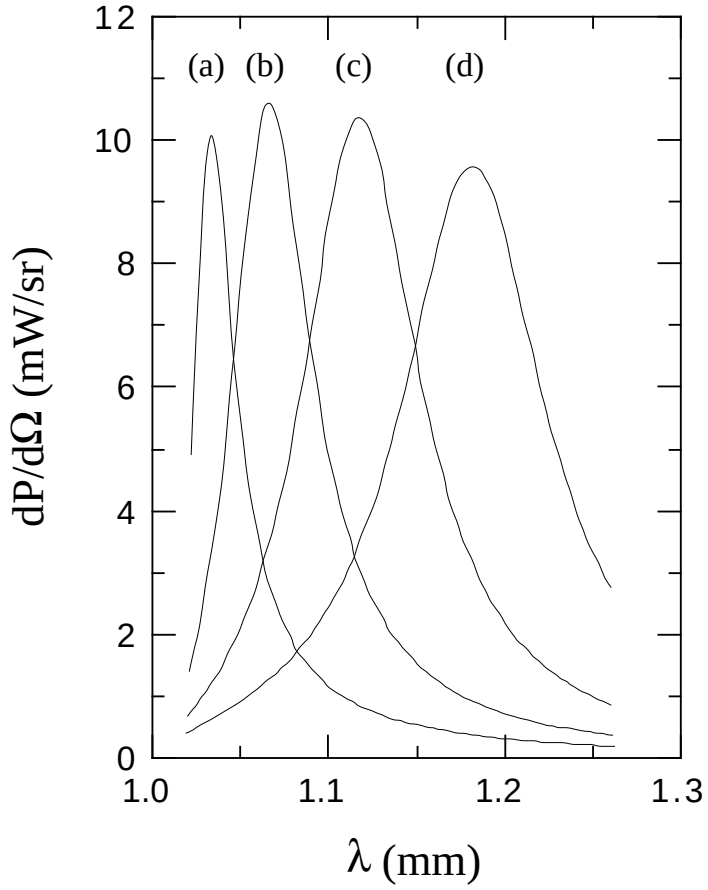


**FIGURE 3.22 : Smith-Purcell spectra in the first order at $\zeta$=0° and $\Psi_1$=0° using a rectangular grating with B=5 cm, L= 10 cm, D=1 mm, h/D=0.1 and a/D=0.1. Gaussian beam profile with $\sigma_y=\sigma_z$=1.5 mm at $z_0$=1.5 mm. Peak current of 10 A. Electron energies of (a) 5 MeV, (b) 6 MeV, (c) 7 MeV, and (d) 8 MeV.**

Fig.3.23 shows emission diagrams as a function of observation angles $\eta$ and $\zeta$ calculated when using a lamellar grating with h/D=0.1 and a/D=0.5 for an electron beam energy of 2 MeV and using a sinusoidal grating with h/D=0.1 for an electron beam energy of 10 MeV for an angle $\Psi_1$=0°, for which a reasonable intensity was calculated at $\zeta$=0°. The beam parameters (FHWM, position etc..) and the grating dimensions are the same than in the previous calculations. A pseudoplot has been chosen to illustrate the properties of the emission with observation angles $\eta$ and $\zeta$ for the x- and y-axis and coloration proportional to the intensity of the emission. The color map is described on the figure itself. Due to the configuration of the experiment, the emission is symmetric with respect to $\zeta$ and the figures have been drawn for positive angle $\zeta$ only. The emission for the lamellar grating is noticeable in the forward direction and is concentrated in narrow bands just before Wood-Rayleigh anomalies and decreases when increasing $\zeta$. The largest intensity is emitted near $\eta$=20° and for angle $\zeta\leq$10°. The radiation diagrams exhibit similar properties at 1, 2, 5 and 10 MeV. When using a shallow sinusoidal grating, the emission is concentrated in the forward direction for $\eta$=45° and for $\zeta\leq$3°. A similar behaviour has been noticed at 1, 2, 5 and 10 MeV.

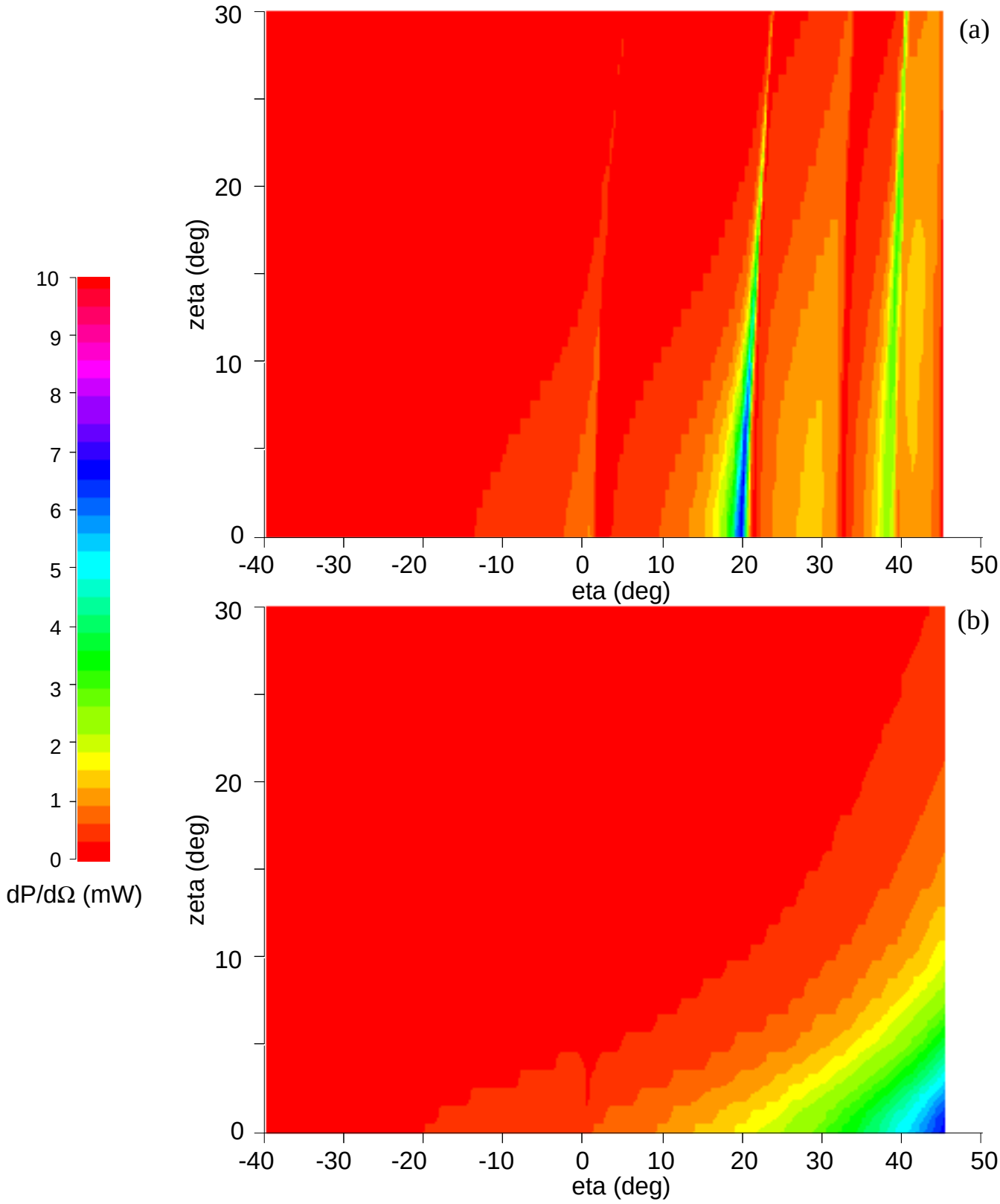


**FIGURE 3.23 : Spectra of Smith-Purcell radiation in the first order as a function of angles η and ζ for $\Psi_1$=0°. (a) using a rectangular grating (h/D=0.1, a/D=0.5) and a 2 MeV electron beam. (b) using a sinusoidal grating (h/D=0.1) and a 10 MeV electron beam. Same beam parameters and grating size as before.**

Fig.3.23 shows emission diagrams as a function of the angle of incidence $\Psi_1$ of the electron beam with respect to the grating rulings direction. The calculations were carried out for angles of observation $45° \leq \theta_n \leq 135°$ and $\varphi_n = 0°$ using a rectangular grating with parameters h/D=0.1 and a/D=0.5 for an electron beam energy of 2 MeV and using a sinusoidal grating with h/D=0.1 for an electron beam energy of 10 MeV. The grating size and beam parameters are the same than in the previous calculations. The results are presented as a function of the wavelength using Eq. ( 1.37 ). For $\Psi_1 = 0°$, reasonable intensities have been calculated in these two configurations (cf. Figs. 3.18(b) and 3.19(c)).

For a 2 MeV electron beam interacting with the considered rectangular grating the maximum intensity is always observed in sharp peaks before Wood-Rayleigh anomalies. The intensity decreases slowly when increasing the angle $\Psi_1$ but reasonable values are obtained up to $\Psi_1 = 25°$, which permits a tuning of the wavelength within 10% at a fixed angle $\theta_n$: the 10% correspond to 1/cos(25°). Unfortunately, the angle $\theta_n$ corresponding to the maximal intensity changes when tilting the grating and therefore tuning of the radiation is difficult by this way. The curves calculated at 1, 5 and 10 MeV are very similar.

For a 10 MeV electron beam interacting with a sinusoidal grating with h/D=0.1 the maximum of emission is always observed for $\theta_n = 45°$, but the intensity decreases very fast when increasing $\Psi_1$ and very low values are obtained when $\Psi_1 \geq 10°$. Similar results are obtained at 1, 2 and 5 MeV for this grating.

Fig. 3.25 shows the spectrum of Smith-Purcell radiation calculated for a 2 MeV electron beam coming at an angle $\Psi_1 = 20°$, interacting with a lamellar grating with parameters h/D=0.1 and a/D=0.5 and for observation angles $-45° \leq \varphi_n \leq 45°$ and $45° \leq \theta_n \leq 135°$ (cf. Fig. 1.4). The result is presented as a function of the angle $\varphi_n$ and of the wavelength using Eq. ( 1.37 ). The same color map as in Fig 3.23 has been used but going from 0 to 6 mW instead of going from 0 to 10 mW, in order to enhance the contrast. The maximum of emission is 5.5 mW at a wavelength of about 0.7 mm near $\varphi_n = 0°$. The most remarkable feature is that the emission pattern is not symmetric any more with respect to the angle $\varphi_n$ or, which is equivalent, with respect to the electron beam trajectory. The emission is concentrated in peaks near Wood-Rayleigh anomalies, but the maximum of emission is not observed for $\varphi_n = 0°$, as it was noticed when $\Psi_1 = 0°$, especially in the forward direction at shorter wavelengths.

Therefore, it seems that tilting the grating does not offer a very easy way to tune the wavelength for relativistic electrons in the 1-10 MeV range and using the considered shallow gratings to produce radiation at far-infrared and millimeter wavelengths, because either the intensity becomes very low when tilting the grating or the direction of maximal intensity changes. When it is possible, using a set of gratings or tuning the electron energy seems easier as shown in Figs. 3.18 to 3.22.

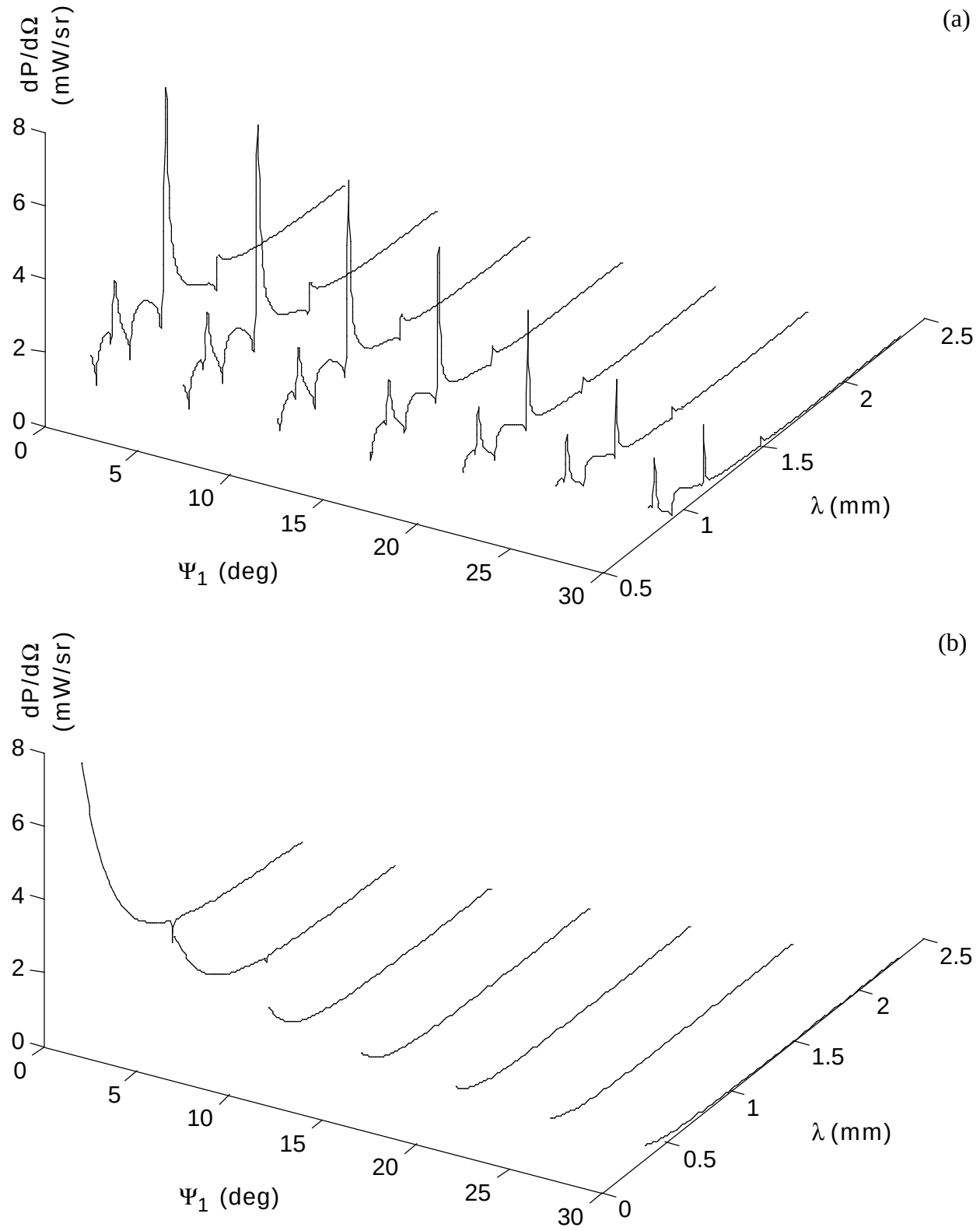


**FIGURE 3.24 : Spectra of Smith-Purcell radiation in the first order as a function of angle $\Psi_1$ for $45° \leq \theta_n \leq 135°$ at $\varphi_n = 0°$. The results are presented as a function of the wavelength using Eq. ( 1.37 ). (a) using a lamellar grating (h/D=0.1, a/D=0.5) and a 2 MeV electron beam. (b) using a sinusoidal grating (h/D=0.1) and a 10 MeV electron beam. Same beam parameters and grating size as before.**

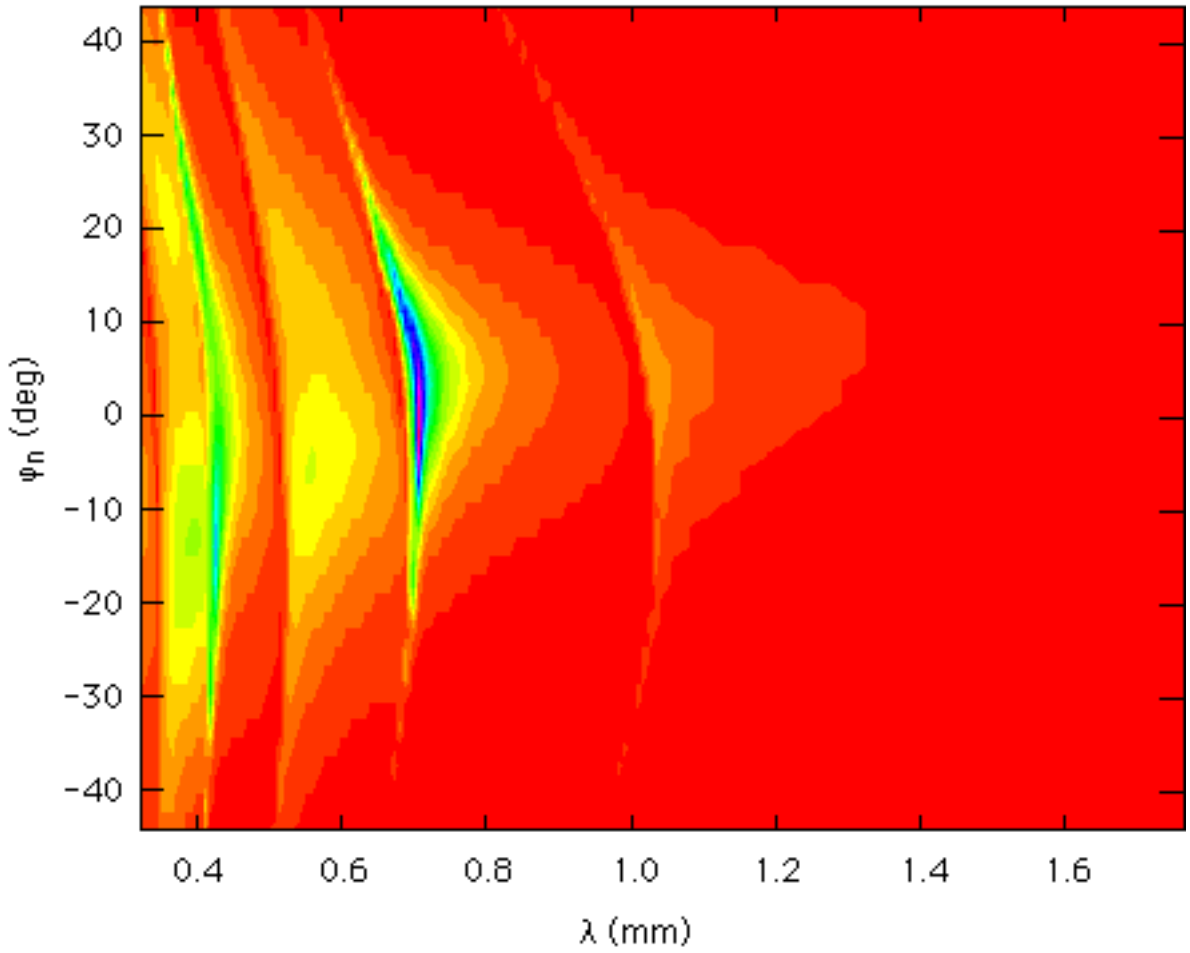


**FIGURE 3.25 : Spectrum of Smith-Purcell radiation in the first order as a function of the wavelength and the observation angle $\varphi_n$ for $\Psi_1$=10° for a 2 MeV electron beam interacting with a lamellar grating with h/D=0.1 and a/D=0.5. Same beam parameters and grating size as before. Same color map as Fig. 3.23.**

## 3.8 Discussion

For wavelengths of the order of a millimeter and for relativistic electrons with energies larger than 1 MeV, the interaction height is large: for a 10 MeV beam, $h_{int} \cong 1.6\lambda$ at $\zeta$=0°. Therefore careful alignment of the electron beam close and parallel to the grating surface is not mandatory for production of photons in the far-infrared or millimeter range and electron beams with a diameter of the order of 1 mm would efficiently interact with the grating. The finite divergence $\Theta$ of an actual beam can be neglected as long as $\Theta < h_{int}/L$ (c.f. paragraph 1.6.2).

The preceding calculations show that the Smith-Purcell radiation produced by relativistic electrons exhibits some interesting features. Electron beams with moderate energy in the 1 to 10 MeV range could be used to produce far-infrared or millimeter radiation by interaction with millimeter period gratings. The use of higher electron energies seems to be of no advantage in this spectral range. The radiation characteristics can be adapted to the experimental needs by a

proper choice of the experimental configuration, choosing the adequate grating and electron energy. A continuous tuning is also possible by varying the angle of observation.

Rotating the grating (i.e. changing the angle $\Psi_1$) is a convenient way to tune the wavelength of the radiation without changing the grating, the direction of observation or the electron energy, operations which could be difficult in an experimental configuration but a grating optimized for such a configuration has to be used: high efficiency at a fixed angle $\theta_n$ and for a large variation of $1/\cos\Psi_1$ in order to provide a large tuning of the wavelength with a reasonable intensity.

By collimating the Smith-Purcell radiation into a solid angle $\Delta\Omega=\cos(\eta)\Delta\eta\Delta\zeta$ one obtains radiation of bandwidth $\Delta\lambda/\lambda=\cos(\eta)\Delta\eta[\beta^{-1}-\sin(\eta)]^{-1}$ for the first propagative order. Using a 5 MeV Gaussian electron beam with a peak current of 10 A and $\sigma_y=\sigma_z=1.5$ mrad, the center of the beam being at $z_0=1.5$ mm, interacting with a lamellar grating with h/D=a/D=0.1, a peak photon flux of $5*10^{13}$ photons/s in a solid angle of 1 μsr can be obtained (cf. the maximum of curve 3.21 (a) near $\lambda=1$ mm). This photon flux would be quasi-monochromatic with a bandwidth $\Delta\lambda/\lambda\sim10^{-3}$. For comparison, a 1 $cm^2$ perfect blackbody at 2000 K emits $10^8$ photons/s/μsr at 1 mm for the same bandwidth.

It has to be noted that the technological needs in designing a Smith-Purcell source are modest compared to other sources like synchrotron radiation sources on electron storage rings: the heart of the source would be an accelerator of moderate energy and relatively low cost and the radiation device is a grating which can be easily produced for radiation in the far infrared or millimeter range, as shown by the experimental results obtained by Doucas *et al*. [65] using a 3.6 MeV electron beam. A precise comparison between a Smith-Purcell source and other sources like synchrotron radiation sources or black-body sources remains to be done: considerations like costs, facility to built and to use have to be taken into account with the sources characteristics to determine their actual performances. It has to be noted that the time structure of these sources is different (continuous for the blackbody, CW for a storage ring and pulsed with picosecond resolution for a linear accelerator), which leads to different possible applications. The performances have also to be compared with those of Free Electron Lasers, which are based on a stimulated effect and therefore are powerful sources.

# CHAPTER 4 The GELINA facility

In the previous parts, a theoretical description of the Smith-Purcell effect was presented, and calculations for electrons in the 1 to 100 MeV energy range have been carried out. An experimental study of the radiation produced by relativistic electrons interacting with optical gratings was carried out at the GELINA facility, which is described in the next sections.

## 4.1 The GELINA accelerator

The Geel Linear Accelerator (GELINA) is an S-band linear accelerator built in 1965 and upgraded in 1976 and 1984 [68][69]. Up to now the accelerator was mainly used for neutron differential cross section and neutron spectroscopy experiments using a neutron source at the end of the 0° beamline. The accelerated electrons interact with an uranium rotating target to produce neutrons by a ($\gamma$-n) process. A post-acceleration pulse compression system permits to deliver an electron pulse of less than 1 ns duration. Using up to 400 m long neutron flight paths, this facility allows to carry out neutron measurements with excellent energy resolution.

The different parts of the accelerator are the injector, a prebunching cavity, a standing wave buncher and two 6 m long accelerating sections. In the buncher, the electrons are accelerated up to 20 MeV and grouped together in a structure which allows the acceleration in the next two travelling wave sections. The maximum energy of the electrons at the end of the last section is 140 MeV. At full current and short pulse length, the energy dispersion is 50% (FWHM). This large intrinsic electron energy spread is used in a compression magnet to reduce the time width of the electron pulses.

The triode electron gun has a heated dispenser cathode which is put at -80 kV with respect to the anode (at zero potential). The grid is biased at -1 kV with respect to the cathode to prevent electrons from being emitted continuously. The gun is triggered by applying a positive pulse to the grid, generated by a large-bandwidth three-stage amplifier. The gun delivers a peak current of up to 20 A at 80 keV to the prebunching cavity. The pulse time width is tunable between 10 ns and 2 μs.

The prebunching cavity and the standing-wave buncher group the electrons together into structures called microbunches to allow the acceleration in the two successive travelling-wave sections. The electron energy is 20 MeV at the entrance of the acceleration section.

After acceleration in the two sections each electron pulse consists of a sequence of microbunches having a width of the order of 10 ps and spaced with 0.33 ns corresponding to the 3 GHz frequency of the klystrons delivering the travelling wave. The filling time of the acceleration cavities is of the order of 1 μs. Therefore at short pulse lengths and high current the accelerator delivers electron pulses consisting of microbunches having a sequentially decreasing energy ranging from 140 to 70 MeV: a microbunch travelling through the accelerator finds on its way less stored electromagnetic energy available for acceleration than its forerunner because that one already took part of the stored electromagnetic energy to be accelerated.

Figure 4.1 shows the GELINA accelerator with the power supplies. The accelerator is installed in a special gallery, separated from the neutron target hall. The power electronics is installed in a separate hall.

At the exit of the machine the electron beam is transported to the neutron target by a 12 m long beam line. The electron pulses can be compressed in a 360° bending magnet [69] where the dispersion of electron energies leads to a dispersion of electron trajectories, the highest-energy bunches entering first having a longer trajectory than the lower energy electrons entering later. Since all electrons have almost the same speed very close to the speed of light, at exit of the magnet the microbunches are grouped together, reducing the total pulse width to about 1 ns, as illustrated in figure 4.2.

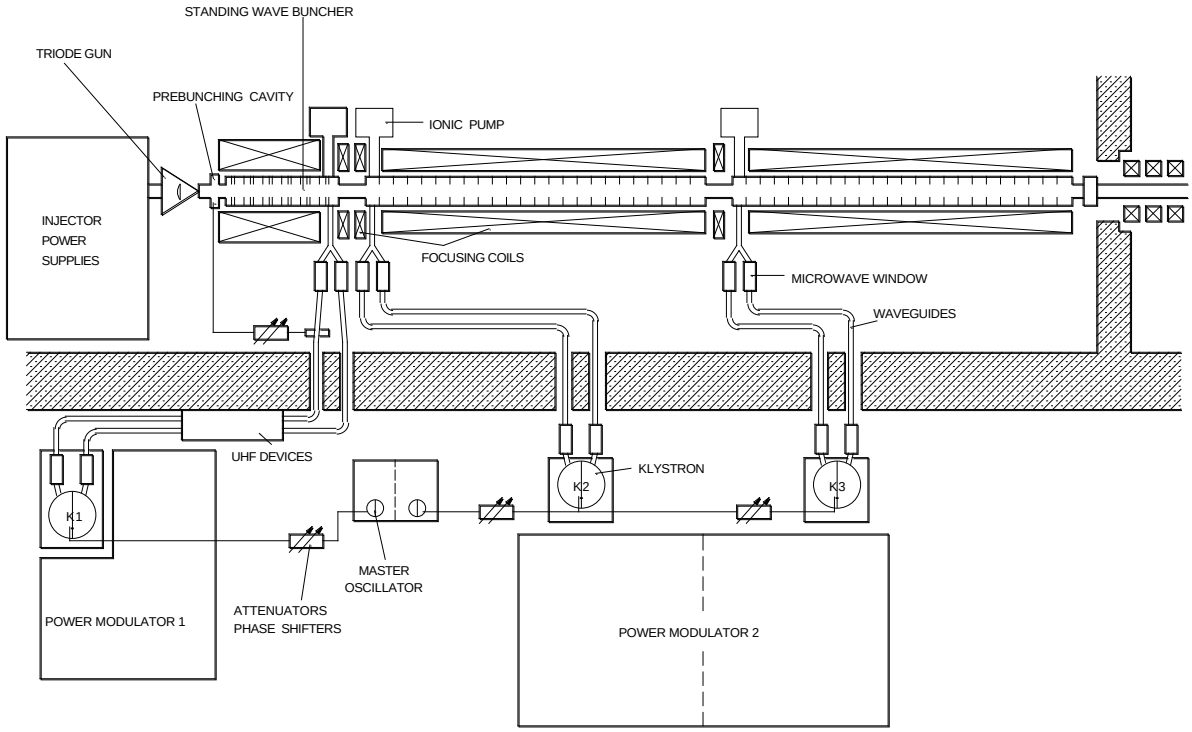


**FIGURE 4.1 : Scheme the GELINA linear accelerator.**

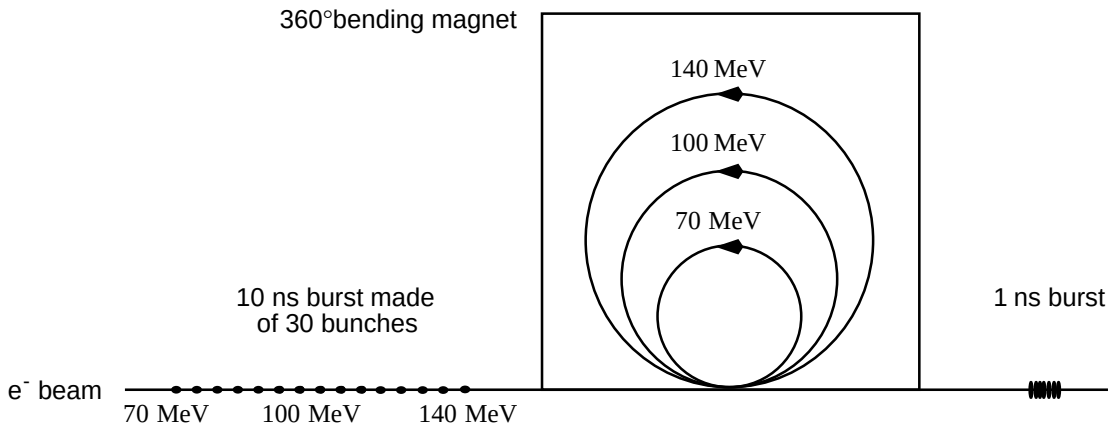


**FIGURE 4.2 : The compression magnet: the achromaticity of the electron beam is used to reduce the pulse length via a spatial dispersion.**

Taking profit of the spatial separation of the microbunches in the 360° bending magnet, it might be possible to isolate one single bunch of 10 ps out of the 30 bunches in a 10 ns long pulse. This possibility, combined with the tunable repetition rate of the linear accelerator, would provide a unique facility for time-resolved measurements using X-rays.

Table 4.1 shows typical parameters of the GELINA accelerator.

**TABLE 4.1 : Beam parameters mostly used.**

| beam energy (MeV) | pulse length (ns) | frequency (Hz) | peak current (A) | mean current (μA) | neutron burst (n/s) |
|---|---|---|---|---|---|
| without compression | | | | | |
| 100 | 10 | 800 | 12 | 96 | $5.6\ 10^{18}$ |
| 100 | 10 | 100 | 12 | 12 | $7.0\ 10^{17}$ |
| with compression | | | | | |
| 100 | 0.6 | 800 | >100 | 75 | $4.6\ 10^{19}$ |
| without compression for OTR and Smith-Purcell experiments | | | | | |
| 20-120 | 1000 | 50 | 0.02-0.1 | 1-5 | / |

The repetition rate of the accelerator can be tuned continuously between 1 and 800 Hz using a pulse generator driven by a Macintosh IIci.

The peak current is adjusted by tuning the grid-cathod potential. In order to provide low current electron beams, this potential was decreased as much as possible. Simultaneously, the heating of the cathode was decreased. With this method, it was possible to generate time-averaged currents of the order of 5 μA, approximately eight orders of magnitude smaller than the normal working regime of the accelerator [12].

The electron beam energy was selected by varying the RF power injected by the klystrons into the two accelerating sections.

The beam shape and the beam position were tuned using a set of focusing coils, dipoles, quadrupoles and steering coils located at the accelerator and along the beam line.

## 4.2 The target hall

The experiments of the present work were carried out using the main beam line in the target hall. Figure 4.3 shows the inner part of the target hall. The compression magnet, the neutron target and the entrances of the flight-paths are visible on top of the drawing. For safety during installation or maintenance and for improving the life-time of the materials, the radiation physics facilities are installed at the beginning of the target hall, as far away as possible from the neutron target. The outside is shielded against radiation (neutron and gamma-rays) by 3.5 m concrete walls. Two holes were drilled into the concrete to permit the extraction of the OTR and XTR beam to a separate hall, where the appropriate detectors are installed.

Figure 4.4 shows the position of the three available beamlines in the GELINA target hall and of the magnetic energy analyser used to measure the beam energy. The dipole magnet located after the energy analyser directs the beam into the main beam line for neutron production or into one of the two achromatic deflections which are used for photo-activation or XTR experiments. A vacuum chamber has been installed on the main beamline and was used for optical transition radiation measurements and for the Smith-Purcell experiments.

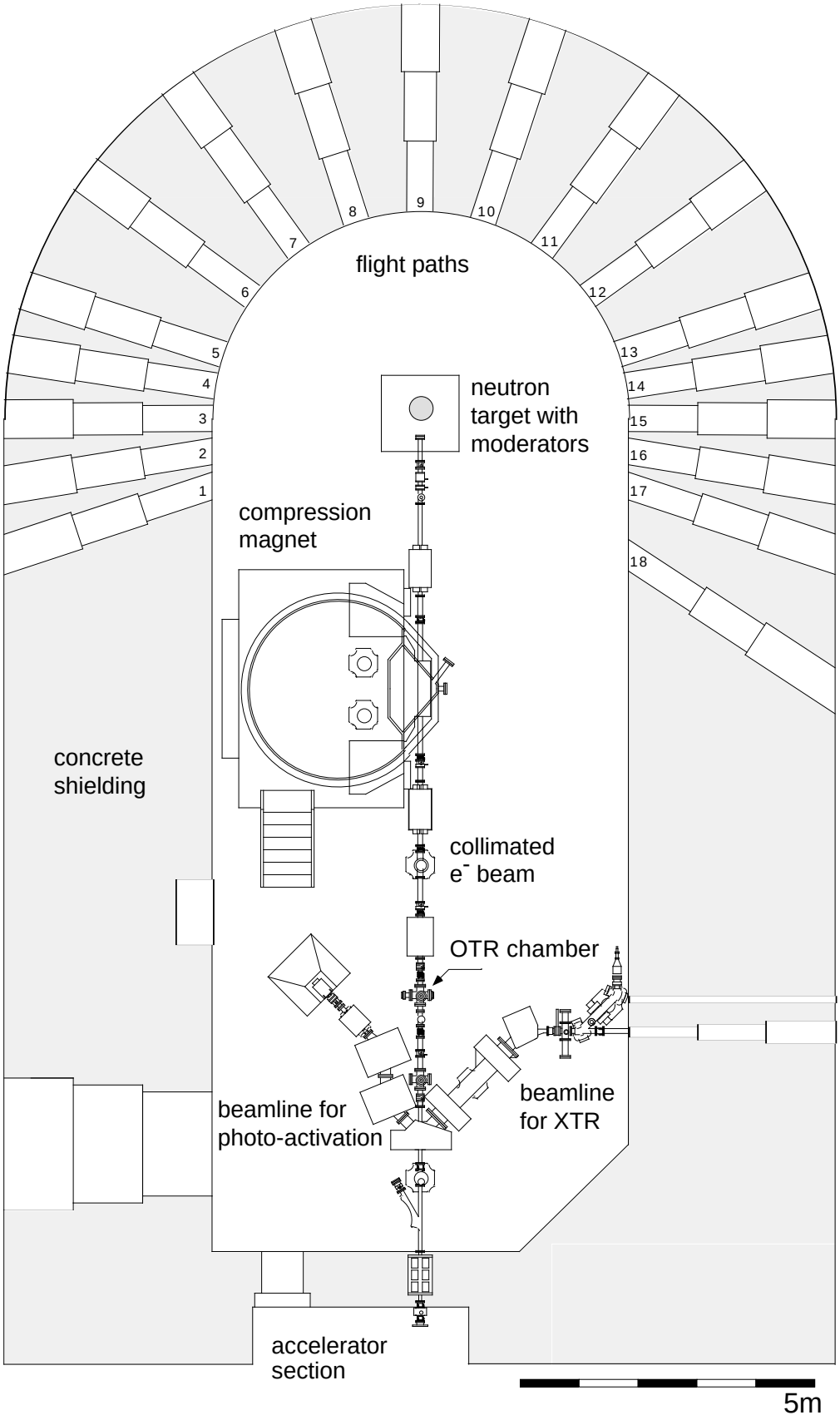


**FIGURE 4.3 : The target room at Geel.**

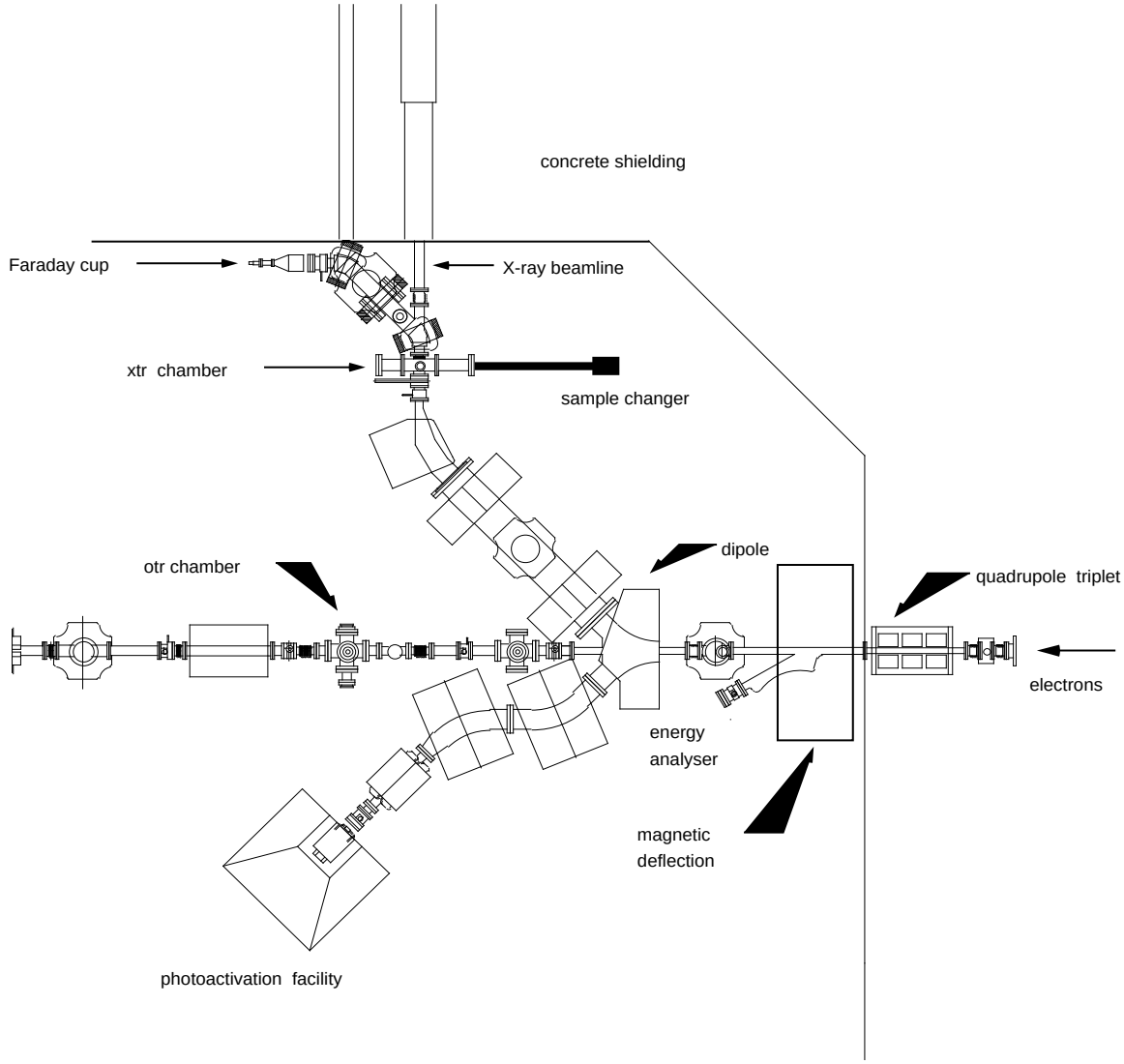


**FIGURE 4.4 : Detail of the target hall.**

## 4.3 Measurements of the beam current

In order to avoid a fast destruction of the radiators, the Smith-Purcell experiments had to be carried out at low peak currents, far below the normal working regime of the accelerator. A fast ferrite is installed at the exit of the accelerator. It measures the current used for the experiment and gives the pulse shape. Figure 4.5 shows a typical current measurement during a Smith-Purcell experiment at 55 MeV.

During the experiments, the neutron target used for neutron production was replaced by an aluminium block working as a Faraday cup. Measuring the current at the beginning and at the end of the beam line, information about the current losses was obtained helping to adjust the electron beam trajectory.

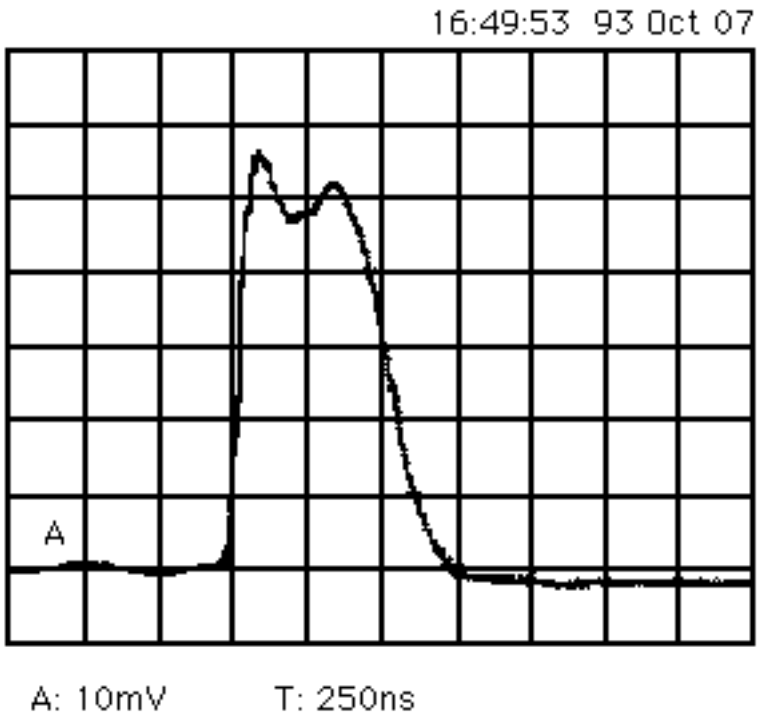


**FIGURE 4.5 : Pulse shape of a 55 MeV electron beam measured with a fast ferrite.**

## 4.4 Energy measurements using a magnetic deflection

A calibrated magnet has been installed at the exit of the accelerator. Coupled with a Faraday cup, it constitutes a magnetic energy analyser. The current injected into the magnet in order to deviate the electron beam to the detector is proportional to the electron beam energy [70]. This system gives also information on the electron energy dispersion. During an energy measurement, which takes about one minute to be completed, the electron beam is not available for the experiment.

Figure 4.6 shows a typical energy spectrum of an electron beam used for Smith-Purcell experiments. The electron beam energy is 85 MeV with a dispersion of 6 MeV (FWHM). The energy could be tuned between 20 MeV and 110 MeV.

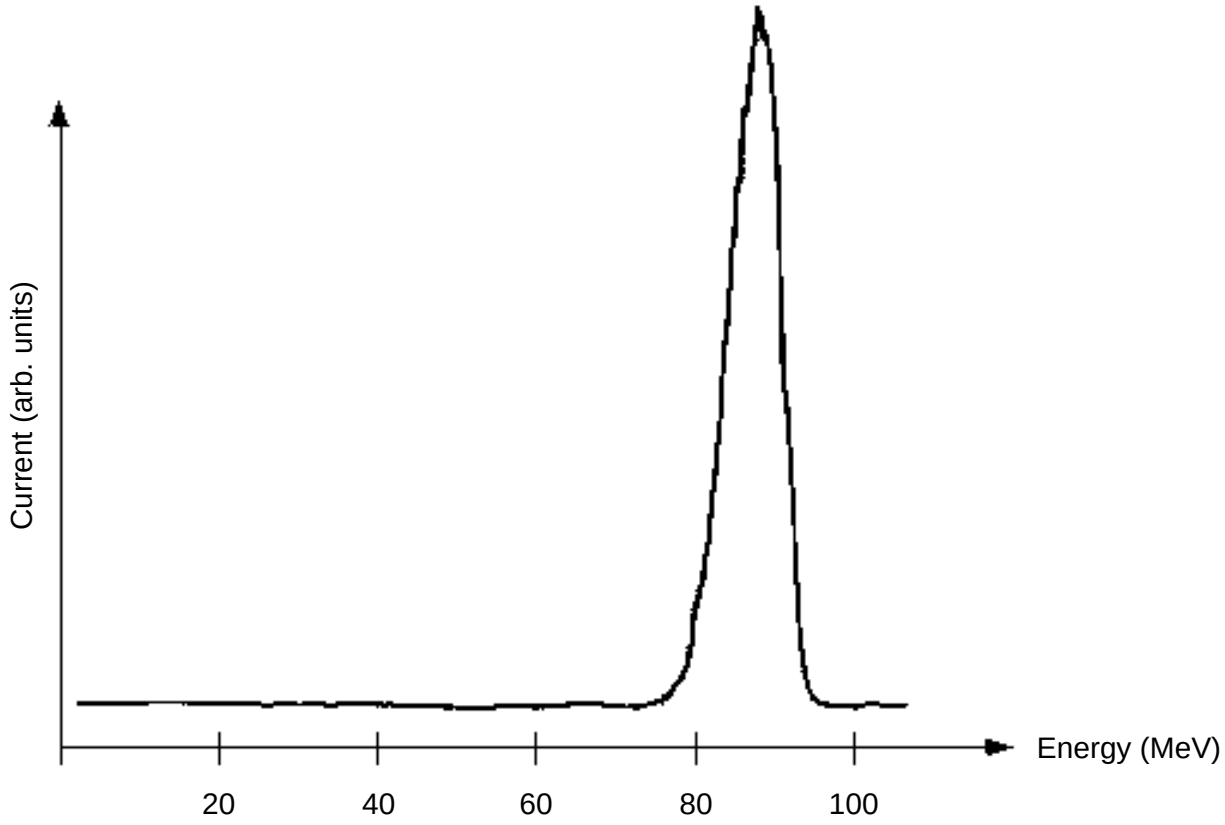


**FIGURE 4.6 : Energy spectrum of a 85 MeV electron beam used for Smith-Purcell experiments.**

## 4.5 The OTR diagnostic tool

Transition radiation is emitted when a charged particle crosses the interface between two media of different dielectric constants. It was predicted by Frank and Ginzburg in 1945 [10] and has been thoroughly studied from theoretical and experimental points of view. The spectral and angular distribution and the degree of polarisation of the radiation are related to the energy and the incidence angle of the electron and are useful for charged particles beam diagnostic. After the pioneering work of L.Wartski [11] numerous diagnostic tools in particle accelerators [71] have been developed.

At the GELINA accelerator such a beam diagnostic has been installed and gives on-line information on the beam parameters [72]: the energy, the size and the divergence of the beam are measured.

When a highly relativistic ($\gamma >> 1$) electron hits a metallic foil the angular distribution of OTR is given by [11]:

$$\frac{d^2W}{d\omega d\Omega} = F(\phi, \theta, \omega) \cdot \frac{e^2}{\pi^2 c} \cdot \frac{\theta^2}{(\gamma^{-2} + \theta^2)^2} \qquad (4.1)$$

where $F(\varphi, \theta, \omega)$ is the Fresnel coefficient of the foil surface. The geometry is depicted in Fig. 4.7. This radiation is highly directional, close to the specular reflection, with a maximum of intensity at $\theta = 1/\gamma$. For an electron beam of finite divergence the distribution is given by the convolution of ( 4.1 ) with the beam divergence.

Focusing a camera on the foil surface, it is possible to measure the current density distribution, i.e. the beam profile. For a perfectly conducting surface, $F(\varphi, \theta, \omega) = 1$ and the radiation pattern is circular symmetric around the direction of the specular reflection with radial polarization. Therefore no polarisation is measured when focusing at specular reflection on the foil for a non divergent beam [11]. When the camera is focused at infinity, the OTR angular distribution is measured, from which information about the electron energy and the beam divergence is obtained [11][72]. At GELINA an optical bench with two cameras is installed, which allows to carry out both measurements simultaneously: a semi-transparent mirror divides the OTR beam, allowing to focus one camera on the beam spot and the second camera on the angular distribution (see Fig. 4.8).

Due to the high radiation level in the target hall the observation of OTR is made in a separate room 8 meters away from the OTR chamber through a 12 cm diameter hole in the concrete shielding. This requires the installation of an appropriate optical bench. At GELINA the total length of the optical bench is 9 m with a maximum angular aperture at the entrance of 30 mrad, corresponding to $6/\gamma$ for a 100 MeV electron beam. In order to align the optical bench a laser was installed in the target hall to simulate the OTR beam. The positions of the lenses and the mirror were adjusted in such a way that the laser beam was transported to the position of the cameras. A correct alignment was obtained when the first camera could see the OTR foil while simultaneously the second camera was able to see the thermal cathode of the accelerator, which is some 20 m far away from the OTR foil and simulates a source at infinity.

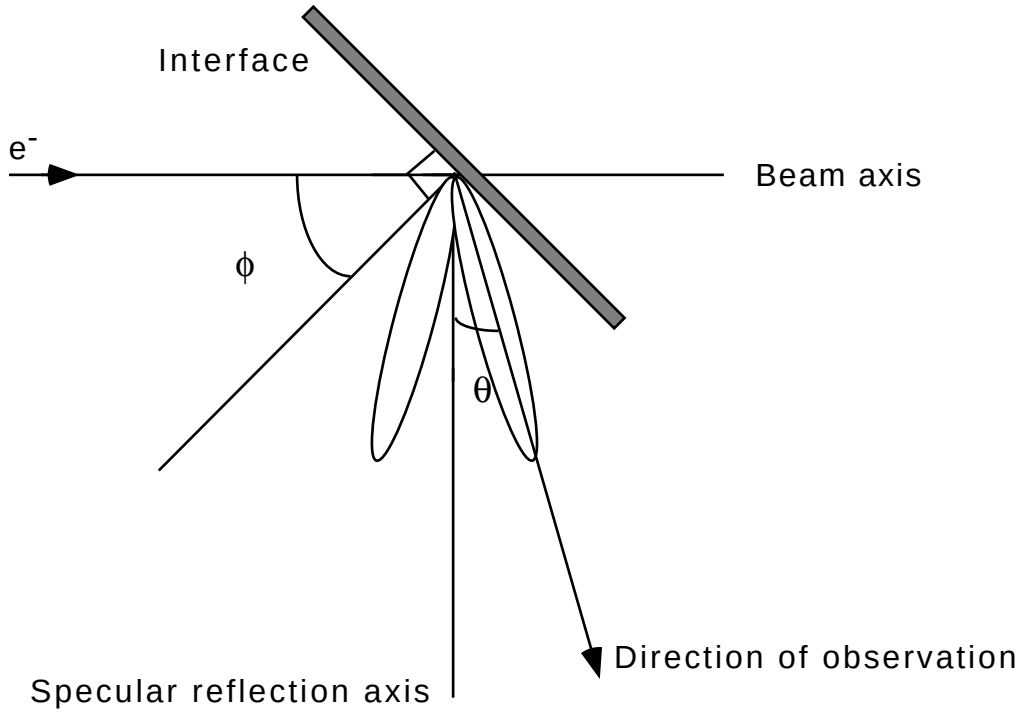


**FIGURE 4.7 : Geometry for observation of OTR.**

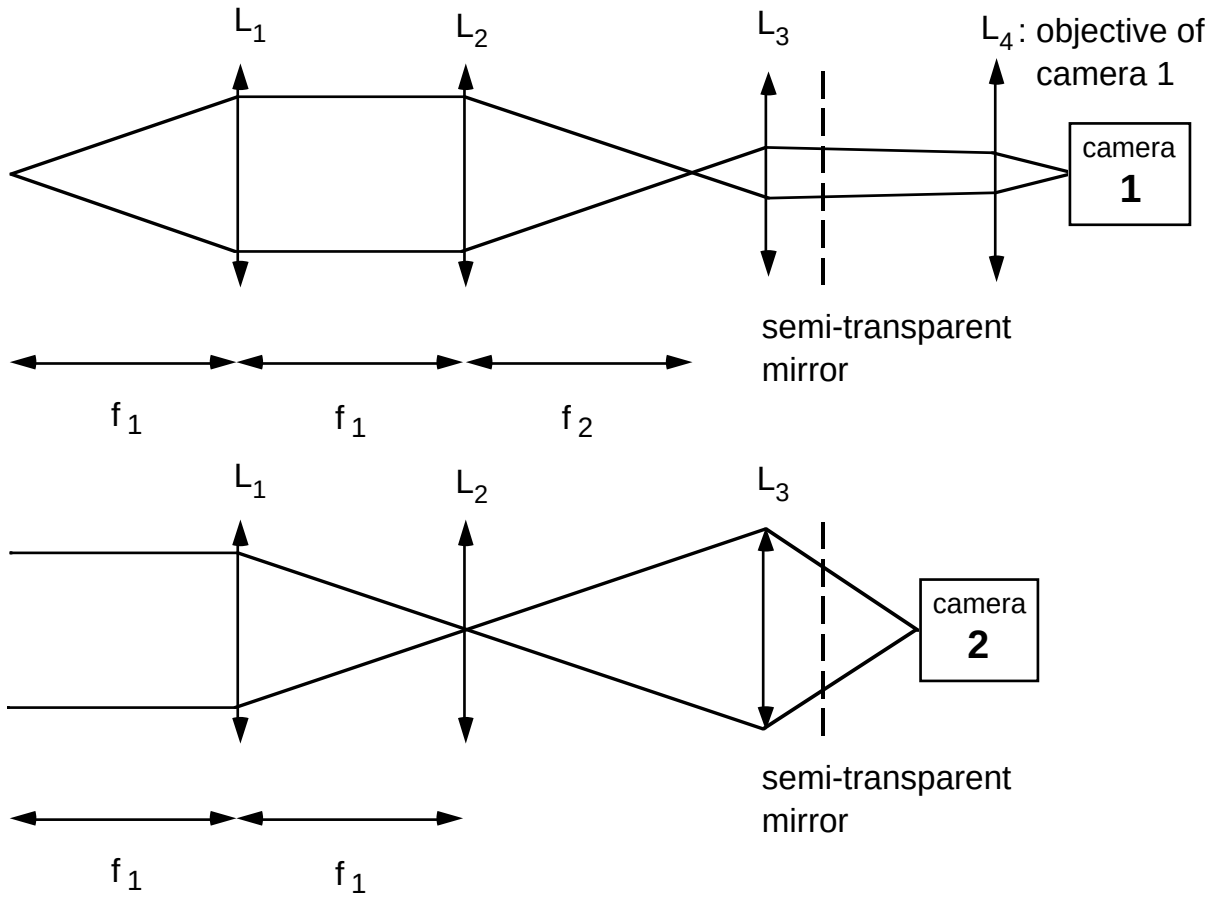


**FIGURE 4.8 : OTR optical bench set-up for focusing at infinity or on the source.**

The calibration of camera 1, used to measure the beamshape, was done inserting a calibrated frame at the position of the radiator. For the calibration of camera 2, used to measure the angular distribution, a picture of a diffraction pattern from a small rectangular grid was used. The resolution was of the order of 1/10 mm for the size and 1/10 mrad for the divergence. Figure 4.9 shows two typical pictures used for the calibration.

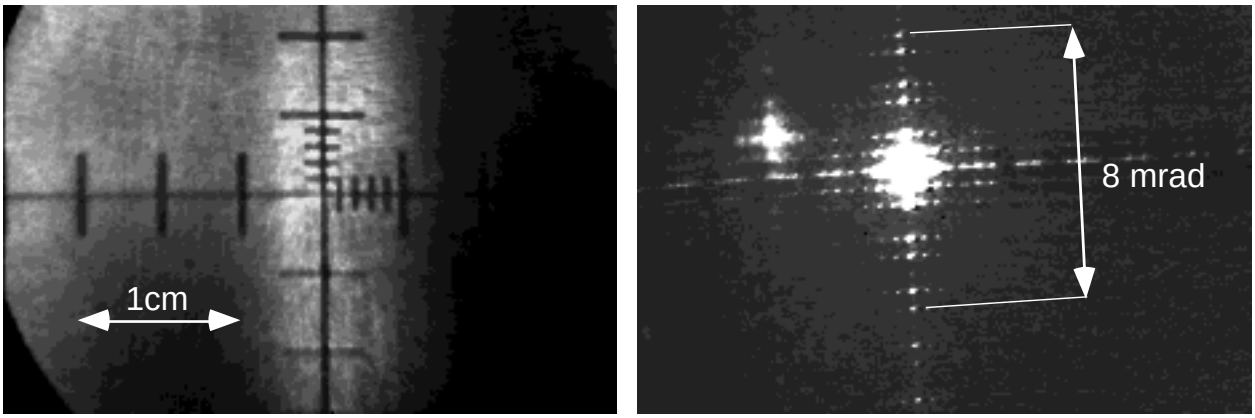


**FIGURE 4.9 : Calibration of the OTR diagnostic system.**

The images from the two cameras were digitized and stored in a Macintosh computer. Fig. 4.10 shows a layout of the OTR diagnostic system. The best way to extract the characteristics of the electron beam out of the observed images would be to fit a calculated OTR angular distribution including parameters such as the energy and the electron beam divergences $\sigma_x$ and $\sigma_y$ to the measured angular distribution. Such a procedure is however time consuming. For on-line diagnostics an estimate of the divergence (reliable within 10%) can be obtained much faster from the contrast $I_{max}/I_{min}$ in the angular distribution [73] On-line analysis was possible using the OTR4.0 application program, a dedicated software written to extract the electron beam parameters from the picture of the beam and of the angular distribution [74]. Fig. 4.11 shows the front panel of OTR4.0. The top-row images belong to the electron beam shape; the bottom-row images belong to the angular distribution. Information about the electron energy, and the size and divergence of the beam are given.

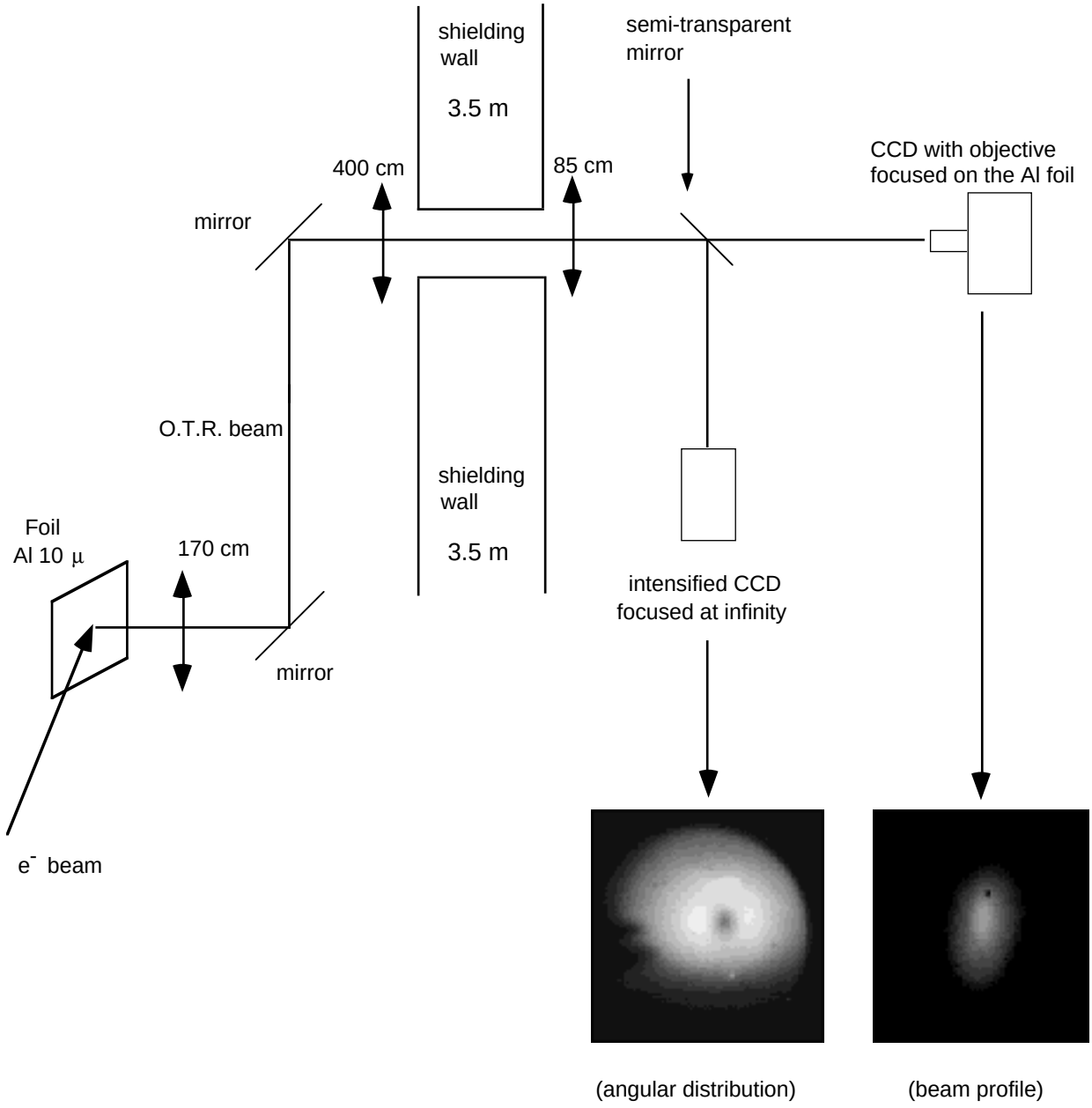


**FIGURE 4.10 : The GELINA OTR diagnostic tool (not drawn to scale).**

During the experiments, the divergence of the beam was usually below 5 mrad (FWHM). For electrons above 50 MeV the beam diameter was of the order of 5 mm (FWHM), increasing up to about 10 mm at lower energies.

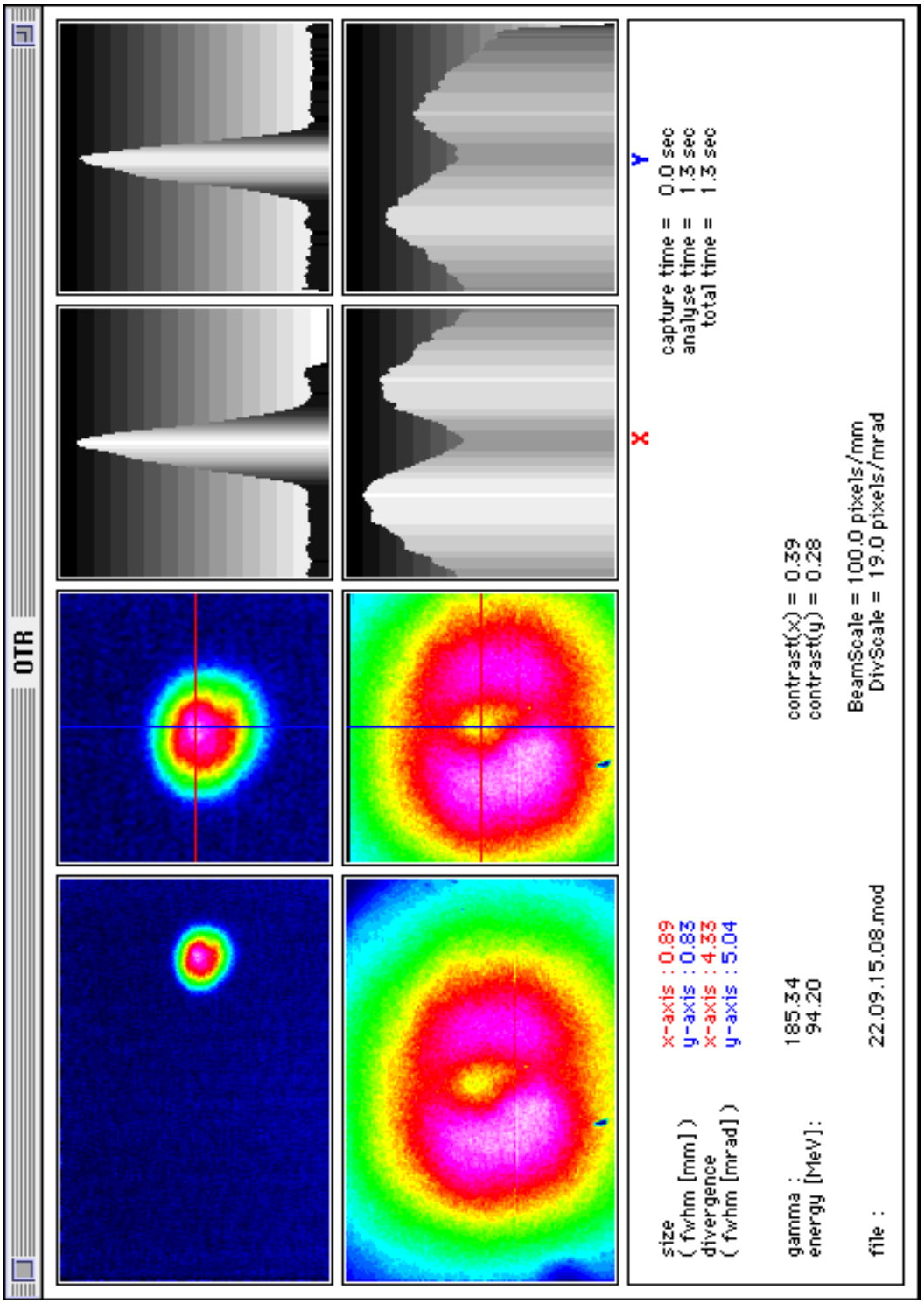


**FIGURE 4.11 : An OTR analysis of a 94 MeV electron beam using the OTR4.0 application program. The pictures are displayed in false colors.**

# CHAPTER 5 Smith-Purcell experiments at GELINA

Three experiments with relativistic electrons interacting with optical gratings were carried out using the GELINA facility during September 1993 and January and May 1994. The experimental set-up and the results of the measurements carried out during these experiments are presented now.

## 5.1 Experimental set-up

### 5.1.1 Insertion devices

Remote controlled insertion devices were used. They work as one-axis goniometers with 360° rotation range. The long translation course permits to insert several radiators like OTR foils, gratings, Cherenkov radiators. The power supplies for the stepping motors are driven by an interface linked to a Macintosh computer. A program to drive the insertion device has been written using the LabVIEW software [74][75]. A user friendly interface permits to send the commands to the motor interface to properly position the radiator in the beam. Fig. 5.1 shows the front panel of the program.

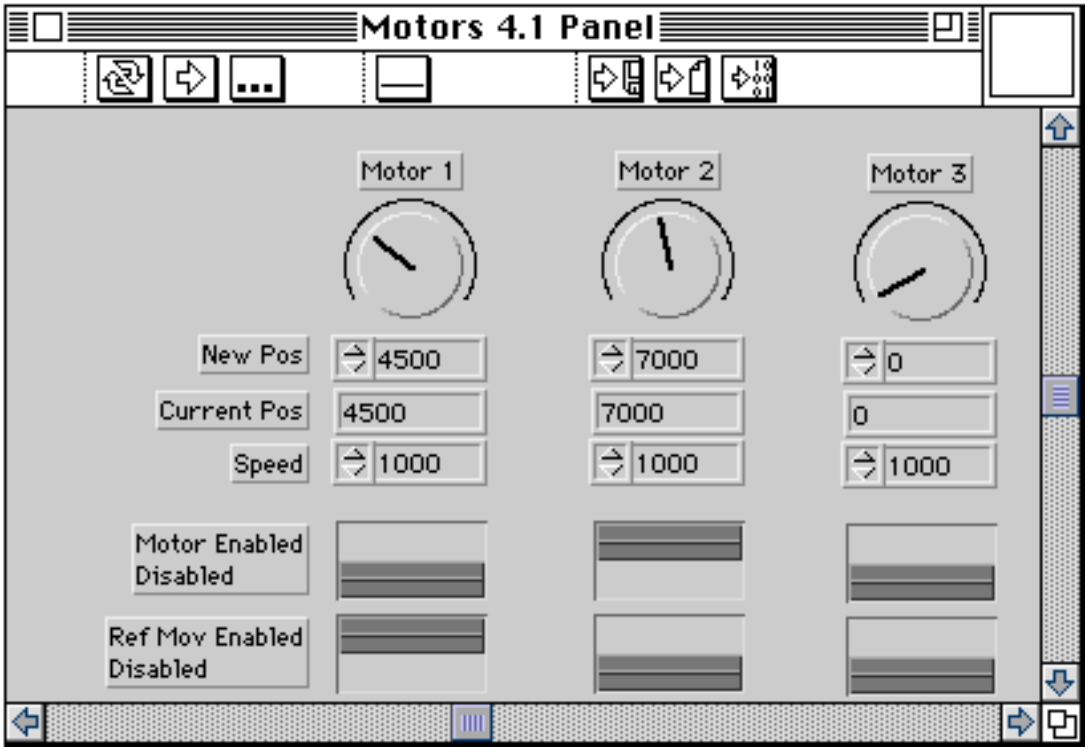


**FIGURE 5.1 : The front panel of the Motor program used to drive the remote controlled insertion devices. The program can drive up to three motors simultaneously.**

Figure 5.2 shows a drawing of the insertion device, vertically mounted on the OTR radiation chamber. A second device was mounted horizontally. The reproducibility of the movements was better than 0.5 mm in translation and 0.1° in rotation.

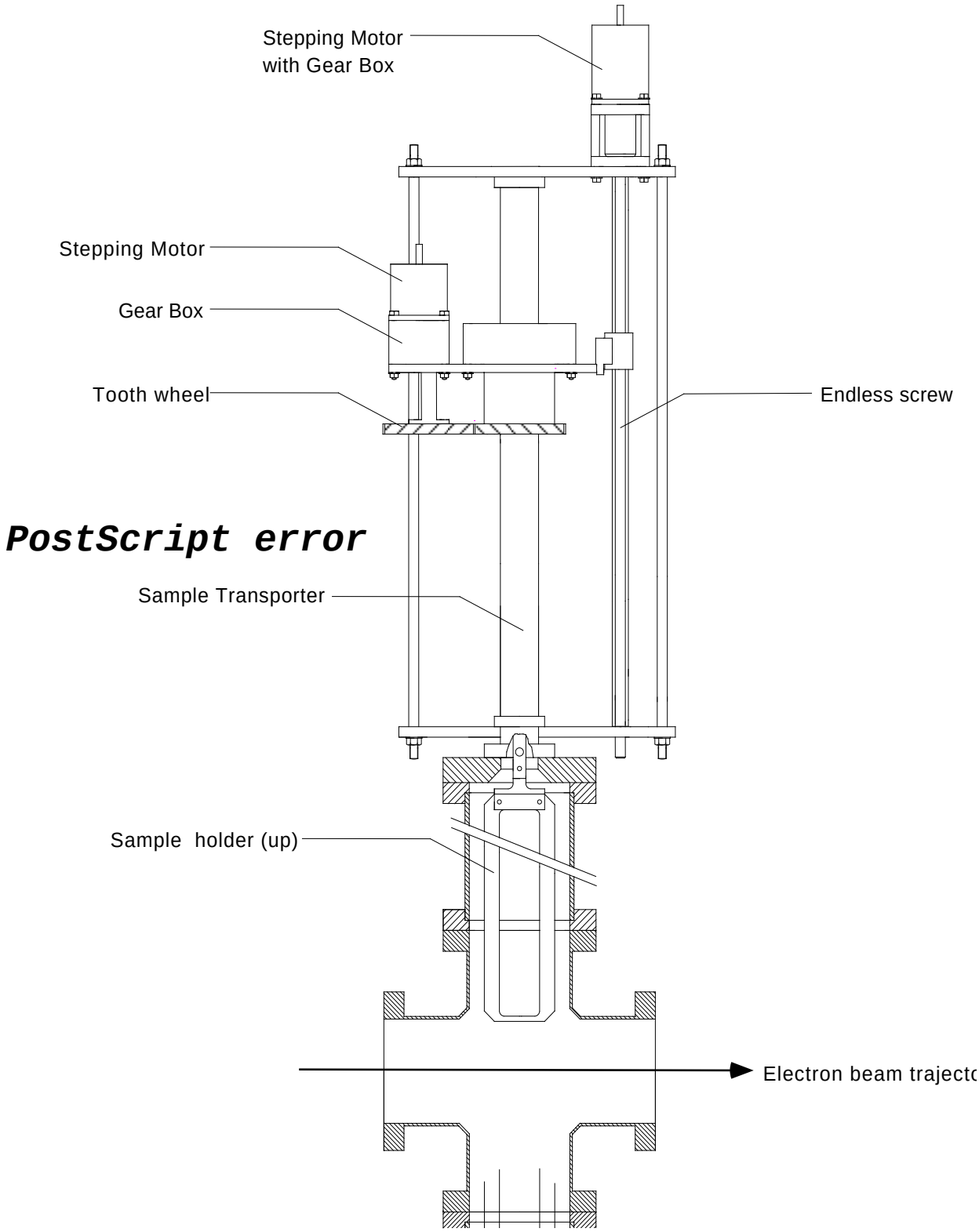


**FIGURE 5.2 : Scheme of a motorized insertion device, mounted on a vacuum chamber.**

## 5.1.2 Target holders

Figure 5.4 shows drawings of the grating holders used in the Smith-Purcell experiments. A vertical insertion device with grating holder 1 was used for Smith-Purcell and OTR measurements. Two OTR foils could be mounted on the frame. A glass grating with triangular profile was used. The grating was protected against the bulk part of the electron beam by a 2 cm thick molybdenum shielding. A glass plate with the same dimensions as the grating was used to estimate the contribution of Cherenkov radiation produced when the electrons hit the grating. The vertical rotation axis of the device coincides with the grating grooves to permit an angular adjustment between the electron beam and the grating surface. See Fig. 5.3 (a) for the geometry of the first experiment.

A second insertion device was installed horizontally supporting grating holder 2. This second experiment was designed to measure the wavelength and the polarization of the Smith-Purcell radiation produced when electrons are passing at a finite angle with respect to the grating rulings. A glass grating with sinusoidal profile was used, with its surface being perpendicular to the horizontal rotation axis. In this case, a precise, low-range angular alignment of the electron beam with respect to the grating surface was obtained by adjusting the beam trajectory. See Fig. 5.3 (b) for the geometry of the second experiment.

A third experiment with similar geometry as in experiment 1 was carried out, but using a SiC grating. A grating holder similar to grating holder 1 was used, with two OTR foils and a 2 cm thick molybdenum shielding for the grating.

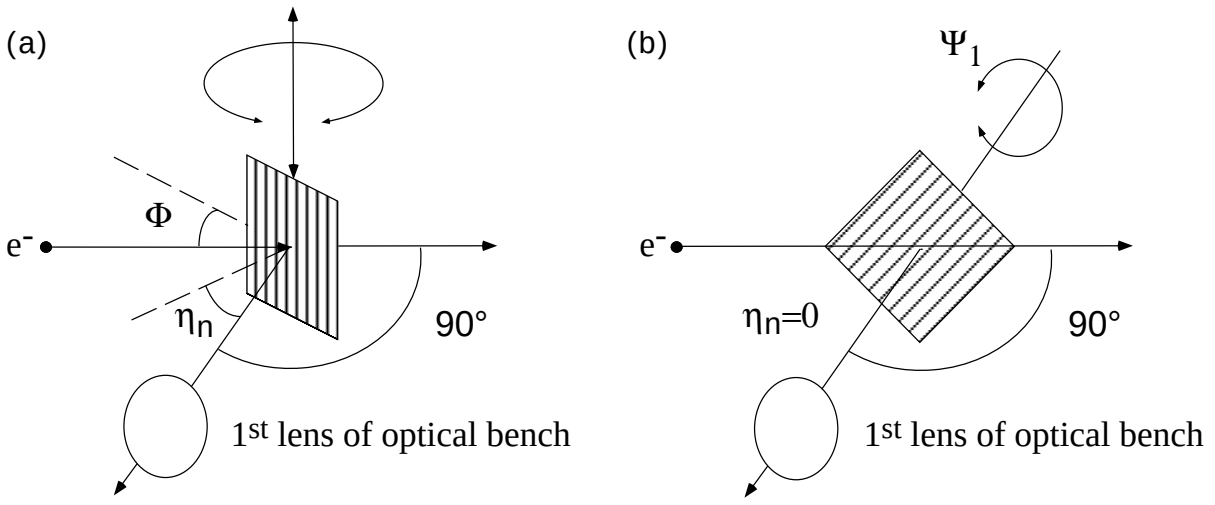


Experiment with an insertion device mounted vertically and grating holder 1

Experiment with an insertion device mounted horizontally and grating holder 2

**FIGURE 5.3 : Principle of the two types of Smith-Purcell experiments.**

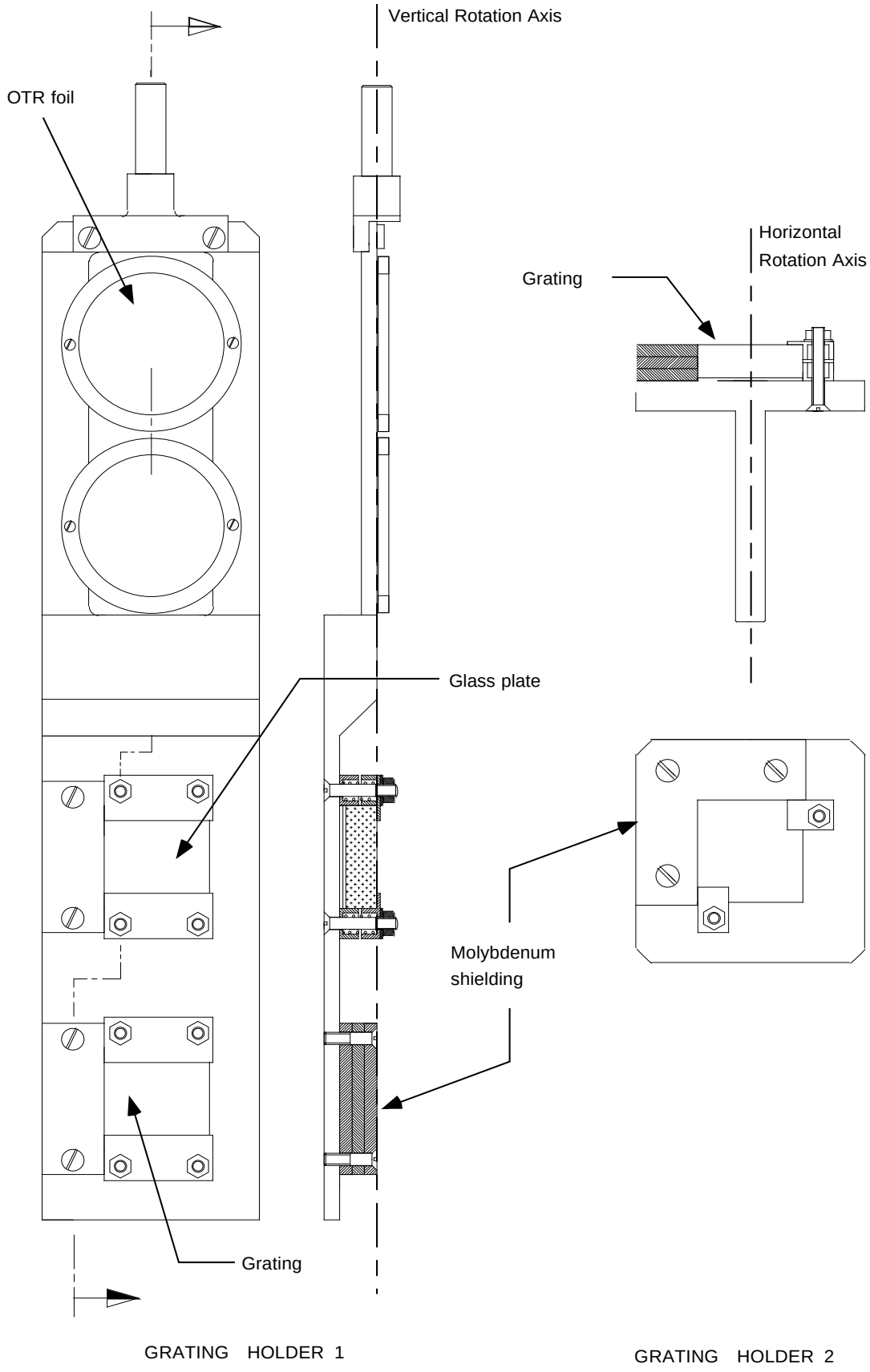


**FIGURE 5.4 : Drawings of the target holders used for Smith-Purcell experiments.**

### 5.1.3 Gratings

In the first two experiments, commercial gratings with 1800 lines/mm on a 36 x36 $mm^2$ glass substrate were used [76]. They had a sinusoidal profile and an echelette profile with blazing angle of 26°45', respectively. These gratings were replicas of master gratings.

Ruled master gratings are produced by evaporating an Al coating onto a highly polished substrate. The grooves are ruled using a diamond tool with the desired angle apex. The mechanical set-up is of vital importance to obtain absolutely straight, parallel and equidistant rulings. With this process, only piecewise linear grating profile can be produced (e.g. triangular or trapezoidal gratings) and the production of such a master grating is a very time-consuming process. Fig. 5.5 shows the principle of production of a mechanically ruled grating.

Holographic master gratings are produced in a different way. A highly polished substrate is coated with a layer of photosensitive material and exposed to an interference pattern created at the intersection of two coherent laser beams. Chemical treatment of the photosensitive layer selectively dissolves the exposed areas producing the grooves. The interfering waves determine the profile of the grating, which can be either sinusoidal, lamellar or triangular. An evaporated metal coating is deposited on the surface to provide high efficiency. Holographic recorded gratings are of very high quality. The interference pattern recording technique leads to a perfect periodicity with minimal grooves errors. Such gratings can be produced with a very high groove density up to 6000 lines/mm and on very large substrates. Figure 5.6 shows the principal steps in the production of a master holographic grating.

Once a master grating has been manufactured it can be replicated to produce copies of the original. A highly polished blank is coated with an epoxy layer and sandwiched together with the master. When the epoxy is cured, the master grating is separated from the replica. The epoxy layer is then an exact copy of the master grating, which can be used again for another replication process. Figure 5.7 shows the process of replicating a master grating.

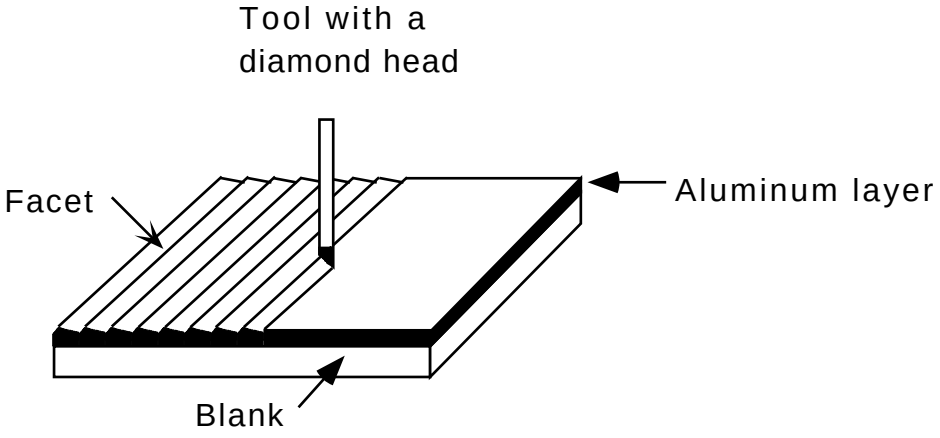


**FIGURE 5.5 : The principle of production of a mechanically ruled master echelette grating.**

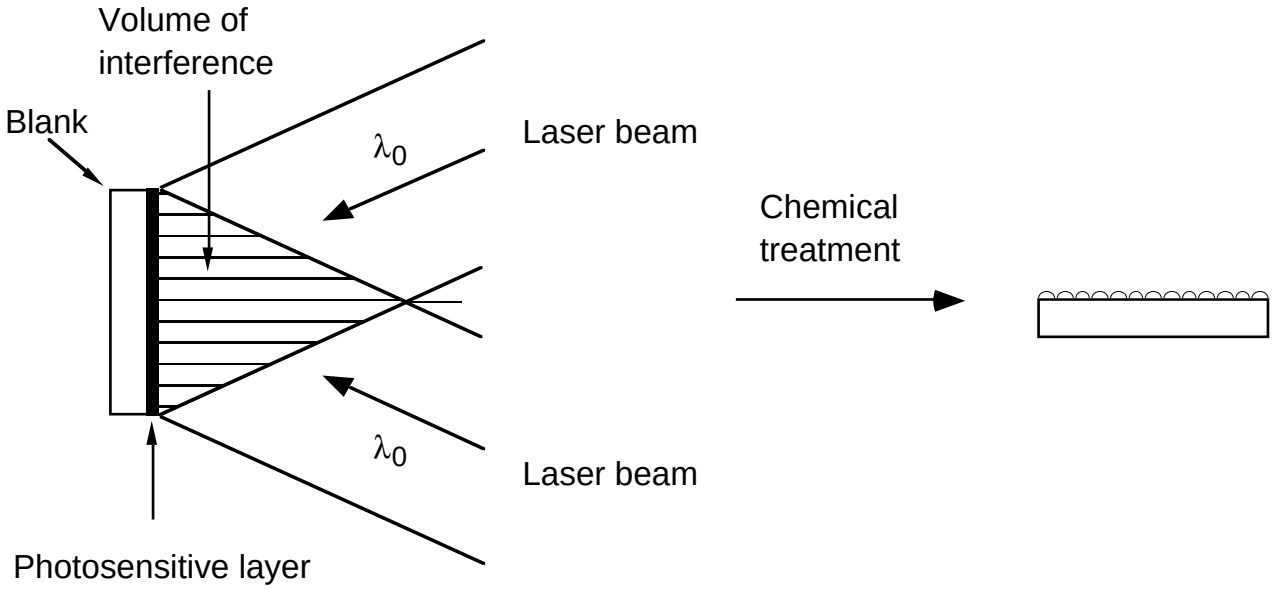


**FIGURE 5.6 : The principle of production of a master holographic grating.**

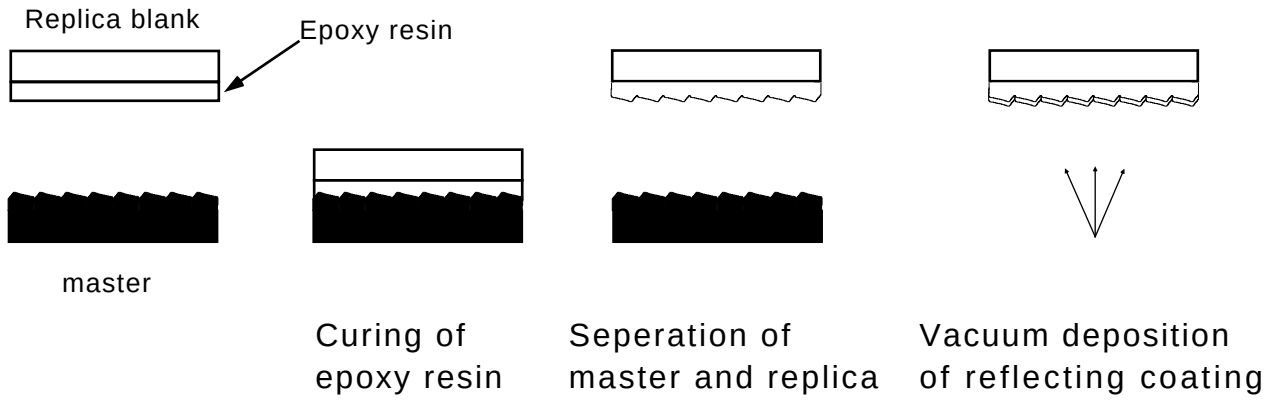


**FIGURE 5.7 : The principle of production of a replica grating.**

The replica grating consists of a substrate, an epoxy layer and a reflecting coating, which makes it unsuitable for use in ultra high vacuum. The risk of thermal damage is also quite important. In a Smith-Purcell experiment, it is difficult to avoid electrons hitting the surface of the grating, due to the finite emittance of the electron beam. The possible damage induced by such electrons decelerated in the grating would limit the life-time of the grating. The very thin layer of reflective material (mostly aluminium) deposited on the surface of the grating can easily be evaporated. The material of the substrate is also of great importance. Most of the standard gratings are made out of glass (BK 7), which is highly fragile. For all this reasons, special precautions have to be taken when handling the grating in an electron beam.

Figures 5.8 and 5.9 show pictures of the surfaces of the sinusoidal and the ruled gratings before use in the Smith-Purcell experiments, obtained with a scanning electron microscope. The two grating surfaces are not free from defects and small particles of dust are deposited on the surfaces.

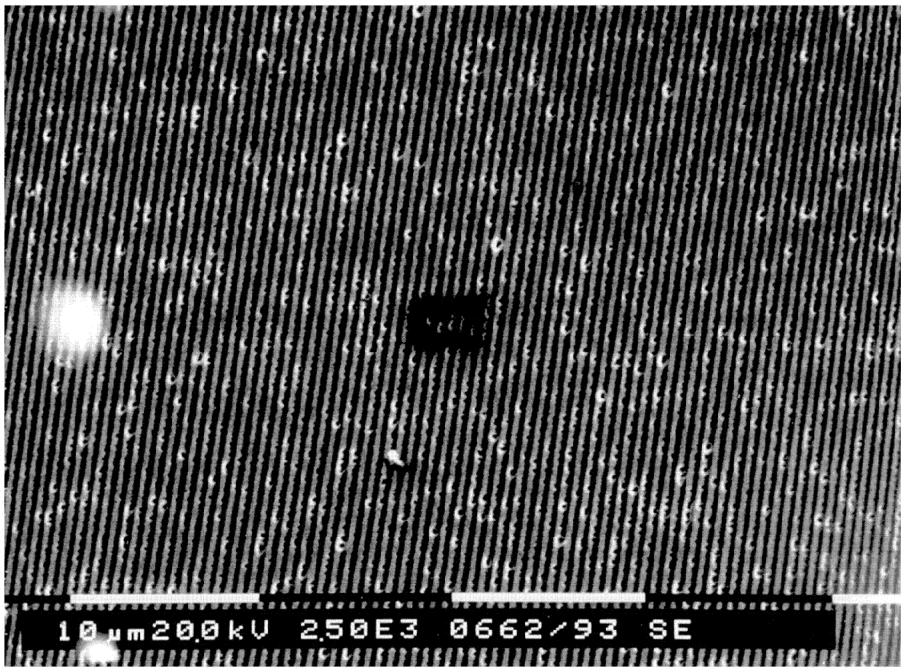


**FIGURE 5.8 : A picture of the 1800 l/mm sinusoidal profile Jobin-Yvon grating before the Smith-Purcell experiments.**

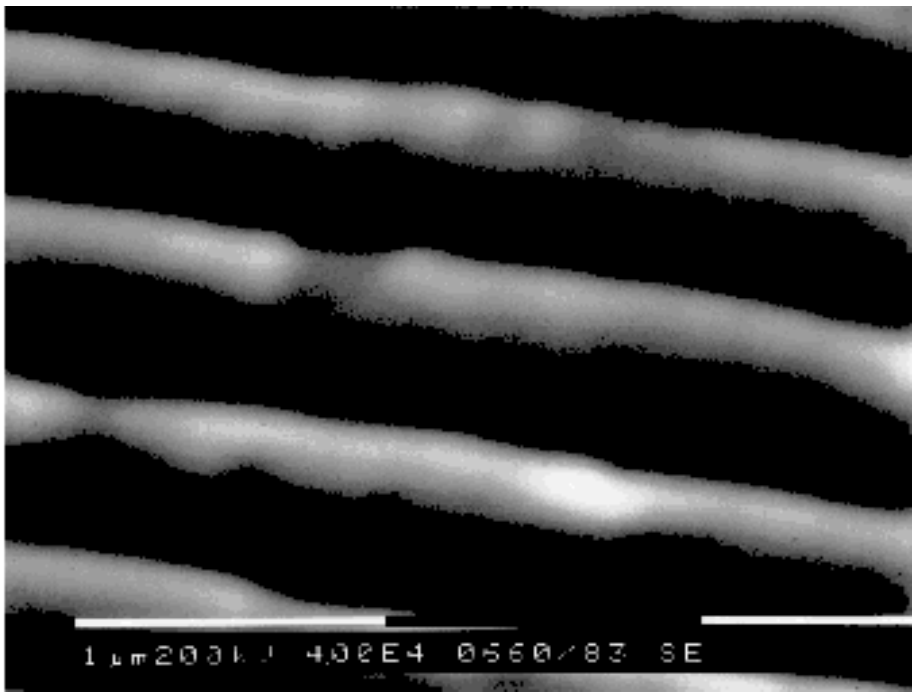


**FIGURE 5.9 : A picture of the 1800 l/mm blazed Jobin-Yvon grating before the Smith-Purcell experiments.**

The third experiment was carried out using a 50 x 50 $mm^2$ grating, ruled in a 100 μm SiC layer deposited on a 10 mm thick graphite block [77]. The grating was produced with the ion beam etching process: the surface profile of a holographic recorded photoresist film grating is transferred onto the grating substrate. An ion etching machine is used to ablate surface atoms through the registered holographic mask. The technique allows to replicate a given groove profile with nanometer accuracy. Figure 5.10 shows the steps of the production of a lamellar ion etched grating

The flat surface of 50 x 50 $mm^2$was divided into two parts. The first half was not etched and used as a plane mirror for OTR measurements (part c). The second part was etched to give a lamellar profile with parameters h/D=0.1 and a/D=0.5. During the fabrication process a defect in the etching facility produced a fault in the lamellar profile resulting in rounded upper parts. Half of this part of the surface was left in this shape (part a) and the second half was etched again to give a triangular upper part (part b). The radiator was then aluminized. Figs. 5.12 describes the grating profiles.

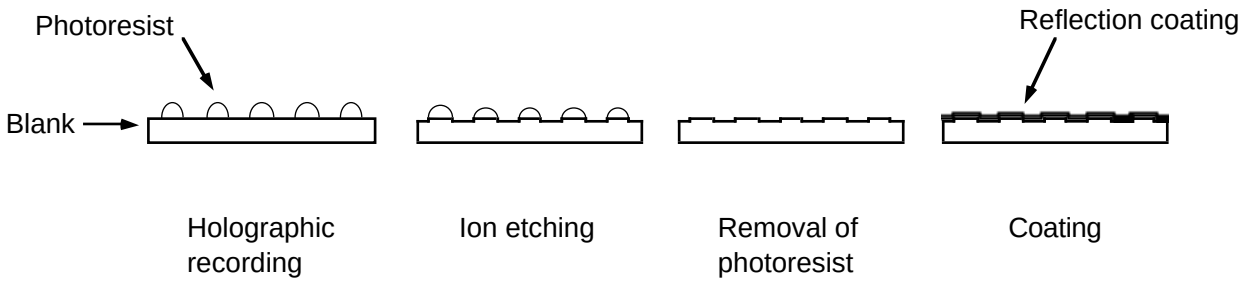


**FIGURE 5.10 : Principle of production of an ion etched grating.**

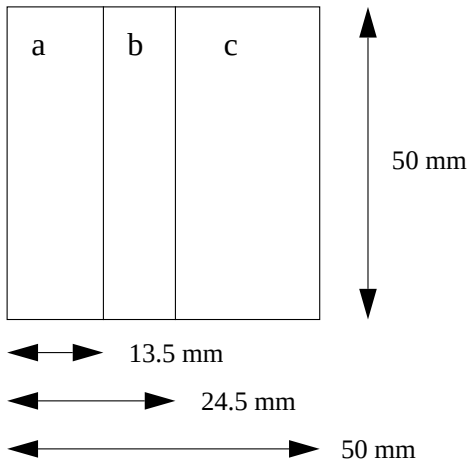


**FIGURE 5.11 : The custom SiC Zeiss radiator used for Smith-Purcell and OTR experiments.**

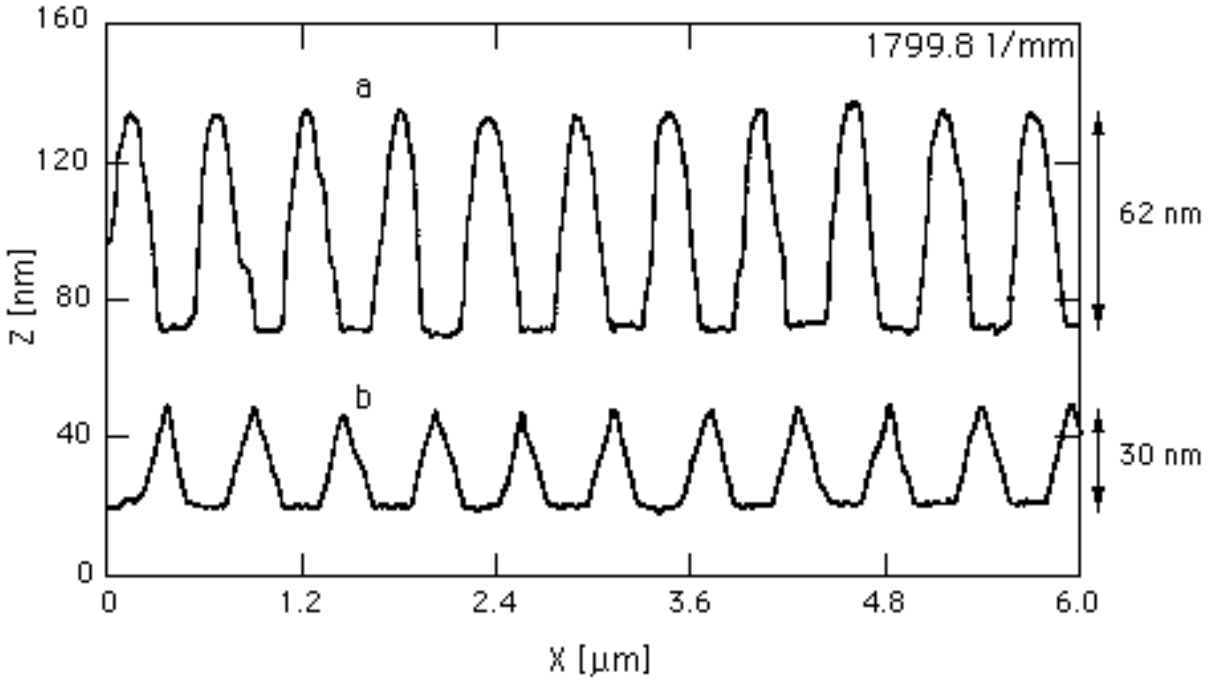


**FIGURE 5.12 : Profiles of the ion-etched gratings on the surface of the SiC radiator.**

### 5.1.4 Optical bench and data acquisition

The Smith-Purcell radiation produced at the GELINA accelerator was rather low in intensity. This was due to the very low beam current used in order to avoid damage to the grating and because only very few electrons really interact, due to the large size of the beam (some millimeters to be compared with the interaction height of the order of 10 µm). In order to be able to detect and characterize the radiation the OTR optical bench had to be modified. Only the intensified camera was installed. A removable objective-lens allowed to focus either at infinity to measure the OTR angular distribution (without objective) or to the target (grating, Sic mirror or OTR foil) to capture a picture of the source. Figure 5.13 describes the new optical bench.

The intensified camera was a low-level camera LH4036-25 from Lhesa Electronique. The detection block is an analyser tube type SIT 25 mm from Thomson Electronics with a S20 ER photocathode [78]. Each photoelectron produced by the photocathode is accelerated up to 10 keV and loses its energy in the silicon of the CCD where it creates by ionization 1500 to 2000 electron-hole pairs. The typical sensitivity is $5.10^{-4}$ lux on the photocathode and the typical spectral response extends from 400 to 900 nm. Figure 5.14 gives the typical spectral response of the photocathode [78]. The spectral response is large for the visible (400-800 nm) with a maximum near 550 nm (green) and decreases very fast in the near-infrared range ($\lambda$>800 nm).

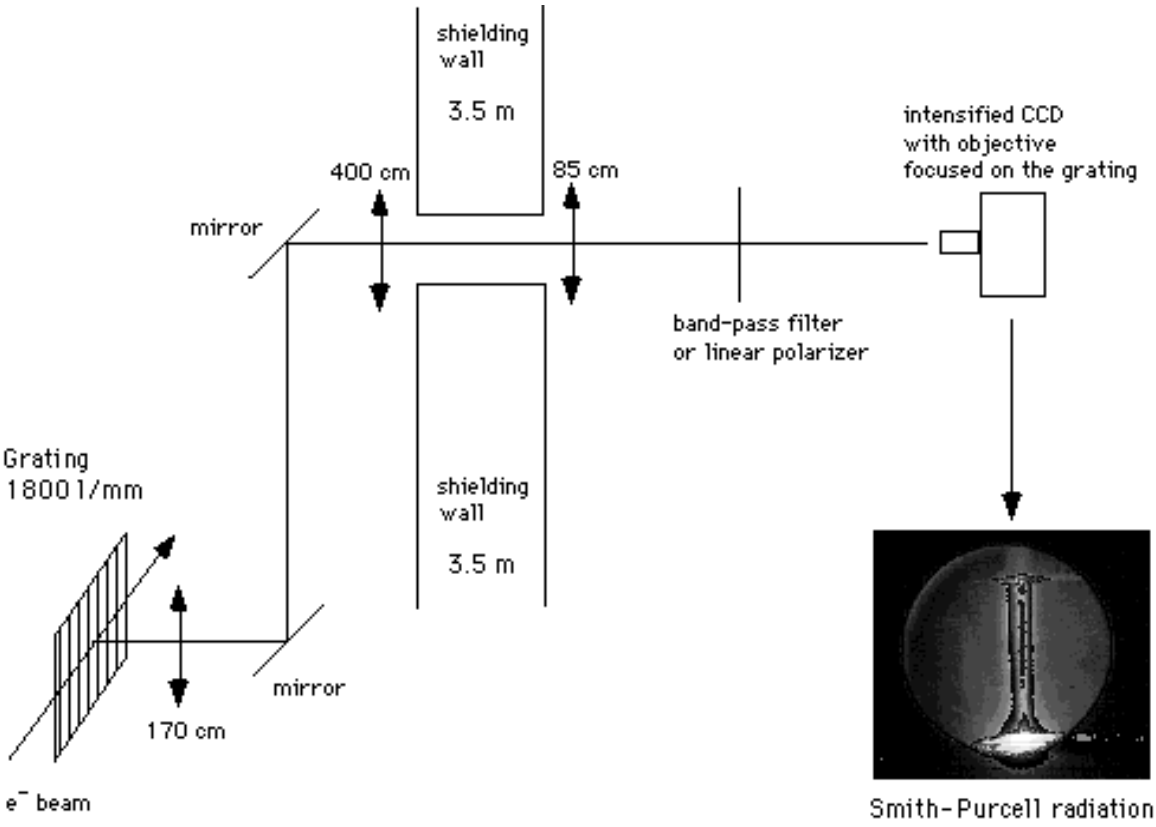


**FIGURE 5.13 : The optical bench used for the Smith-Purcell experiments.**

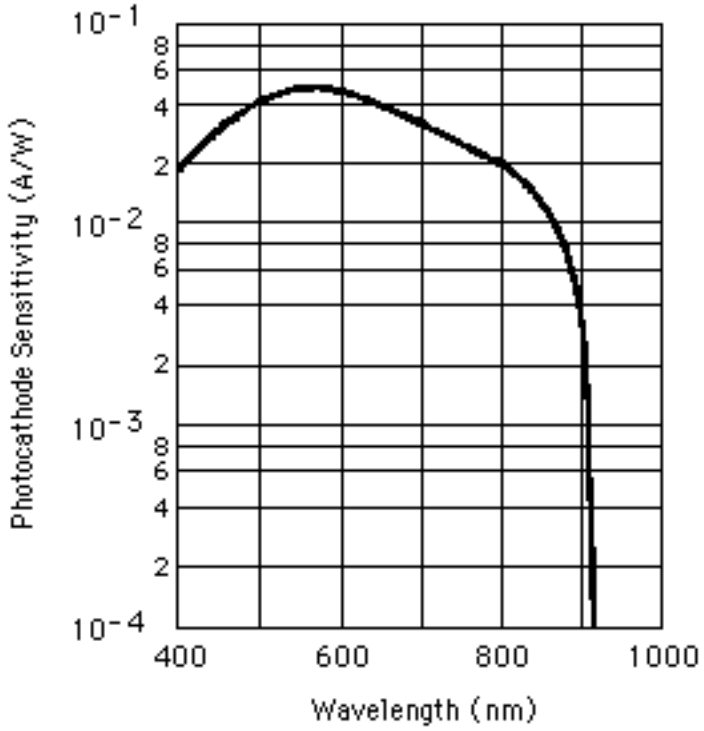


**FIGURE 5.14 : Spectral response of the photocathode of the intensified CCD camera.**

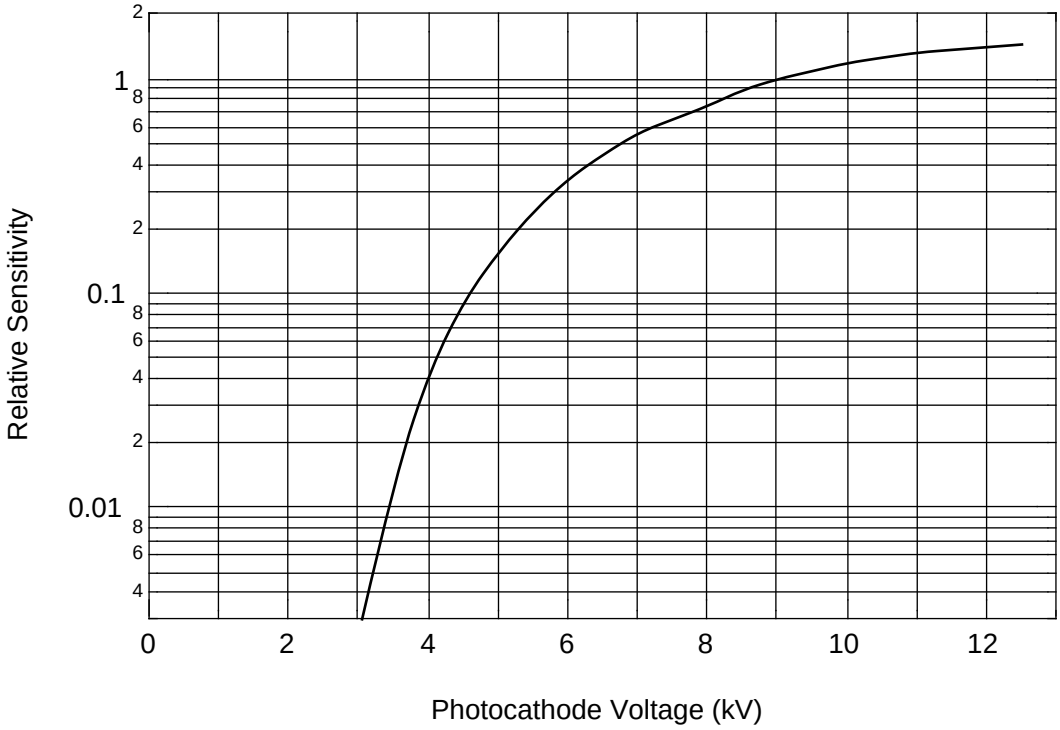


**FIGURE 5.15 : Relative sensitivity of the CCD intensified camera versus the photocathode voltage.**

The sensitivity of the camera could be adjusted by varying the voltage of the photocathode. Fig. 5.15 shows the sensitivity curve [78]. It varies slowly above 6 kV, but very fast for lower voltage.

In order to get reliable relative measurements, the camera was operated always at full sensitivity and calibrated gray filters in front of the camera were used to reduce the intensity. These filters are made out of a metallic alloy coating vacuum-deposited on an optical-quality glass (BK7) substrate and provide flat spectral density curves over a large spectral range for moderate optical densities [79]. Figure 5.16 shows the optical density curves characterizing these gray filters.

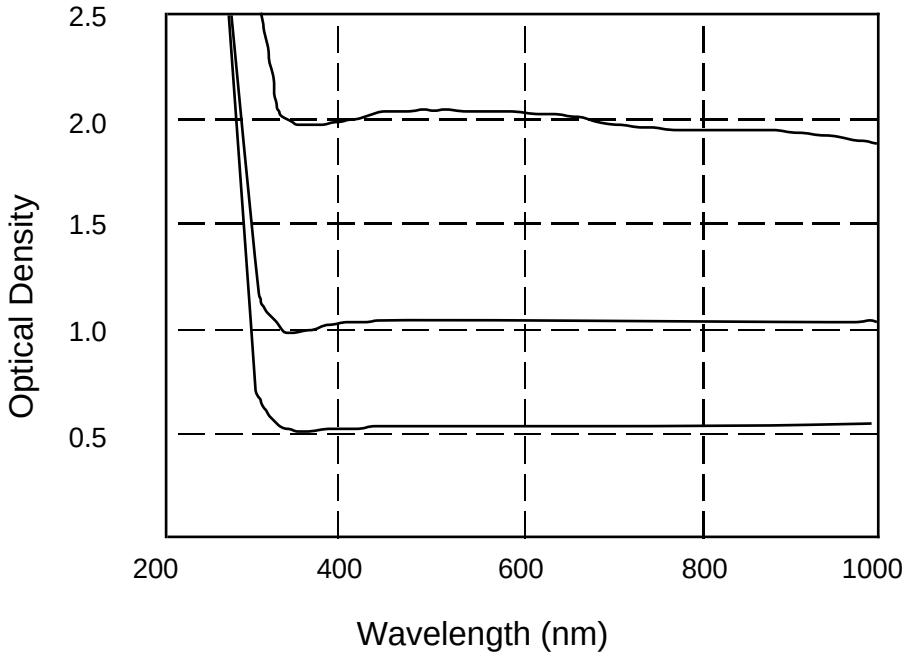


**FIGURE 5.16 : Density curves of the neutral gray filters.**

A set of calibrated interference filters operating with the same principle as the Fabry-Perot interferometer was used to characterize the spectral distribution of the emitted light. The filters cover the visible spectrum from 400 to 700 nm in 50 nm steps. The bandwidth of the filters is 10 nm [79]. Figure 5.17 shows the transmission of the interferometric filters.

A dichroic sheet linear polarizer was used to measure the polarization of the emitted radiation. It is made of a polymeric plastic, the molecules of which are oriented by stretching thereby achieving birefringence. Pigment molecules are selectively attached to the polymer, leading to strong absorption of one of the two orthogonal states of polarization.

The image acquisition was done using a Macintosh IIfx computer equipped with a Data Translation QuickCapture frame grabber. The Image software was used for image acquisition and treatment. Image is a public domain program for the Macintosh for digital image processing and analysis. It is fully compatible with other Macintosh applications and supports many standard image processing functions, like histogram equalization, contrast enhancement, density profiling, smoothing, sharpening, etc... The images can be shading-corrected and frame-averaged. Image also incorporates a Pascal-like macro programming language, providing the ability to automate complex, and frequently repetitive, processing tasks. It supports the Data Translation QuickCapture card for digitizing images using a TV camera.

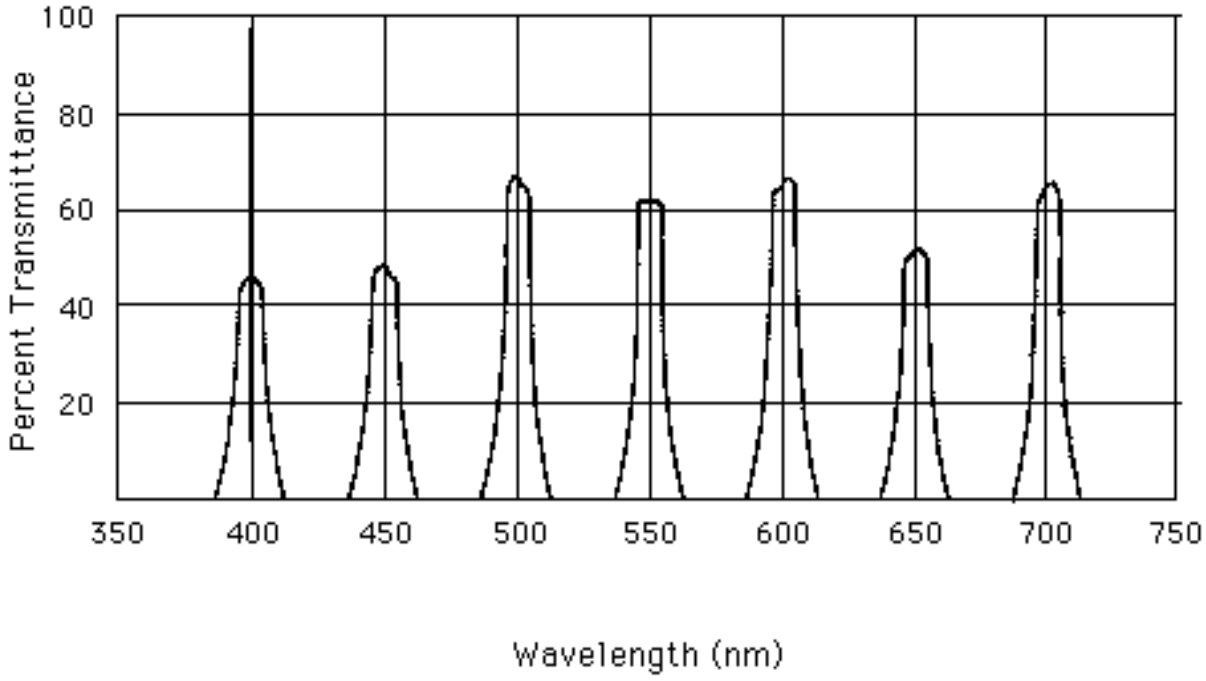


**FIGURE 5.17 : Transmission curves of the 10 nm bandwidth interferometric filters.**

## 5.2 First experiment: vertical insertion device and blazed grating

The first experiment was done using a vertical insertion device equipped with target holder 1 on which several radiators were installed. Two OTR foils were used to measure the shape and the position of the beam.

The blazed grating with 1800 l/mm described previously was used for the Smith-Purcell measurement. As the substrate of this grating is made out of glass the contribution of Cherenkov radiation produced by electrons hitting the grating could not be avoided. In order to discriminate these two effects, a glass plate with same dimension as the grating was installed on the target holder and used in the same conditions as the grating.

Figure 5.18 shows a typical picture of the radiation produced by electrons of about 100 MeV interacting with the blazed grating and observed with the intensified camera, without polarizer and without filter. The observation angle is 90° with respect to beam direction and the direction of the electron beam is from top to bottom.

The electron beam and the grating were positioned in such a way that a homogeneous distribution of light along the grating surface was observed. This was not obtained when the electron beam was coming parallel to the grating surface, but at a small angle of incidence of 6.5°. Therefore, the emitted radiation was not pure Smith-Purcell radiation. Bachheimer [20] studied the case of almost parallel electrons of some 100 keV interacting with optical gratings and has shown that the characteristics of the emitted light were very similar to those of pure Smith-Purcell radiation.

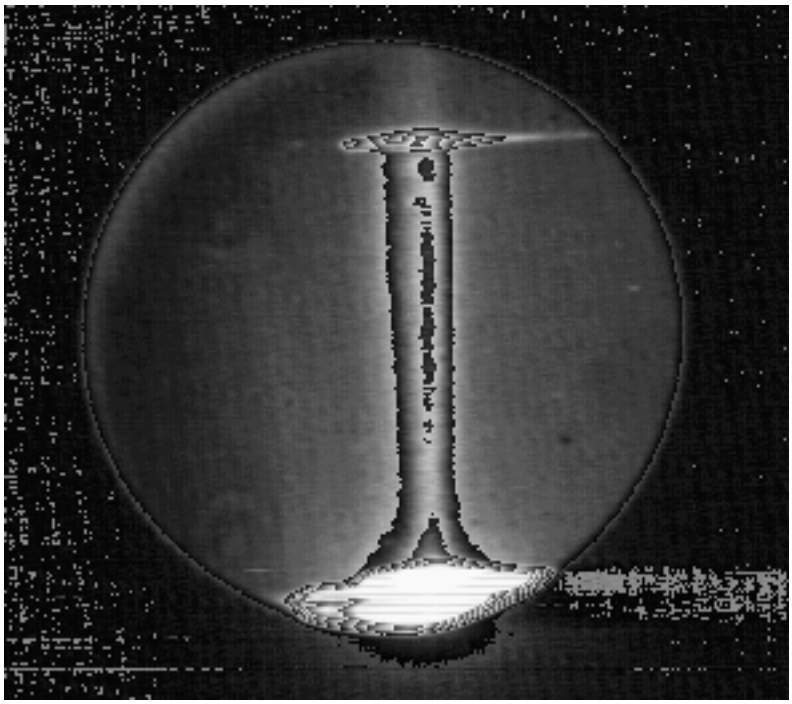

**FIGURE 5.18 : Radiation of 100 MeV electrons interacting with the glass blazed grating.**

The small halo and the large saturated halo visible on top and bottom of the picture are probably due to transition radiation and Cherenkov radiation produced by electrons penetrating the grating. The Al coating on the grating surface absorbs most of the radiation produced in the glass, but the light can also be reflected by the target holders and emerges through the small gap existing between the grating and the shielding and from the back side of the grating. As the camera observes at direction ($\eta$=0°, $\zeta$=0°) and as the electrons move perpendicularly to the grating rulings, the following properties for pure Smith-Purcell radiation are expected:

1) the radiation wavelength should be 555.5 nm (equation ( 1.39 ) with $c_0/v_0$=1, $\Psi_1$=0°, $\eta$=0° and D=555.5 nm)

2) the radiation should be H-polarized (equation ( 1.17 ) to ( 1.20 ) with $\Psi_1$=0° and $\zeta$=0°).

## 5.2.1 Measurement of the polarization

Figure 5.19 shows the polarization of the radiation measured for 35 MeV, 55 MeV and 97 MeV electrons. The experimental points indicate the maximum intensity observed at the grating surface as a function of the angular position $\varphi$ of the polarizer. The data were scaled to the same value at $\varphi$=90°. The line shows the intensity expected for a purely H-polarized radiation. The experimental data follow the theoretical curve remarkably well, except near 0° and 180°. The low intensity observed for this state of polarization (i.e. E-polarization) is probably due to transition radiation or Cherenkov radiation escaping through the Al layer on the surface of the grating.

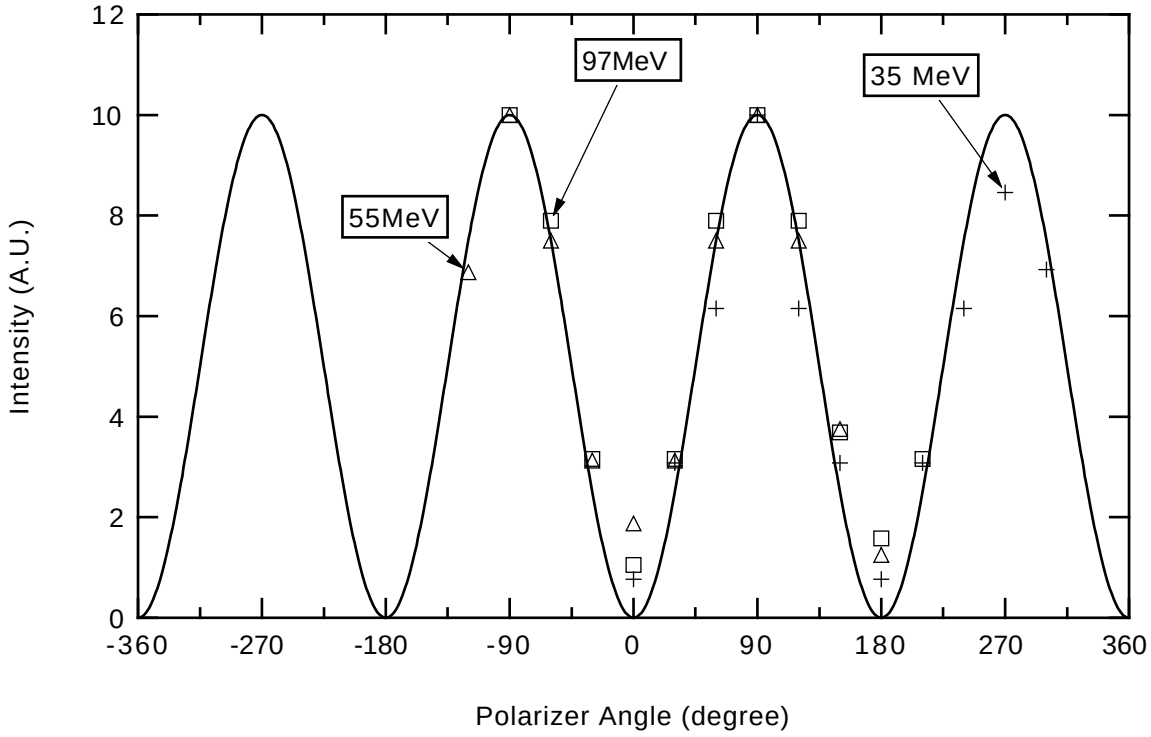


**FIGURE 5.19 : Polarization of light emitted by a 1800 l/mm grating interacting with electron beams of different energies. (+) 35 MeV, (∆) 55 MeV and (P) 97 MeV.**

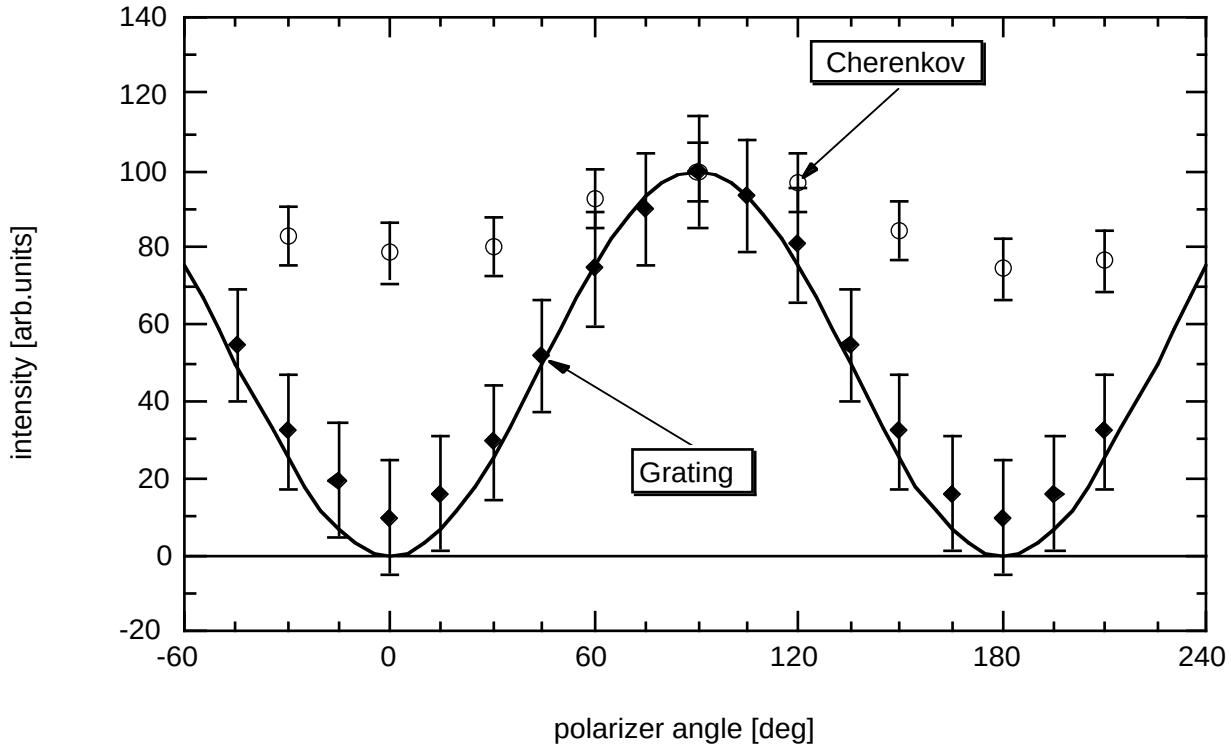


**FIGURE 5.20 : Polarization of light emitted by a glass grating and a glass plate interacting with a 110 MeV electron beam.**

Fig. 5.20 shows a comparison of the polarization of the radiation emitted by the grating and the glass plate using a 110 MeV electron beam. The curves have been scaled to the same value at φ=90°. The black line indicates the intensity expected for a purely H-polarized radiation. The radiation emitted from the grating is almost purely H-polarized while the degree of polarization for the light emitted by the glass plate is only 20%.

### 5.2.2 Measurement of the spectrum

The spectrum of the radiation was measured using the set of interference filters. Figure 5.21 shows the spectra obtained using a 110 MeV electron beam interacting with the blazed grating and with the glass plate. The data have been corrected for the transmission of the filters and the spectral sensitivity of the cathode camera. While the radiation emitted by the glass plate covers a broad spectrum from 400 to 700 nm, the radiation observed from the grating exhibits a narrow spectrum: almost all the intensity is concentrated near 550 nm. The curve for the glass light is simply a guide for the eyes. For the grating data, the curve is a Gaussian centered at 555.5 nm and fitted to the data.

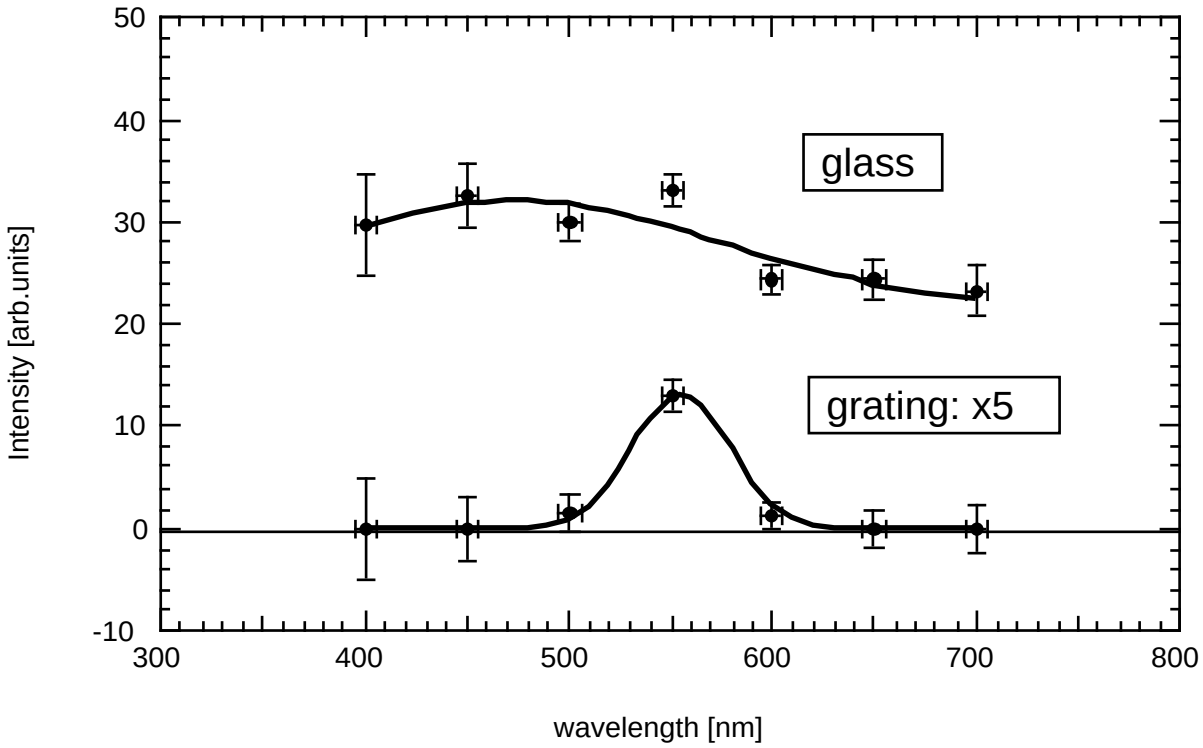


**FIGURE 5.21 : Spectra of light emitted by a glass plate and a glass grating interacting with a 110 MeV electron beam. Electron beam angle of incidence: 6.5°.**

### 5.2.3 Energy dependence of the radiation factor

The energy dependence of the radiation factor was determined using Eq.( 1.88 ). The beam energy was measured using the magnetic energy analyser and the beam current was registered with the fast ferrite (cf. chapter 4). The shape of the beam was measured using the OTR radiators and Gaussians were fitted to the beam profile. Figure 5.22 shows an example of such a fit. The OTR picture of a 30 MeV electron beam has been taken and a cut along the y-axis (corresponding to the direction of the rulings of the grating) is plotted. The beam shape can be well represented by a Gaussian profile.

Fig. 5.23 shows the relative values of the radiation factor $|R_{-1}(0,0)|^2$ compared to calculations carried out using techniques described in chapter 3. The theoretical values were scaled to the experimental data at 55 MeV. No attempt was made for a comparison on an absolute scale, because the camera was not calibrated. In order to take into account the finite angle of incidence $\Phi$ of the electron beam, Eq. ( 1.88 ) has been integrated numerically over the grating length considering an electron trajectory which is stepwise parallel to the grating surface along one period D. The divergence of the electron beam was not included in the calculations.

The general trend in the energy dependence of the radiation factor agrees well with the predictions for Smith-Purcell radiation. The large uncertainties in the experimental data especially at low energies are mostly due to the bad signal-to-noise ratio because of the very low current used in the experiment in order to avoid as much as possible damage to the grating.

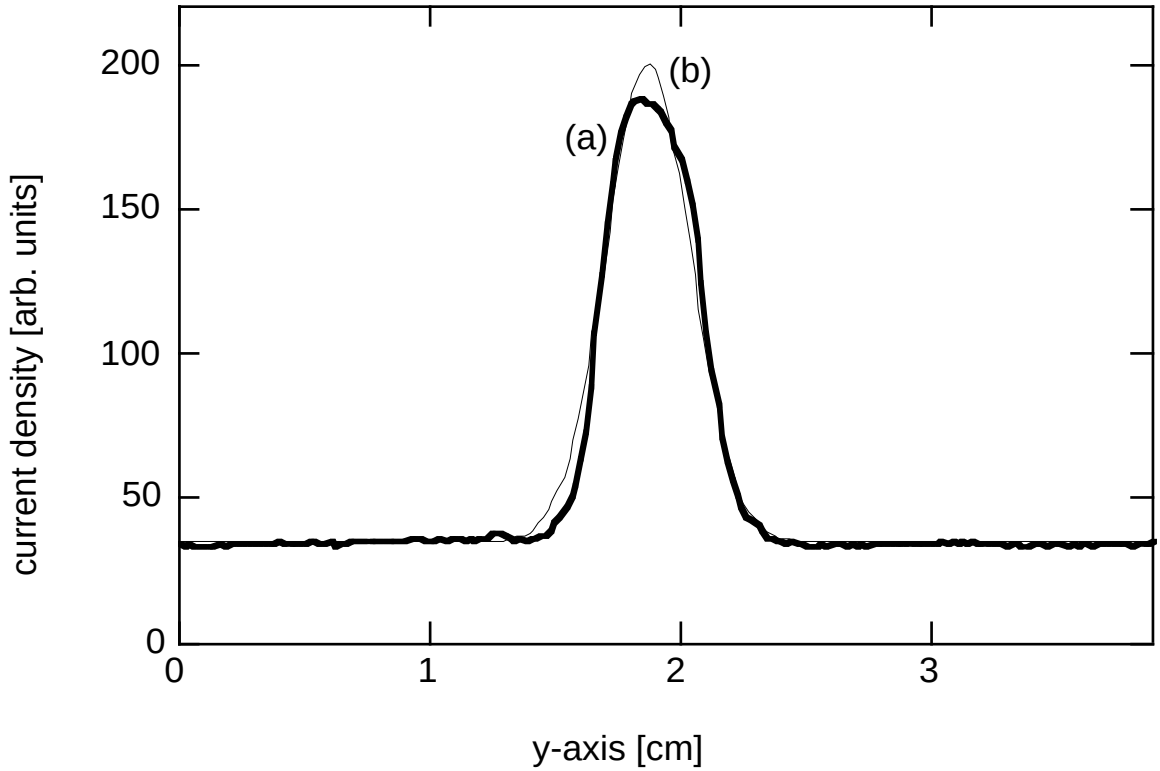


**FIGURE 5.22 : Fit of the electron beam profile at 30 MeV (a) experimental data, (b) Gaussian fit.**

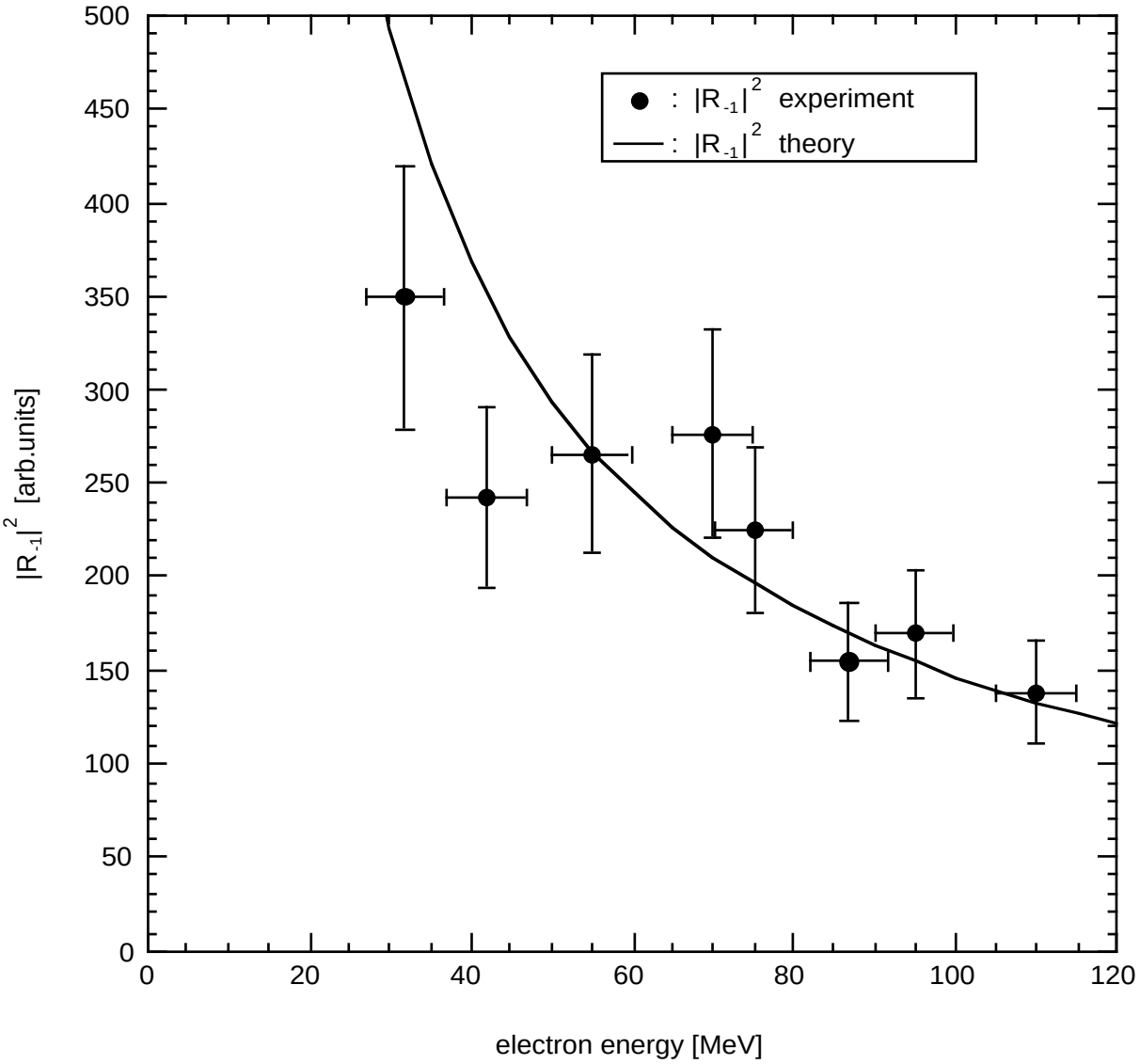


**FIGURE 5.23 : Energy dependence of the radiation factor for the blazed grating, as extracted from the experimental data, compared with the theoretical energy dependence.**

Unfortunately, no confirmation of these results could be obtained during a second run in January 1994 due to the destruction of the grating by the electron beam. Figure 5.24 shows a picture of the blazed grating obtained with a scanning electron microscope after the experiments. The surface of the grating has been damaged, probably by excessive heating. Characteristics of recrystallisation of the Al reflective layer can be seen and the grating rulings have been partially destroyed.

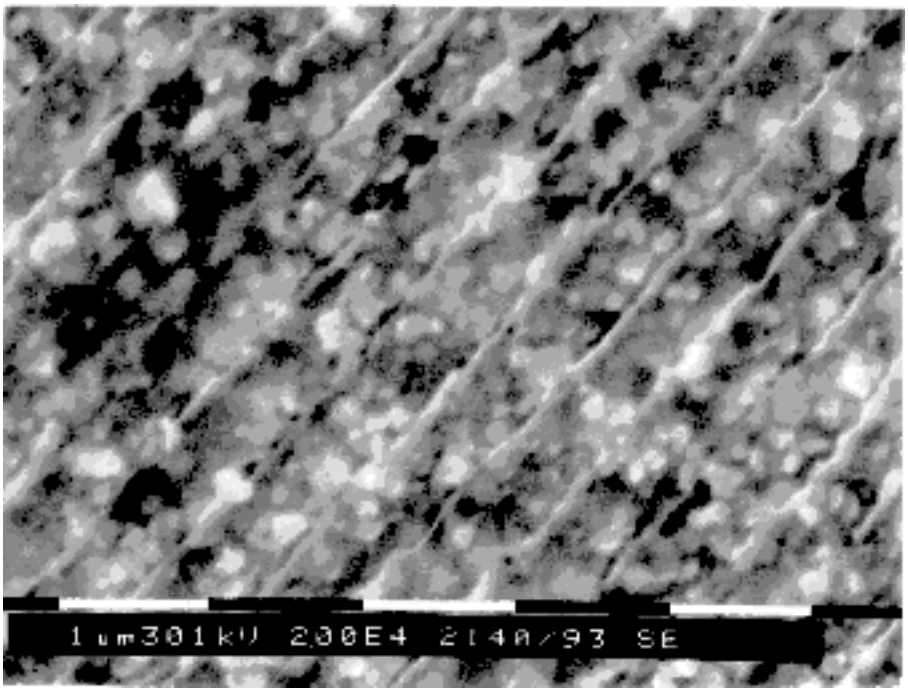


**FIGURE 5.24 : A picture of the blazed grating after exposure to the electron beam during Smith-Purcell experiments.**

## 5.3 Second experiment: horizontal insertion device and sinusoidal grating

A second experiment was carried out with an insertion device mounted horizontally and a 1800 l/mm glass grating with sinusoidal profile. The configuration of the experiment as described in paragraph 5.1.2 would allow a verification of the theory developed in chapters 1 and 2 for Smith-Purcell radiation produced by electrons moving at an arbitrary angle with respect to the grating rulings. This experiment has been carried out beginning October 1993, after the first experiment in September 1993. Unfortunately, the sinusoidal grating was destroyed before any observation could be done. The surface of the grating was destroyed at a macroscopic scale, probably due to the melting of the epoxy layer deposited for the replication of a master grating (cf. section 5.1.3). Bubbles of gas have perforated the Al layer. Fig. 5.25 shows a picture of the grating surface after the experiment, obtained with a scanning electron microscope at very low magnification. The grating rulings were destroyed, probably by recrystallisation of the Al reflective layer. Fig. 5.26 shows a picture of the grating surface obtained with a scanning electron microscope at high magnification.

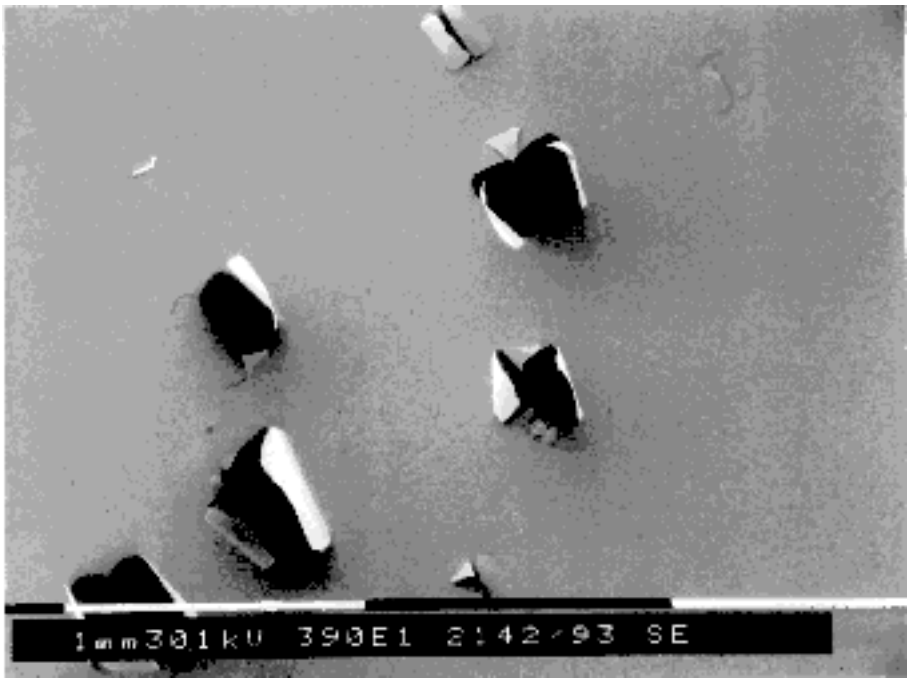


**FIGURE 5.25 : A picture at low magnification of the sinusoidal grating after destruction by the electron beam during Smith-Purcell experiments.**

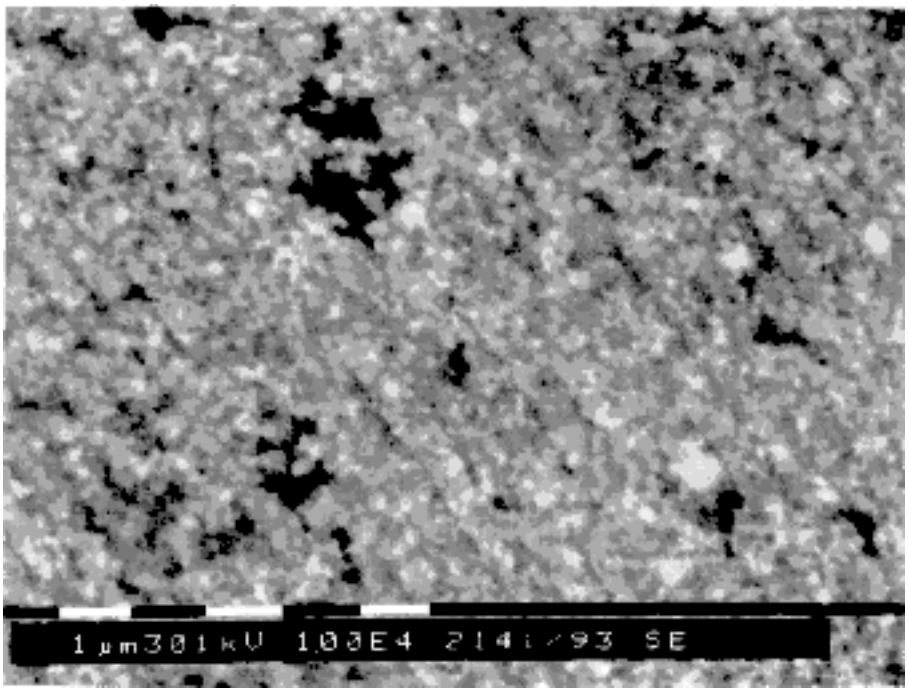


**FIGURE 5.26 : A picture at high magnification of the sinusoidal grating after destruction by the electron beam during Smith-Purcell experiments.**

## 5.4 Third experiment: vertical insertion device and SiC grating

This experiment was carried out during May 1994. Two SiC gratings with different profiles (see paragraph 5.1.3) were used. The radiation was measured as a function of the angle of incidence $\Phi$ of the electron beam, with the observation angle $\eta_n=\Phi$ changing when the grating was rotated (see figure 5.3(a)). A theoretical model [80] shows that in this case, the dispersion relation ( 1.40 ) is replaced by:

$$-\frac{n\lambda}{D} = \frac{c_0}{v_0}\cos\Phi - \sin\eta + \frac{s}{k}\sin\Phi \qquad (5.1)$$

in which for relativistic electrons one has $c_0/v_0\sim1$ and $|s/k|\sim1/\gamma<<1$. Therefore for an observation angle $\eta_n=\Phi$, one obtains:

$$-\frac{n\lambda}{D} = \cos\Phi - \sin\Phi = \sqrt{2}\sin\left(\frac{\pi}{4} - \Phi\right) \qquad (5.2)$$

Contrary to Smith-Purcell radiation, also positive orders can be observed. For $\Phi\leq45°$ only negative orders are observed, while for $\Phi\geq45°$ only positive orders appear.

Figure 5.27 shows the intensity distribution as a function of the incidence angle $\Phi$, obtained using 85 MeV electrons. No difference was observed between the two SiC gratings. The open circles show the intensity observed without filters. Curve (a) is a guide to the eye. Curve (b) is the intensity observed using the SiC mirror. The closed circles show from left to right the intensity observed with interference filters of 550, 500 and 450 nm respectively. The data have been corrected for the known transmission of the filters, but not for the wavelength dependent sensitivity of the detection system (optical bench and camera sensitivity). Curve (c) is the sum of three Gaussians centered at angles $\Phi(\lambda)$ calculated using Eq. ( 5.2 ) for the central wavelengths of the bandpass filters. The full width half maximum is given by a bandwidth $\Delta\lambda$ calculated for the angular aperture of the detection system usingEq. ( 5.2 ).

The experimental data at 550, 500 and 450 nm agree fairly well with the theoretical prediction, but the weakness of the signal lead to large error bars. According to Eq. ( 5.2 ) in first order n=-1 and at angles $\Phi>15°$ only wavelengths $\lambda<400$ nm contribute, for which the sensitivity of the detection system decreases drastically. The photocathode of the camera is not sensitive in the near UV and the glass windows of the radiation chamber and the lenses of the optical bench are not transparent in this spectral range. At $\Phi=45°$, the zero order n=0 is observed and all wavelengths contribute. The radiation is very intense, comparable to transition radiation observed from the SiC mirror. The spectra of the radiation emitted by the SiC gratings and by the SiC mirror were identical. The angular distributions of the radiation were very similar.

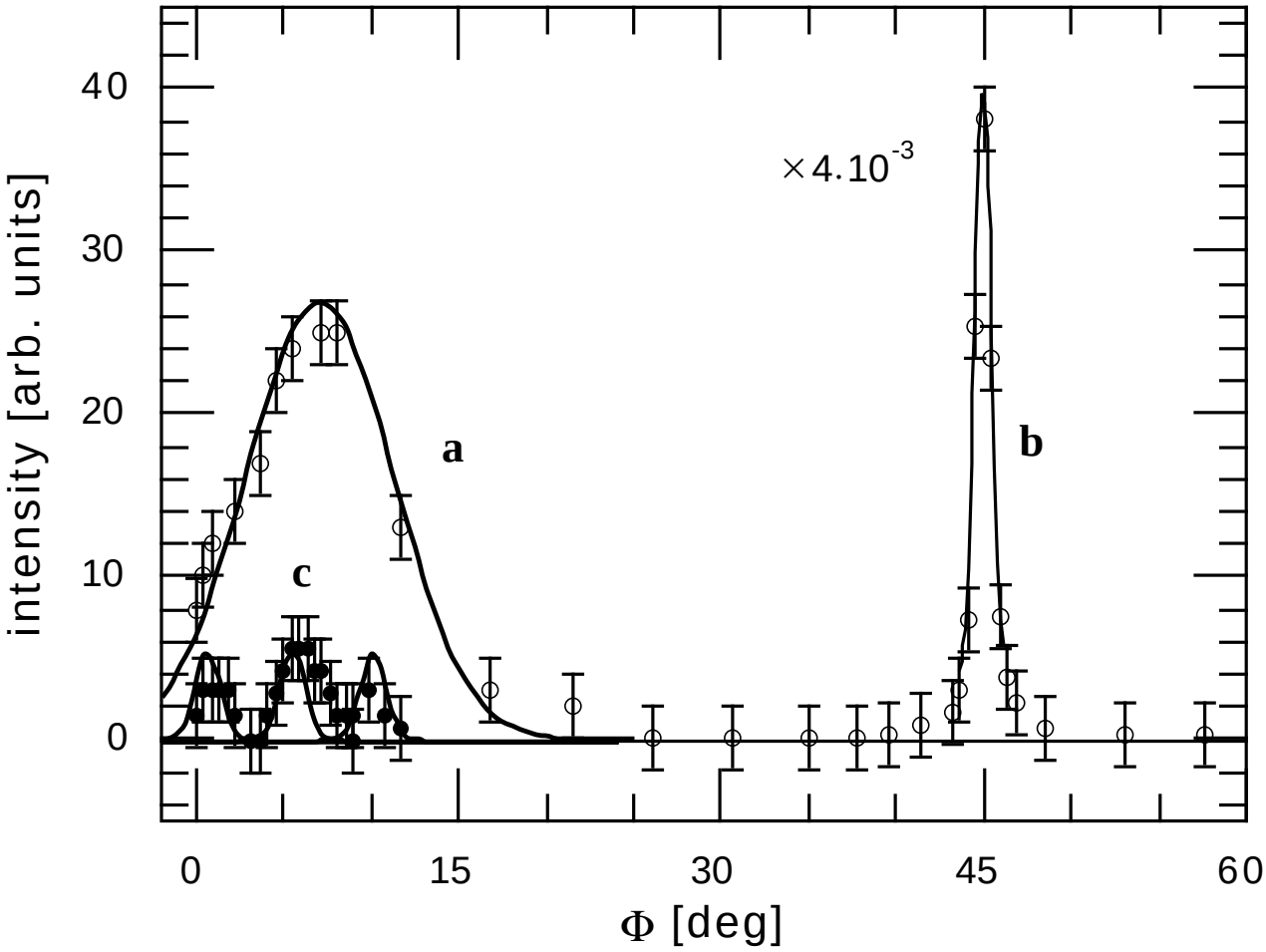


**FIGURE 5.27 : Intensity distribution of light emitted from SiC grating as a function of the incidence angle Φ with 85 MeV electrons. Open circles: without filters. Closed circles: from left to right with filters of 550, 500, 450 nm respectively. (a) guide to the eye, (b) intensity with a SiC mirror, (c) theoretical predictions from Eq. ( 5.2 ).**

The polarization of the radiation was measured for several angles of incidence. In that measurement also no difference has been observed between the two SiC gratings. For low angles of incidence $\Phi<15°$, the radiation was purely H-polarized, as expected for Smith-Purcell radiation at $\Phi=0°$. No wavelength dependence was observed using the interference filters. For the 0-order at $\Phi=45°$, the polarization was identical with that expected for OTR. No dependence on the wavelength was noticed using the interference filters. Fig. 5.28 shows the intensity of the radiation at $\Phi=2°$ and $\Phi=45°$ as a function of the polarizer angle $\varphi$. The solid line shows the intensity expected for a purely H-polarized radiation like pure Smith-Purcell radiation emitted for $\Phi=0°$. It has been scaled to the experimental data (closed circles) at $\varphi=270°$. The dashed line shows the constant intensity expected from transition radiation emitted by a perfectly conducting surface for a non divergent beam [11]. It has been scaled to the experimental data (open circles) at $\varphi=90°$. The experimental data agree well with the theoretical predictions.

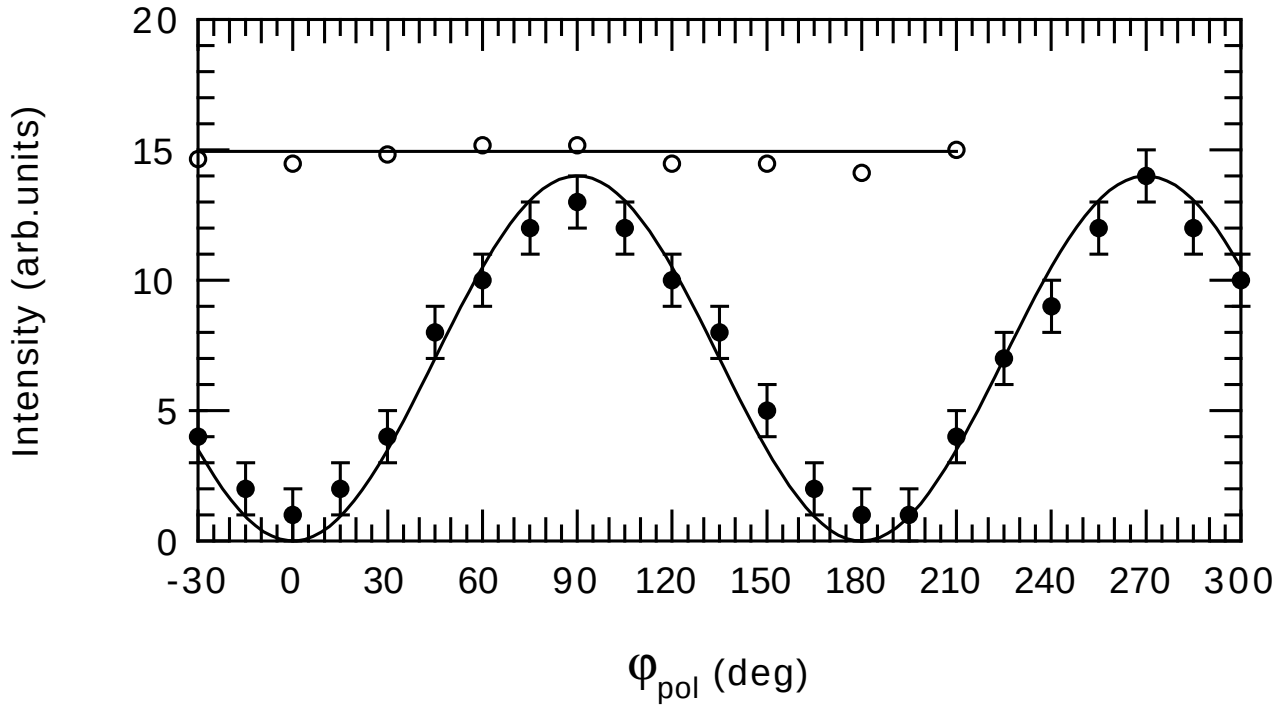


**FIGURE 5.28 : Polarization of light emitted from SiC grating with 85 MeV electrons. Closed circles: at Φ=2°. Solid line: theoretical curve for a purely H-polarized radiation. Open circles: at Φ=45°. Solid line: theoretical curve for OTR from a perfectly conducting surface and a non divergent beam at Φ=45°.**

The experiment was carried out for several electron energies between 20 to 110 MeV. The energy dependence of the radiation was measured at low angles of incidence $\Phi<6°$ and at $\Phi=45°$. For $\Phi=45°$, the energy dependence expected for OTR from a flat surface was obtained. For $\Phi<6°$, the energy dependence of the radiation was calculated from the observed intensity assuming a Gaussian beam profile as in section 5.2.

Fig. 5.29 shows the results for low angles of incidence. The circles are the values of the radiation factor derived from the intensity measured at $\Phi<6°$ which all have shown the same energy dependence. The curves are the same for the two SiC gratings. The solid line is the energy dependence of the radiation factor calculated for pure Smith-Purcell radiation from a lamellar grating with period D=555.5 nm, and with parameters h/D=0.1 and a/D=0.5. Up to 70 MeV, the accordance of the experimental results and the theoretical curve is good. At higher energies, large discrepancies appear. They could be explained by the fact that the grating profile was actually not a rectangular profile (cf. Fig. 5.12). Also the profile could had been modified due to heating of the surface (like for the glass grating), even if no damage was visible after the experiment. Therefore calculations have also been carried out for a sinusoidal grating with h/d=0.1 and for the grating profiles described by Fig. 5.12, approximating the profile by its Fourier transform. These calculations have shown a very similar energy dependence than for the lamellar grating. We conclude then that the discrepancies are probably explained by the difference between the theoretical model, which assumes parallel electrons and the experimental configuration in which the electrons were coming at small but finite incidence angles.

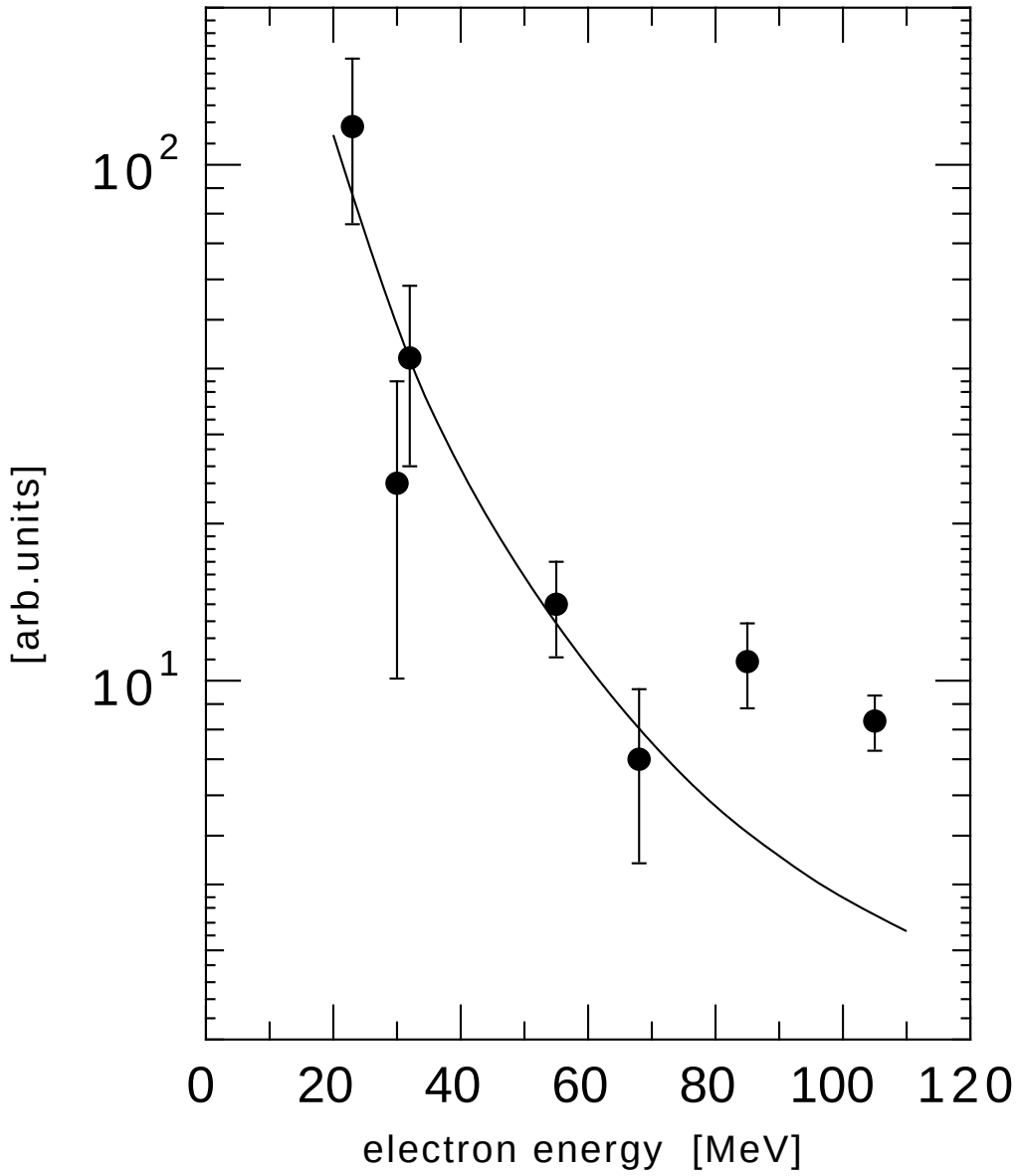


**FIGURE 5.29 : The energy dependence of the radiation produced by relativistic electrons interacting with a SiC grating at low angles of incidence. Circles: values of the radiation factor at $\Phi<6°$. Curve: energy dependence of the radiation factor calculated for pure Smith-Purcell radiation with a lamellar grating.**

Fig. 5.30 shows the results for a large angle of incidence. The circles are the intensities per unit current density observed at specular reflection for $\Phi=45°$. No difference has been noticed between the two SiC gratings. The line is the theoretical energy dependence of optical transition radiation calculated taking into account the aperture of the optical bench. At specular reflection the correspondence between the experimental points for the radiation emitted from a grating and the theoretical curve calculated for transition radiation from a flat surface is excellent.

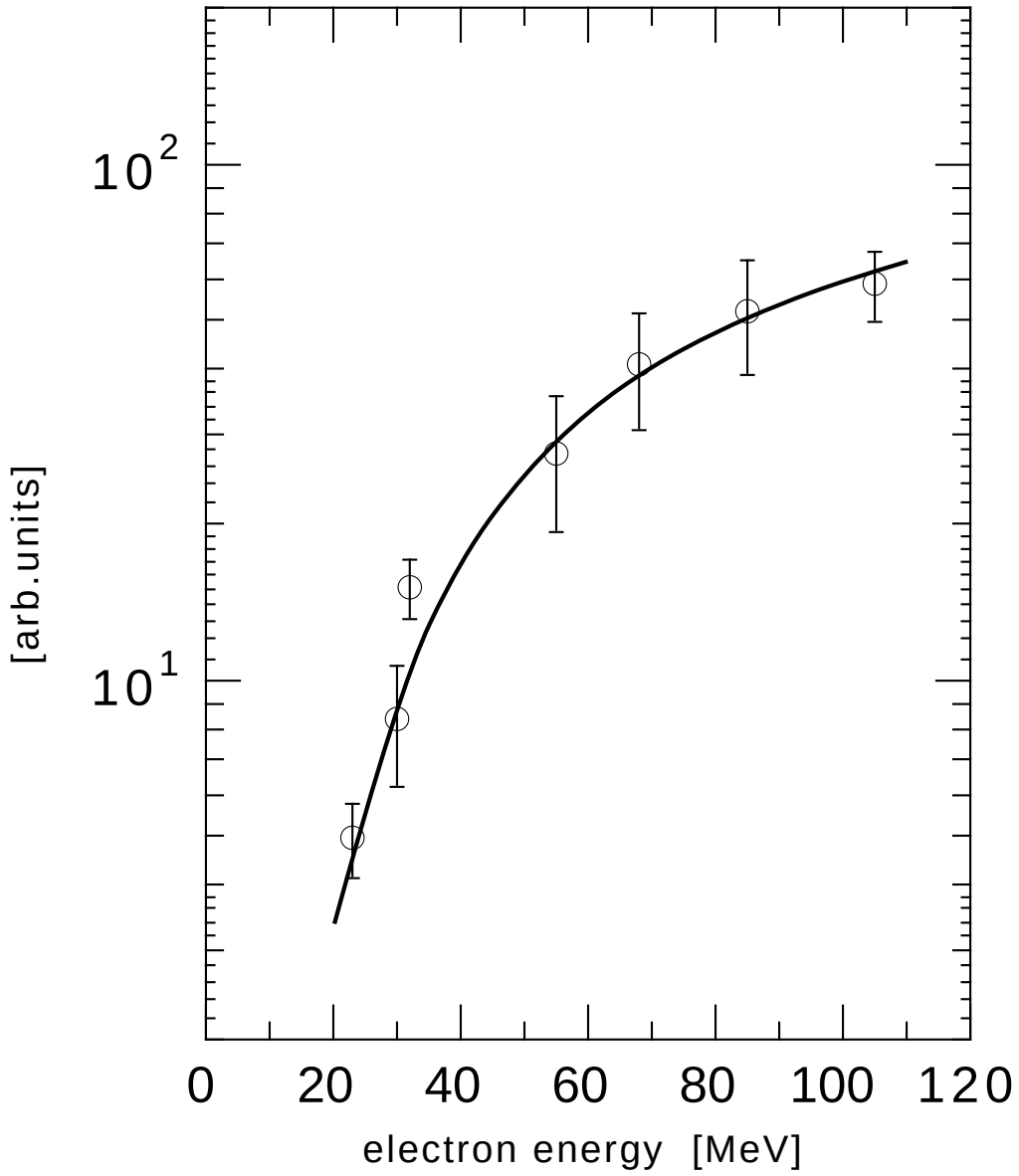


**FIGURE 5.30 : The energy dependence of the radiation produced by relativistic electrons interacting with a SiC grating at an incidence angle of 45°. Circles: measured energy dependence. Curve: theoretical energy dependence of OTR calculated for the geometry of the experiment.**

At specular reflection and for Φ=45° no difference in the polarization and energy dependence has been observed between the transition radiation emitted by electrons hitting a flat surface and the radiation emitted by electrons hitting a grating. This result is surprising because the characteristics of both surfaces are different and lead in optics to different properties. As the grating diffracts light, the reflection coefficient for the 0-order, which corresponds to specular reflection is generally lower than for a flat surface. Also gratings have generally very special polarization properties, for example near Wood-Rayleigh anomalies. Such effects have not been observed yet in OTR experiments from gratings.

# CONCLUSIONS

This work is the result of a three years fellowship spent at the Institute for Reference Materials and Measurements (IRMM), one institute of the Joint Research Centre of the European Union, as a Ph.D. student from the Laboratoire des Systèmes Photoniques, Université Louis Pasteur-Strasbourg. The first part of this work had a theoretical dominance, while the second part was mostly experimental using the GELINA linear accelerator of the IRMM.

In the first chapter, a theoretical description in the frame of an electromagnetic theory of the Smith-Purcell radiation produced by electrons moving parallel to a grating at an arbitrary angle with respect to the grating rulings was proposed. Therefore, this work is an extension of the previous models assuming electrons moving perpendicular to the grating grooves. The field of the moving electron has been calculated. Techniques derived from the electromagnetic theory of gratings have been applied to calculate the Smith-Purcell radiation intensity as a function of the propagative waves diffracted by the grating and several properties of the Smith-Purcell radiation have been established. The calculation of the Smith-Purcell effect is reduced to the solution of a special grating problem involving an evanescent incident wave in a conical mounting. The domain of validity of the model has been discussed. It is restricted to perfectly conducting surfaces. A three-dimensional theory of the Smith-Purcell radiation produced by electrons moving at an arbitrary angle with respect to the rulings of a metallic or dielectric grating remains to be developed. The case of electrons not moving parallel to the grating surface has been discussed. It has been shown that using relativistic electrons and gratings of large period, the alignment of the electron beam parallel to the grating surface and the finite divergence of the electron beam are not mandatory. Therefore, it should be fairly easy to generate radiation in the far-infrared or millimeter range using the Smith-Purcell effect.

In chapter two, some techniques to solve the grating problem have been adapted to the case of Smith-Purcell diffraction and their domain of application has been investigated. For rectangular gratings, the Modal Expansion Method is the most appropriate. For shallow sinusoidal grating, the Rayleigh method is very powerful and gives exact results with moderate computational efforts. The Integral Method is the most general one and can be adapted to a large variety of grating profiles. For all methods, reliable results are obtained when convergence is achieved and the power relations are satisfied. The reciprocity theorem for non-symmetric grating profiles can also be used, but it is more difficult to satisfy.

In chapter three, the previously exposed theories have been applied to calculate the Smith-Purcell radiation produced by relativistic electrons with energy in the 1 to 100 MeV range interacting with millimeter period gratings, leading to radiation in the far-infrared and millimeter range, a spectral region where intense tunable sources are hardly available. The characteristics of the radiation have been described for several shallow gratings. The influence of the grating depth has been investigated for sinusoidal and rectangular gratings. The influence of tilting the electron beam trajectory with respect to the grating rulings on the radiation characteristics has been studied. The Smith-Purcell radiation produced by 1 to 10 MeV electrons interacting with shallow lamellar or blazed gratings constitutes a good candidate for building sources based on the spontaneous emission by choosing the adequate experimental parameters. Therefore, the Smith-Purcell effect could be the basis of a new type of free electron lasers using low energy accelerators (some MeV) and gratings, but a detailed theory of such devices remains to be written in this energy range.

For the first time, high energy electrons of 20 to 110 MeV have been used to produce radiation by interaction with optical gratings using the GELINA facility. The results have been exposed in chapter five, in which the spectral and angular distributions, the polarization and the dependence on the electron energy were detailed. At small angle of incidence, the radiation shows the main characteristics of Smith-Purcell radiation. The polarization and wavelength were in good agreement with the theory. The energy dependence of the radiation factor was compared to theoretical predictions. A fairly good agreement was obtained for the blazed glass grating except at low electron energies (below 40 MeV). When using a SiC grating discrepancies appear at high energies (over 80 MeV). These discrepancies probably point out the limits of the model used for theoretical predictions, which does not take into account the finite angle of incidence of the electrons. The radiation intensity was weak, leading to large errors in the measures. This was due to the small beam current used for the experiments, in order to avoid damage to the grating. Also very few electrons really interact with the grating, because of the low interaction range, about 10 μm, and the large size of the beam of several millimeters. Therefore, the experiment should be repeated for another wavelength range or with a small emittance accelerator which would deliver a very narrow electron beam. In view of the theoretical predictions, an accelerator of lower energy in the 1 to 10 MeV range should be used.

An experiment to measure the radiation produced when the electrons hit the grating surface with a finite incidence angle was carried out. An experimental comparison between transition radiation from a flat surface and “transition radiation from a grating” has been attempted. At the specular reflection and for an angle of incidence of 45°, the characteristics of the radiation produced by electrons hitting a grating are very similar to those of optical transition radiation produced when electrons hit a mirror. The energy dependence and the polarization were identical at 400, 450, ..., 700 nm. It would be interesting to carry out this experiment with an actual spectrometer to study more accurately the spectrum in order to look for effects like Wood-Rayleigh anomalies or wavelength-dependent polarization state of the diffracted waves, which are well known in spectroscopy, but were not observed in these experiments.

A detailed study at the GELINA facility is foreseen when the new radiation physics laboratory will be equipped and when the rejuvenation of the electron accelerator will be completed. The low emittance of the future accelerator combined with the detection facilities which will be provided in the new laboratory should permit to improve and to complete the results obtained up to now.

# ACKNOWLEDGMENTS

During the three years long period that I spent at the IRMM, I had the opportunity to meet many persons who contributed in some way or another to this work. I would like to thank all of them here, and I apologize in advance for those whom I forgot to mention.

I would like to thank Prof. P. Meyrueis, from the Laboratoire des Systèmes Photoniques in Strasbourg who accepted to be my supervisor for doing a PhD work at the IRMM in Geel. The difficulties in organizing the work were surpassed thanks to his help, and to the support of his co-workers, especially Prof. J. Harthong, with whom I had interesting discussions and who also accepted the heavy work of being my “rapporteur interne”, and Y. Takakura, who provided me with numerous useful advises.

At the IRMM, I would like to thank firstly Jean-Marie Salomé. His long experience running the Linac made possible the experiments. I cannot forget the constant support he provided me, thanks to his good knowledge of both the French and EC administrations. I also acknowledge the Direction of the institute, Prof. W. Müller and Prof. A. Deruytter for accepting and supporting this work at IRMM.

These lines are dedicated to Peter Rullhusen and Norbert Maene. The constant support, advice and assistance that they gave me, helped not only to start this PhD work, but certainly to complete it. They also greatly helped to make my so-called English intelligible. I would like to thank the colleagues who helped me in some way to progress in the field of radiation physics. Gert De Roost, Nico Ooms, Kris Verstraelen, Stéphanie Schaeffer, Peter Goedtkindt, the Operators of the Linac, the Workshop team and the Computer team. I also would like to thank all the colleagues at IRMM for the good working atmosphere that I found when I arrived. I cannot give all the names here and I apologize for it, but I especially thank Frank Gunsing and Thierry Moreno, who helped me to relax in some difficult periods.

The idea of studying Smith-Purcell radiation was from Louis Wartski, who I thank for the interest he has shown for this work, and the encouragement he provided to me.

# REFERENCES


[1] I.M. Frank, Izv. Akad. Nauk. SSSR Ser. Fiz. **6**, 3 (1942) *(in Russian)*

[2] S.J. Smith and E.M. Purcell, Phys. Rev. **92**, 1069 (1953)

[3] W.W. Salisbury, U.S. Patent 2 634 732 filed October 26, 1949 issued April 7, 1953

[4] W.W. Salisbury, J. Opt. Soc. Am. **52**, 1315 (1962)

[5] K.Ishiguro and T.Tako, Optica Acta G.B. **8**, 25 (1961)

[6] J.A. Bradshaw, Proc. Symp. Mil. Waves 8, Brooklyn, N.Y. Polytechnic Press p 223, 1959

[7] W.W. Salisbury, J. Opt. Soc. Am. **60**, 1279 (1970)

[8] G. Toraldo Di Francia, Nuovo Cimento **16**, 61 (1960)

[9] I. Tamm, Zh. Fis. SSSR **1**, 439 (1939)

[10] I.E. Frank and V.L. Ginzburg, J. Phys. (Paris) **9**, 353 (1945)

[11] L. Wartski, Ph.D. thesis Université Paris Sud (1976) *(in French)*

[12] P. Goedtkindt, Ph.D. thesis Vrije Universiteit Brussel (1993) *(in English)*

[13] B.M. Bolotovskii and G.V. Voskresenskii, Sov. Phys. Usp. **9**, 73 (1966)

[14] V. G. Baryshevsky and I. D. Feranchuk, J. Phys. (Paris) **44**, 913 (1983)

[15] A. Hessel, Can. J. Phys. **42**, 1195 (1964)

[16] R.W. Wood, Philos. Mag. **4**, 396 (1902)

[17] O.A. Tret'yakov, Radio Eng. Electron. Phys. **10**, 1156 (1965)

[18] Ye.V. Avdeyev and G.V. Voskresenskii, Radio Eng. Electron. Phys. (USSR) **9**, 1360 (1966)

[19] S.J. Glass and H. Mendlowitz, Phys. Rev. **174**, 57 (1968)

[20] J.P. Bachheimer, Ph.D. thesis Université Scientifique et Médicale Grenoble (1971) *(in French)*

[21] R.F. Millar, Proc. Cambridge Phil. Soc. **69**, 175 (1971)

[22] C.W. Barnes and K.G. Dedrick, J. Appl. Phys. **37**, 411 (1966)

[23] E. Lalor, Phys. Rev. A **7**, 735 (1973)

[24] A.R. Neureuther and R. Mittra, Proc. IEEE **55**, 2134 (1967)

[25] A.R. Neureuther and R. Mittra, Can. J. Phys. **47**, 435 (1969)

[26] E.L. Burdette and G. Hughes, Phys. Rev. A **14**, 1766 (1976)

[27] M.J. Moran, Phys. Rev. Let. **69**, 2523 (1992)

[28] P.M. Van den Berg, J. Opt. Soc. Am. **63**, 689 (1973)

[29] P.M. Van den Berg, J. Opt. Soc. Am. **63**, 1588 (1973)

[30] P.M. Van den Berg, J. Opt. Soc. Am. **64**, 325 (1974)

[31] L.N. Deryugin, Radio. Eng. Electron. Phys. (USSR) **15**, 25 (1960)

[32] O. Haeberlé *et al*., Phys. Rev. E **49**, 3340 (1994)

[33] A. Wirgin, Opt. Comm. **26**, 148 (1978)

[34] M. Okita *et al.*, Electron. Comm. Japan 2 **76**,42 (1993)

[35] J.P. Bachheimer, J. Physique **31**, 665 (1970)

[36] J.P. Bachheimer, Phys. Rev B **6**, 2985 (1972)

[37] J.C. McDaniel *et al.*, Appl. Opt. **28**, 4924 (1989)

[38] A. Gover *et al.*, J. Opt. Soc. Am. B **1**, 723 (1984)

[39] *Electromagnetic Theory of Gratings*, edited by R. Petit (Springer-Verlag, Berlin, 1980)

[40] Lord Rayleigh, Proc. R. Soc. London Ser. A **79**, 399 (1907)

[41] R.Petit, Opt. Acta **14**, 301 (1967)

[42] M.L. Ter-Mikaelian, *High-Energy Electromagnetic Processes in Condensed Media* (Wiley Interscience, New York, 1972)

[43] L.N. Deryugin, Radio. Eng. Electron. Phys. (USSR) **15**, 12 (1960)

[44] R.F. Millar, Proc. Cambridge Phil. Soc. **69**, 217 (1971)

[45] W.C. Meecham, J. Appl. Phys. 27, 361 (1956)

[46] H. Ikuno and K. Yasuura, IEEE Trans.Antennas Propag. **AP-2**, 657 (1973)

[47] R. Petit and M. Cadilhac, C.R. Acad. Sci. **259**, 2077 (1964) *(in French)*

[48] A. Wirgin, Rev. Opt. **45**, 249 (1964) *(in French)*

[49] J.L. Uretski, Ann. Phys. (Paris) **33**, 400 (1965) *(in French)*

[50] J. Pavageau *et al.*, C.R. Acad. Sci. **264**, 424 (1967) *(in French)*

[51] P.M. Van den Berg, Appl. Sci. Res. **24**, 261 (1971)

[52] J. Pavageau and J. Bousquet, Opt. Acta **17**, 469 (1970)

[53] D. Maystre and R. Petit, Opt. Comm. **5**, 90 (1972) *(in French)*

[54] O.A. Tret'yakov et al., Sov. Phys. Tech. Phys. **11**, 22 (1966)

[55] MATLAB User's Guide and Reference Guide, The MathWorks, Inc

[56] J.J. Dongarra *et al.*, LINPACK User's Guide Society for Industrial and Applied Mathematics, Philadelphia (1979)

[57] B.T. Smith *at al.*, EISPACK Guide, Lecture Notes In Computer Science 6 (Springer-Verlag, 1976)

[58] P.M. Van den Berg J. Opt. Soc. Am. **71**, 1224 (1981)

[59] K. Yasuura and Y. Okuno, J. Opt. Soc. Am. **72**, 847 (1982)
[60] Y. Okuno and T. Matsuda, J. Opt. Soc. Am. **73**, 1305 (1983)
[61] Y. Okuno and T. Matsuda, J. Opt. Soc. Am. A **2**, 572 (1985)
[62] S. Jovicevic and S. Sesnic, J. Opt. Soc. Am. **62**, 685 (1972)
[63] J. Walsh *et al.*, Nucl. Instr. Meth. **A341**, 277 (1994)
[64] K. Yasumoto *et al.*, IEEE Trans. Plasma Sci. **18**, 699 (1990)
[65] G. Doucas *et al.*, Phys. Rev. Lett. **69**, 1761 (1992)
[66] G. Doucas *et al.*, Nucl. Instr. Meth. **A331**, 609 (1993)
[67] K.J. Woods, *Private Communication*
[68] A. Bensussan and J.M. Salomé, Nucl. Instr. Meth. **155**, 11 (1978)
[69] D. Tronc *et al.*, Nucl. Instr. Meth. Phys. Res. **228**, 217 (1985)
[70] J.M. Salomé and R. Forni, IEEE Trans. Nucl. Sci. **NS-28**, 2234 (1981)
[71] R.B. Fiorito and D.W. Rule, AIP Conf. Proc., Oct. 20-23, Santa Fe, NM (1993)
[72] S.Schaeffer, Internal report, GE/LI/1, Nov. 1992 IRMM, Retieseweg, B-2440 Geel
[73] P. Rullhusen, O. Haeberlé *et al. (in preparation)*
[74] G. de Roost, dissertation Hoger Instituut der Kempen (HIK) (1993), B-2440 Geel *(in Dutch)*
[75] N. Ooms, dissertation Hoger Instituut der Kempen (HIK) (1994) B-2440 Geel *(in Dutch)*
[76] Jobin Yvon, Diffraction Gratings Handbook
[77] Zeiss, Zeiss Information No. 92 (1982)
[78] Thomson-CSF, Notice TEV 3150 (1973) *(in French)*
[79] Melles Griot, Optics Guide 5
[80] O. Haeberlé *et al.*, Phys. Rev. Lett. *(submitted)*

## ABSTRACT

The Smith-Purcell effect has been widely studied since its theoretical prediction in 1942 and its first experimental confirmation in 1953. The previous available models assume electrons moving parallel to a grating surface and perpendicular to the grating rulings. In the first chapter, the description of the Smith-Purcell effect for electrons moving parallel to a grating, at an arbitrary angle with respect to the grating rulings is exposed in the frame of an electromagnetic theory.

The model is restricted to perfectly conducting surfaces, for which some of the modern available techniques to solve the grating problem are adapted to the peculiar configuration of the incident field. These techniques are developed in the second chapter.

In chapter three, the Smith-Purcell radiation produced by relativistic electrons with energy in the 1 to 100 MeV range interacting with millimeter period gratings is calculated, using the previously developed theories. The properties of the radiation are described and possible applications are proposed.

In the fourth chapter, the GELINA facility which was used to carry out Smith-Purcell experiments is described.

In chapter five, the Smith-Purcell experiments are described. The spectral and angular distributions, the polarization and the dependence on the electron energy of the radiation obtained by interaction of high energy electrons of 20 to 110 MeV with optical gratings in various configurations are presented.



### KEYWORDS

Electromagnetism, Diffraction, Grating, Electron accelerator, Infrared, Millimeter waves, Smith-Purcell effect, Transition Radiation